

379
N81d
No. 4471

MICROSTRUCTURAL STUDIES OF DENTAL AMALGAMS
USING ANALYTICAL TRANSMISSION
ELECTRON MICROSCOPY

DISSERTATION

Presented to the Graduate Council of The
University of North Texas in Partial
Fulfillment of the Requirements

For the Degree of

DOCTOR OF PHILOSOPHY

By

Tejpal Kaur Hooghan, B.S., M.S

Denton, Texas

May 1997

Major Prof: DR. Russell F. PINIZZOTTO

379
N81d
No. 4471

MICROSTRUCTURAL STUDIES OF DENTAL AMALGAMS
USING ANALYTICAL TRANSMISSION
ELECTRON MICROSCOPY

DISSERTATION

Presented to the Graduate Council of The
University of North Texas in Partial
Fulfillment of the Requirements

For the Degree of

DOCTOR OF PHILOSOPHY

By

Tejpal Kaur Hooghan, B.S., M.S

Denton, Texas

May 1997

Major Prof: DR. Russell F. PINIZZOTTO

Hooghan, Tejpal Kaur, Microstructural Studies of Dental Amalgams Using Analytical Transmission Electron Microscopy, Doctor of Philosophy (Physics), May, 1997, 166 pp., 4 tables, 55 illustrations.

Dental amalgams have been used for centuries as major restorative materials for decaying teeth. Amalgams are prepared by mixing alloy particles which contain Ag, Sn, and Cu as the major constituent elements with liquid Hg.

The study of microstructure is essential in understanding the setting reactions and improving the properties of amalgams. Until the work reported in this dissertation, optical microscopy (OM), scanning electron microscopy (SEM), and x-ray diffractometry (XRD) were used commonly to analyze amalgam microstructures. No previous systematic transmission electron microscopy (TEM) study has been performed due to sample preparation difficulties and composite structure of dental amalgams.

The goal of this research was to carry out detailed microstructural and compositional studies of dental amalgams. This was accomplished using the enhanced spatial resolution of the TEM and its associated microanalytical techniques, namely, scanning transmission electron microscopy (STEM), x-ray energy dispersive spectroscopy (XEDS) and micro-microdiffraction ($\mu\mu\text{D}$). A new method was developed for thinning amalgam samples to electron transparency using the "wedge technique."

Velvalloy, a low-Cu amalgam, and Tytin, a high-Cu amalgam, were the two amalgams characterized. Velvalloy is composed of a Ag_2Hg_3 (γ_1)/ $\text{HgSn}_{7.9}$ (γ_2) matrix

surrounding unreacted Ag_3Sn (γ) particles. In addition, hitherto uncharacterized reaction layers between $\text{Ag}_3\text{Sn}(\gamma)/\text{Ag}_2\text{Hg}_3$ (γ_1) and Ag_2Hg_3 (γ_1)/ $\text{HgSn}_{7.9}$ (γ_2) were observed and analyzed. An Ag-Hg-Sn (β_1) phase was clearly identified for the first time.

In Tytin, the matrix consists of Ag_2Hg_3 (γ_1) grains. Fine precipitates of Cu_6Sn_5 (η') are embedded inside the γ_1 and at the grain boundaries. These precipitates are responsible for the improved creep resistance of Tytin compared to Velvalloy. The additional Cu has completely eliminated the γ_2 phase which is the weakest component of amalgams. Ag-Hg-Sn (β_1) and large grains of Cu_6Sn_5 (η') are found adjacent to the unreacted alloy particles. Tytin alloy particles contain Cu_3Sn (ϵ) precipitates in a matrix of Ag_3Sn (γ) and Ag_4Sn (β).

SEM was used to correlate the TEM findings in the context of the general microstructure. The results are in good agreement with those published in the literature. The microstructural details reported here, many of which were not previously available, will help provide insight into the deformation mechanisms of dental amalgams.

ACKNOWLEDGMENTS

It is a great pleasure to thank the many people who helped me with advice, assistance, and encouragement during the course of my graduate studies.

First, I would like to thank Dr. Russell F. Pinizzotto, my dissertation supervisor, for his invaluable advice, help and patience during the course of this project, and my studies. I would also like to thank the faculty members of the Physics Department for their time and help in ways more than one. In particular, I would like to thank Dr. William D. Deering for his constant support and encouragement during my studies in the Department.

I would like to deliver special thanks to Dr. T. Okabe for his help in obtaining samples for this project for its initial financial support. His help in providing related reading material was invaluable and is greatly appreciated.

I would also like to take this opportunity to thank Dr. John H. Watkins for many helpful and thought provoking discussions, and his constant support and encouragement. I would like to thank all the members of Dr. Pinizzotto's group, both past and present, for their everyday help and friendship.

Last but not the least, I would like to express my deepest gratitude to my husband, whose support, encouragement, and understanding has helped me reach this point, and my daughter for constantly supporting me and pushing me to finish.

TABLE OF CONTENTS

	Page
LIST OF TABLES	vi
LIST OF ILLUSTRATIONS.....	vii
LIST OF SYMBOLS	xiii
 Chapter	
1. INTRODUCTION	
1.1 Historical Background	1
1.2 General Introduction to Dental Amalgam	2
1.3 The Need for Transmission Electron Microscopy (TEM)	4
CHAPTER 1 REFERENCES	9
 2. OVERVIEW OF AMALGAMATION REACTIONS	
2.1 Introduction	10
2.2 Alloy Particles	11
2.3 Amalgamation Reactions	13
2.3.1 Dissolution of Particles into Mercury	
2.3.2 Nucleation and Growth of Precipitates	
2.4 Reaction Products	19
2.4.1 Ag_2Hg_3 (γ_1)	
2.4.2 $\text{HgSn}_{7.9}$ (γ_2)	

2.4.3	Cu_6Sn_5 (η')	
2.4.4	Ag-Hg (β_1)	
2.5	Previous TEM Studies of Dental Amalgam	22
CHAPTER 2 REFERENCES		29
3. EXPERIMENTAL DETAILS		
3.1	Preparation and Processing of Alloy Particles	31
3.2	Materials	33
3.2.1	Velvalloy	
3.2.2	Tytin	
3.3	Amalgamation Procedure	34
3.4	TEM Sample Preparation	35
3.5	Microstructural Characterization	39
3.5.1	Transmission Electron Microscopy	
3.5.2	Micro-microdiffraction	
3.5.3	Scanning Electron Microscopy	
3.5.4	Indexing of Diffraction Patterns	
CHAPTER 3 REFERENCES		47
4. MICROSTRUCTURE OF A LOW COPPER AMALGAM		
4.1	Introduction.	49
4.2	General Microstructure.	50
4.3	Alloy Particle Microstructure.	51
4.3.1	Ag_3Sn (γ)	

4.3.2	$\text{Cu}_3\text{Sn} (\epsilon)$	
4.4	Matrix Phases.	52
4.4.1	$\text{Ag}_2\text{Hg}_3 (\gamma_1)$	
4.4.2	$\text{HgSn}_{7-9} (\gamma_2)$	
4.4.3	$\text{Ag-Hg-Sn} (\beta_1)$	
4.4.4	$\text{Cu}_6\text{Sn}_5 (\eta')$	
4.5	Reaction Layers.	57
4.5.1	γ/γ_1 Reaction Layer	
4.5.2	γ_2/γ_1 reaction layer	
4.6	Location of Zn.	60
4.7	Summary and Conclusions.	61
	CHAPTER 4 REFERENCES.	84
5. MICROSTRUCTURE OF A HIGH COPPER AMALGAM		
5.1	Introduction	85
5.2	General microstructure	86
5.3	Unreacted Particles	87
5.3.1	$\text{Ag}_3\text{Sn} (\gamma)$	
5.3.2	$\text{Ag}_4\text{Sn} (\beta)$	
5.3.3	$\text{Cu}_3\text{Sn} (\epsilon)$	
5.4	Matrix Phases	90
5.4.1	$\text{Ag}_2\text{Hg}_3 (\gamma_1)$	
5.4.2	$\text{Ag-Hg} (\beta_1)$	

5.4.3	$\text{Cu}_6\text{Sn}_5 (\eta')$	
5.5	The Layer Surrounding Unreacted Particles	92
5.5.1	Ag-Hg-Sn (β_1)	
5.5.2	$\text{Cu}_6\text{Sn}_5 (\eta')$	
5.6	Stability of Phases	94
5.7	Summary and Conclusions	95
	CHAPTER 5 REFERENCES	135
6.	SUMMARY	136
	APPENDIX: ANALYTICAL ELECTRON MICROSCOPY	143
	APPENDIX REFERENCES	161
	BIBLIOGRAPHY	162

LIST OF TABLES

	Page
4.1 Lattice parameters of the phases in Velvalloy.	63
4.2 Ratio of areas of prominent x-ray peaks for Velvalloy.	64
5.1 Lattice parameters of the phases in Tytin.	97
5.2 Ratio of areas of prominent x-ray peaks for Tytin.	98

LIST OF ILLUSTRATIONS

		Page
2.1	Equilibrium Ag-Sn phase diagram.	24
2.2	Cu-Sn equilibrium phase diagram.	25
2.3	Schematic diagram showing the development sequence of the microstructure of low Cu amalgam after mixing lathe cut particles with Hg.	26
2.4	Equilibrium Ag-Hg phase diagram.	27
2.5	Isothermal section of Ag-Hg-Sn ternary phase diagram at 37°C.	28
3.1	Tripod used for TEM specimen preparation.	43
3.2	Sample preparation sequence.	44
3.3	Calibration of microdiffraction.	45
3.4	Indexing of electron diffraction pattern.	46
4.1	SEM image of TEM specimen showing straight edge achieved by mechanical polishing.	65
4.2	Superlattice reflections from three different Ag_3Sn (γ) grains.	67
4.3	Bright field image of part of a large unreacted Ag_3Sn (γ) particle.	68
4.4	Micrograph of matrix illustrating smooth grain boundaries of Ag_2Hg_3 (γ_1) ...	69
4.5	Diffraction patterns from Ag_2Hg_3 (γ_1)	69
4.6	TEM micrograph of Ag_2Hg_3 (γ_1) grain showing small Ag_3Sn (γ) grains inside.	70

4.7	Irregular grain boundaries between Ag_3Sn (γ) and Ag_2Hg_3 (γ_1)	71
4.8	Bright field image of thin regions showing equiaxed Ag-Hg-Sn (β_1) crystals	73
4.9	A sketch of reaction layer between γ_1 and γ_2	75
4.10	TEM micrograph of $\text{HgSn}_{7.9}$ (γ_2) showing amorphous layer between γ_2 and Ag_2Hg_3 (γ_1).	76
4.11	Single crystal pattern of γ_2 illustrating streaks and ZnO diffraction rings. . . .	77
4.12	Bright field TEM image of a small cluster of Cu_6Sn_5 (η') equiaxed grains found in the matrix.	78
4.13	SADP from a Cu_6Sn_5 (η') grain showing superlattice reflection.	79
4.14	SADP from Ag_3Sn (γ) crystal indicating presence of Cu_6Sn_5 (η').	80
4.15	Sketch and image of the reaction layer between γ and γ_1	81
5.1	Backscattered SEM image of a TEM Tytin sample and schematic diagram . .	99
5.2	Diffraction patterns obtained from alloy particles verifying Ag_3Sn (γ).	101
5.3	Backscattered electron image in SEM of the alloy particle.	102
5.4	TEM bright field micrographs showing varied microstructure from outer regions of particles to inner regions	103
5.5	TEM images 200,000x magnified show different microstructure in alloy particles	105
5.6	Low magnification TEM image of alloy particle and SADP from the same area	108
5.7	Bright/dark field images of the particle with diffraction pattern	109

5.8	Bright field image from particle showing dislocation bands	111
5.9	$\mu\mu$ D can be indexed as Ag_3Sn (γ) with zone axis as $[\bar{3} \ 1 \ 2]\gamma$ or as Ag_4Sn (β) with zone axis $[2 \ \bar{1} \ \bar{1} \ 3]\beta$	112
5.10	SADP from a particle showing $[1 \ 0 \ 0]\gamma$ zone axis pattern superimposed with $[0 \ 0 \ 0 \ 1]\beta$ pattern	112
5.11	SEM backscattered image showing blocky morphology of Cu_3Sn (ϵ) and TEM image of particle at 60,000x showing discrete Cu_3Sn (ϵ) grains	113
5.12	Bright field TEM images of Cu_3Sn (ϵ) grains showing heavily twinned and/or faulted substructure	115
5.13	$\mu\mu$ D pattern from Cu_3Sn (ϵ), $[1 \ \bar{1} \ \bar{1}]\epsilon$ and Cu_6Sn_5 (η') $[2 \ \bar{3} \ 1 \ 2]$ with bright field TEM image showing the morphology of Cu_6Sn_5 (η')	117
5.14	Bright field image from a particle showing Moire fringes and dark field image showing small precipitates of ϵ	118
5.15	Bright field image from particle showing Moire fringes and SADP showing extra diffraction spots from ϵ precipitates	121
5.16	SADPs from Ag_2Hg_3 (γ_1)	123
5.17	TEM image from Ag_2Hg_3 (γ_1) with no obvious crystallographic defect showing Cu_6Sn_5 (η') precipitates	124
5.18	Some grain boundaries of Ag_2Hg_3 (γ_1) indicate another phase	125
5.19	Bright field image of Ag-Hg (β_1) and SADP $[2 \ \bar{1} \ \bar{1} \ 0]$	127
5.20	Ag_2Hg_3 (γ_1) matrix region showing a number of small rod shaped Cu_6Sn_5 (η') precipitates	128

5.21. SEM showing location of large Cu_6Sn_5 (η') around unreacted particles and TEM image of Cu_6Sn_5 (η') growing on unreacted particle	129
5.22 Large Cu_6Sn_5 (η') grain including γ and γ_1 grains inside it and SADPs from the same grain not showing superlattice reflections	131
5.23 Cu_6Sn_5 (η') grain growing in the particle and SADP from the same grain showing superlattice reflections, $[\bar{2} \ 4 \ \bar{2} \ 3]$	133
5.24 SADP from a particle showing SnO_2 rings after storing TEM sample for 10 months	134
A.1 Diagrams showing the relevant cone angles in TEM and STEM modes	154
A.2 Signals produced from the interaction of a high energy electron beam with a crystalline sample	155
A.3 Characteristic x-ray generation and nomenclature of x-ray lines	156
A.4 The electron beam/sample interaction volume showing the approximate spatial resolution of x-ray analysis in thin and bulk samples	157
A.5 The effect of varying the beam convergence angle 2α on the type of CBDP . .	158
A.6 Ray diagram of micro-area electron diffraction	159
A.7 Probe diameter and angular resolution	160

LIST OF SYMBOLS

γ	Ag_3Sn
β	Ag_4Sn
γ_1	Ag_2Hg_3
γ_2	HgSn_{7-9}
β_1	Ag-Hg
β_1	Ag-Hg-Sn
ϵ	Cu_3Sn
η'	Cu_6Sn_5
η	Cu_6Sn_5

CHAPTER I

INTRODUCTION

1.1 Historical Background

Intermetallic compounds are used in dentistry in different forms, for example, for crowns, bridges, braces and to repair cavities. When Ag-Sn alloy particles are mixed with liquid Hg, the resulting mixture is called dental amalgam. Dental amalgams are the oldest intermetallic compounds in use for restoring tooth cavities. The plastic consistency of the initial mixture allows the dentist to compact the material into the cavity where it solidifies and hardens by chemical reaction.

Dental amalgams have been used as tooth fillings starting from about 659 A.D. Although it is not known who actually discovered its composition, Chinese artisans of the Tang dynasty have been recorded to have used dental amalgams for “decorative artwork.” Su Kung was the first person to document this alloy in the book commonly known as “*materia medica*.”¹ Su Kung described the alloy composition, method of preparation and mixing, and its ability and usefulness in repairing decaying teeth. The next mention of a dental amalgam refers to a copper amalgam based on the compound Cu_4Hg_3 , used in Europe in the 16th Century. Although there is no documentation of the amalgams used, it would be safe to assume that the artisans using these amalgams passed on their skills, recipes, and alloy compositions to their apprentices.¹ The next mention of dental amalgams in the literature extends back to the year 1819, when a Mr. Bell introduced a

silver amalgam in England which came to be known as Bell's putty. Mr. M. Taveau, of Paris, is said to have been a pioneer in the use of silver amalgams for dentistry in the year 1826.^{1,2}

Systematic experimental work on dental amalgams was started by G.V. Black, a dentist and self-taught metallurgist.^{1,2,3} He started his experiments by comparing two amalgams having the same composition, but prepared by different methods. He was also the first person to systematically study dimensional changes in amalgams as they harden. He empirically determined the composition which results in minimal dimensional change. His observation that an amalgam should contain about 25% tin to be dimensionally stable is valid even today.

In 1929, the American Dental Association approved an alloy similar in composition to the one determined by G.V. Black, listed in the Specification for Dental alloys. In 1963, Youdelis and Innes developed a high-copper content amalgam which was the next major development in the pursuit of better amalgams.⁴ It was not until 1970 that it was shown that restorative work done using high copper amalgams was clinically superior to low copper amalgams, especially in resisting marginal breakdown.

1.2 General Introduction to Dental Amalgam

The Cu concentration in the initial Ag-Sn particles is used to classify amalgams into two major categories. Alloy particles can be produced either by water or gas atomization or by lathe-cutting of an ingot. The preparation of alloy powder is described in Chapter 3. In general, when the Cu concentration is less than 6 wt. % in the particles,

the alloy is known as a low-Cu alloy, whereas an alloy containing more than 8-10% Cu is termed a high-Cu alloy.² Commercially, two forms of high-Cu powder are produced: admixed and single composition. The first form of high-Cu amalgam introduced by Innes and Youdelis contains two types of particles of different compositions: (1) spherical eutectic Ag-Cu particles and (2) lathe-cut, low-Cu, Ag-Sn particles. The second form of alloy powder, developed later, contains particles of a single ternary composition, Ag-Sn-Cu. The chemical composition (wt%) of the main constituent elements in low-Cu alloy powder is in the range of: Ag, 66.7-72.5; Sn, 24.3-27.6; and Cu, 1.2-5.5. The range in high-Cu powder is: Ag, 39.9-70.1; Sn, 17.0-30.2; and Cu, 9.5-29.9. In addition to these major alloying elements, many alloys contain a small amount of Zn, usually between 0.01 and 2.0 wt%.²

When liquid Hg reacts with the Ag-Sn-Cu alloy particles, both Ag and Sn, and probably Cu, dissolve into the Hg. Hardening of amalgams occurs by four mechanisms: (1) dissolution of the Ag-Sn-Cu alloy particles into liquid Hg; (2) nucleation of precipitates in the liquid; (3) growth of the precipitates until the microstructure solidifies; and (4) diffusion of Hg and Sn in the solid amalgam. During these reactions, the alloy powder and all precipitates coexist with liquid Hg, retaining the plastic consistency of the mixture for a short period of time, approximately 10-15 minutes depending on the alloy system. The material completely solidifies within 3-10 hours. A hardened amalgam contains approximately 30% unreacted Ag-Sn-Cu particles dispersed in the microstructure, since the mixture of Hg and alloy particles does not contain enough Hg to consume all of the powder. The Hg-deficiency is intentional so that the remaining

unreacted particles strengthen the amalgam.

X-ray diffraction (XRD), optical microscopy (OM), and scanning electron microscopy (SEM) have been used to determine the microstructure of fully hardened low-Cu amalgams. They consist of unreacted Ag-Sn-Cu (primarily Ag_3Sn (γ)) alloy particles in a matrix of Ag_2Hg_3 (γ_1) and $\text{HgSn}_{7.9}$ (γ_2).³ In high-Cu amalgams, Cu has the lowest solubility in Hg and will precipitate first as rod-shaped Cu_6Sn_5 (η') precipitates. Later, the Ag_2Hg_3 (γ_1) forms around the Cu_6Sn_5 (η') precipitates. Up to 2-3 wt. % of the Cu in the alloy particles can dissolve in the Ag_3Sn (γ). The remainder occurs in the Cu_3Sn (ϵ) phase. Since Sn is scavenged by the Cu, only a small amount of $\text{HgSn}_{7.9}$ (γ_2) will form in high-Cu amalgams. After the introduction of high-Cu amalgams, low-Cu amalgams became less popular due to their inferior chemical and mechanical properties, which result in inferior clinical performance.² The phases present in the alloy particles, phase diagrams, amalgamation reactions, and reaction products are discussed in detail in Chapter 2.

1.3 The Need for Transmission Electron Microscopy (TEM)

Dental amalgams have been used for long time and, as described above, researchers have studied amalgams in detail since the 1880s. An understanding of microstructural development in amalgams is necessary to improve their physical, mechanical, and clinical properties. The microstructures of commercial amalgams and the sequence of reactions which cause amalgams to harden are mostly understood.⁵ However, in previous studies, the limitations of XRD, OM, and SEM have prevented

detailed characterization of some important and interesting aspects of amalgam microstructure.

The presence of Ag-Hg (β_1) in freshly made amalgams has not been clearly established. The classical techniques used to detect the presence of small volume fractions of β_1 in amalgams suffer from ambiguities. XRD spectra are complicated by the fact that most β_1 peaks coincide with peaks due to Ag_3Sn (γ). Moreover, x-ray energy dispersive spectroscopy (XEDS) analyses in the SEM are limited by inadequate spatial resolution to reliably discriminate small volumes of Ag-Hg (β_1) from the surrounding phases. Since the Ag-Hg (β_1) and Ag_3Sn (γ) phases have different crystal structures, single crystal electron diffraction in the TEM should be able to distinguish these phases within the general amalgam microstructure.

In producing the alloy, Zn is often added to the molten metal to prevent oxidation during melting.⁴ It has been reported that compressive strength, and creep, and fatigue resistance increase with increasing Zn content.^{6,7} Because the amount of Zn in the alloy is small, the effect of Zn on the microstructure cannot be determined using SEM/XEDS. The superior spatial resolution and analytical capabilities of TEM are needed to determine the influence of Zn on the microstructure of dental amalgam.

One of the important methods used to elucidate the amalgamation mechanisms is to study the reaction zones between the Ag-Sn-Cu alloy particles and the Ag_2Hg_3 (γ_1) matrix. High-Cu amalgam reaction zones have been studied using the SEM and its associated techniques.⁸ Mahler reported that in high-Cu amalgams an inner and an outer reaction layer exist. He reported that the inner layer, i.e., adjacent to the Ag-Sn-Cu

particles, is a mixture of γ_1 and possibly Ag-Hg (β_1), while the outer layer consists mainly of Cu_6Sn_5 (η').⁹ Okabe also suggested that the reaction layer is not a single phase structure.¹⁰ An ultrastructural study of the Ag_3Sn (γ)/ Ag_2Hg_3 (γ_1) reaction zone would be helpful in explaining the reaction mechanisms of low-Cu and high-Cu amalgams, and should definitively determine the existence of β_1 in the reaction zone.

The only previous transmission electron microscopy (TEM) study of amalgams¹¹ reported in the literature examined high-Cu amalgams, but did not completely characterize the reaction zones. However, fine Cu_6Sn_5 (η') rods were observed in the reaction zones between the alloy particles and matrix. While high-Cu amalgam reaction zones are thick enough to be observed even in the SEM, no previous studies have found or examined low-Cu amalgam reaction zones.

Only two publications by Boswell report the results of transmission electron microscopy (TEM) study of dental amalgams. Both deal with high-Cu amalgams.^{11,12} No TEM studies of low-Cu amalgam have been found. In the high-Cu amalgam studies, various features that could not be found in a usual SEM examination were reported. In particular, the TEM results verified the dissolution/precipitation mechanism of microstructural formation proposed by Waterstrat and Okabe:⁵ the alloy particles dissolve in the liquid Hg, followed by precipitation of the intermetallic phases from solution.

1.4 Objectives of This Study

The primary goals of this research are to observe, document, and microstructurally characterize different commercially used dental amalgams, and explain their properties

and strengthening mechanisms. The distribution of phases and their morphology within the overall amalgam microstructure would help to explain the reaction mechanisms in amalgam formation.

Sample preparation has been the major difficulty in the TEM study. A new method for preparing the samples for TEM examination has been developed and perfected. Samples were prepared using a mechanical “tripod” polisher. Chapter 3 gives a complete description of the technique.

Previous characterization studies of dental amalgams were performed using XRD, OM, and SEM. As described above, the studies using TEM have been very limited. In the present study, the microstructures of amalgams were examined using TEM and its associated micro-analytical techniques which offer superior spatial resolution. In particular, all phases were analyzed using a combination of focused beam micro-microdiffraction ($\mu\mu\text{D}$) and XEDS in the scanning transmission electron microscopy (STEM) mode. Using these techniques, spatially restricted phases, particularly in the reaction layers, could be characterized and compositional changes across individual phases could be recorded. The data from these two microanalytical techniques were simultaneously recorded from areas of the thin foil about 20 nm in diameter.

A low-Cu amalgam, Velvalloy, was examined as the first step of our comprehensive analytical TEM study of dental amalgams, since understanding the structure of this type of amalgam is a prerequisite to examining amalgams with more complex microstructures. The results of Velvalloy study, are discussed in Chapter 4. Single crystal patterns and XEDS were obtained from all phases. TEM results were

compared to those previously reported in literature and were found to be consistent. Finer details of the microstructure were observed.

After a successful study of low-Cu amalgam, Tytin, a high-Cu amalgam was examined. The microstructural analyses of Tytin are discussed in Chapter 5. The Tytin microstructure is compared to the microstructure of Velvalloy to explain its superior mechanical properties.

This microstructural study will be a helpful basis for studying more complex amalgams, e.g., admixed high-Cu and In-containing amalgams, in the future.

CHAPTER 1 REFERENCES

1. R.M. Waterstrat, J. O. M **42**, 8 (1990).
2. T. Okabe, in *Encyclopedia of Materials Science and Engineering*, edited by R. W. Cahn (Pergamon Press, Oxford), Suppl. Vol. 2, 866 (1990).
3. T. Okabe, R. J. Mitchell, M. B. Butts, and C. W. Fairhurst, *Microstructural Science* **7**, 165 (1979).
4. R.W. Phillips, *Skinner's Science of Dental Materials*, (Saunders Company, West Washington Square, PA 19105, 1982).
5. R. M. Waterstrat and T. Okabe, *Intermetallic Compounds* (John Wiley & Sons Ltd., 1994), Vol. 2, p. 575 (1994).
6. J. H. Watkins, H. Nakajima, K. Hanaoka, L. Zhao, T. Iwamoto, and T. Okabe, *Dent. Mater.* **11**, 24 (1995).
7. L. B. Johnson and G. C Paffenbarger, *J. Dent. Res.* **59**, 1412 (1980).
8. T. Okabe, R. Mitchell, M. B. Butts, J. R. Bosley, and C. W. Fairhurst, *J. Dent. Res.* **56**, 1037 (1977).
9. D. B. Mahler and J. D. Adey, *J. Dent. Res.* **63**, 921 (1984).
10. T. Okabe, Manuscript prepared for the proceedings of the Satellite Symposium, "*Setting mechanism of dental materials*", in Glasgow, Scotland, U.K.; co-sponsored by GC Corporation, The Dental Materials Group, IADR and The Academy of Dental Materials (1992).
11. P. G. Boswell, *Scripta Metallurgica* **13**, 383 (1979).
12. P. G. Boswell, *J. Mat. Sci.* **15**, 1311 (1980).

CHAPTER 2

GENERAL OVERVIEW OF AMALGAMATION

REACTIONS AND PHASES

2.1 Introduction

The physical and mechanical properties of amalgams are governed by their microstructures. The properties of multiphase materials depend on the morphology and the amount of each different phase. A basic tenet of materials science is that material properties can be changed and controlled by altering the microstructure.

Amalgam microstructures have been studied for more than a century. Optical microscopy (OM), x-ray diffraction (XRD), and scanning electron microscopy (SEM) have provided a thorough knowledge and understanding of amalgams and have helped to improve their clinical properties. The clinical properties of amalgams that enable them to withstand marginal fracture, microleakage, and corrosion make them a unique restorative material. The use of amalgams have been declining due to possible toxicity of mercury. At the present time, there is no other acceptable alternate material with similar properties and economical like dental amalgams. Various review papers have been written^{1,2} and the recent review papers by Mitchell and Okabe^{3,4} explain the amalgam setting reactions in detail.

This chapter is a brief summary of some of the previous important amalgamation studies and the proposed reaction mechanisms based upon them. The phases and the

microstructures of particles and mixed amalgams are presented in separate sections. Relevant phase diagrams are used for defining phases at various temperatures and within compositional ranges. Many phases are unstable upon cooling. Dental amalgams age at body temperature (approximately 37°C), hence the phases which are stable at 37°C are of interest for this work. Throughout this study, samples were stored at room temperature (25°C), which is slightly lower than body temperature. Since all the phases found in dental amalgams are stable below 100°C, storing the samples below 37°C does not alter the microstructure. Since this dissertation covers two types of dental materials, low-Cu amalgam and single composition high-Cu amalgam, only these two materials will be discussed.

2.2 Alloy Particles

In 1896, G.V. Black gave the chemical composition of alloy powder in wt% as either 68.5% Ag, 25.5% Sn, 5% Au, and 1% Zn, or 68.5% Ag, 25.5%Sn, 4%Au, 1% Zn, and 1% Bi. Except for the addition of a small amount of Cu, the composition of low-Cu alloy powder has not changed significantly. Currently used alloy powder compositions were specified in Chapter 1.⁵ Black empirically concluded in his metallurgical studies that dimensional changes in hardened amalgam were influenced by the amount of Sn in the alloy. His findings were: (1) more than 30% Sn results in shrinking, and (2) less than 25% Sn produces expansion.⁶ His conclusion that amalgam alloy should contain approximately 25% Sn for minimal dimensional change remains in effect.

The phase diagram of the silver-tin system was given by Murphy in 1926.⁶ Fig.

2.1 is the equilibrium binary phase diagram of the silver-tin system. Since Ag and Sn are the major components of the amalgam alloy particles, it is necessary to understand the phase relations shown in this diagram at 37°C.

The composition of low-Cu alloy falls in the $\beta+\gamma$ and γ areas of the diagram, which are shaded and marked ABCDE. The compositions of commercial alloys lie between B and C, 24.58 and 27 wt% Sn. At point C, Ag and Sn form an intermetallic compound, Ag_3Sn , the γ phase, with a peritectic reaction at 480°C. A decrease in tin will produce an increase in β at room temperature. If the Sn concentration is more than 26.8 wt%, γ and tin are formed in the particles if the temperature is below 221°C. When such an alloy is mixed with mercury, the excess Sn leads to an increase in the amount of tin-mercury phase (γ_2) in the amalgam matrix. $\text{HgSn}_{7.9}$ (γ_2) is the weakest and the most corrosive phase in the amalgams and is discussed later in this chapter.

X-ray diffraction and other studies have shown that primarily γ phase is present in commercial amalgams. A solid solution of Ag-Sn (the β phase, hexagonal close-packed) is also present. Addition of a small amount of Cu to Ag-Sn alloy particles results in Cu replacing Ag atoms. In single composition high-Cu alloy particles, the Cu forms a Cu-Sn phase when the amount of Cu in Ag_3Sn is greater than its solubility limit in γ (approximately 1%).¹ This phase can be ϵ Cu-Sn (Cu_3Sn , orthorhombic) or η' (Cu_6Sn_5 , NiAs-type, hexagonal) at room temperature. Fig. 2.2 is a phase diagram of the Cu-Sn binary system. Cu_3Sn (ϵ) forms at 676°C. Cu_6Sn_5 (η) forms from a peritectic reaction at 415°C and transforms to an ordered form (η') below 227°C. Cu reacts with Sn during amalgamation to form η' which eliminates the undesired $\text{HgSn}_{7.9}$ (γ_2) phase. Sometimes,

other elements such as Au, Pd, and Mn are also added to eliminate the γ_2 phase.

Some high-Cu powders contain alloy particles other than the conventional low-Cu Ag-Sn base, such as the Ag-Cu eutectic. Amalgams prepared from these powders are known as admixed amalgams. The structure of the Ag-Sn particle is the same as described above, but Ag-Cu particles contain alternating lamellae of α -Ag and α -Cu, which is typical for eutectic decomposition. When Zn is present in the particles, it can form Cu_3Zn_8 if the Zn concentration is large.⁷

2.3 Amalgamation Reactions

2.3.1 Dissolution of Particles in Mercury

The amalgam matrix and alloy are both considered to be nonequilibrium structures.^{2,4} The setting reaction of an amalgam starts with dissolution of the alloy particles in liquid Hg. There have been a number of studies on the dissolution of pure metals such as Sn, Pb, and Zn in mercury using Berthoud's method as adapted by Moelwyn-Hughes.^{2,5} The rate equation is defined as:

$$\frac{dC}{dt} = \frac{KA}{V} (C_{sat} - C) \quad (1)$$

The solution of the above equation is

$$C = C_{sat} (1 - e^{-KAH/V}) \quad (2)$$

where,

C = concentration of the solute in the liquid at a given time t

C_{sat} = saturation concentration of the solute in the liquid

K = rate constant

A = surface area of the solid exposed to the liquid

V = volume of the liquid

t = time.

Two factors that affect the rate constant K are: (1) the release of solute atoms from the surface of the solid, and (2) migration of atoms through the diffusion layer formed between the solid and the liquid. If D is the diffusion coefficient for solute atoms in the liquid and δ represents the thickness of the diffusion layer surrounding the solid, $K = D/\delta$. Hence, particle dissolution is restricted by the diffusion of solute atoms through the layer.

These two equations explain the setting reaction of amalgams and the dissolution rate of the alloy particles. Smaller amounts of mercury (V), and larger surface area of alloy particles (A), both result in a faster reaction.

K is a function of temperature and trituration speed (mixing speed during amalgamation). The diffusion coefficient D increases with temperature, while the thickness of the diffusion layer is reduced with increased mixing speed. Hence, increases in both temperature and mixing increase the ratio D/δ , which results in a faster setting of the amalgam. As will be discussed in Chapter 3, the alloy particle surfaces are cleaned to remove contaminants like oxides because the contaminants slow the dissolution reaction.

Previous dissolution studies using different binary compositions of Ag-Sn alloys in Hg were analysed using Equation (2). It was concluded that the Ag dissolution rate is

not a function of the Ag concentration in the alloy, but the Sn dissolution rate increases with increasing Sn concentration. The dissolution rate constant for Ag is 10^{-4} cm/s. The rate constant for Sn dissolution from γ is approximately 10^{-6} cm/s.⁸

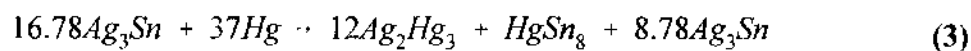
When liquid Hg reacts with the Ag-Sn (+Cu) alloy particles, both Ag and Sn, and probably Cu, dissolve into the Hg. In low-Cu amalgams, Ag reaches supersaturation first, well before the Sn, which causes Ag_2Hg_3 (γ_1) to precipitate before $\text{HgSn}_{7.9}$ (γ_2)⁹ (the solubilities of Cu, Ag, and Sn in Hg are 0.019 at%, 0.66 at%, and 1.68 at%, respectively¹⁰). Precipitated equiaxed Ag_2Hg_3 (γ_1) grains occupy most of the matrix volume. Since Sn has the highest solubility in Hg, $\text{HgSn}_{7.9}$ (γ_2) grains precipitate last, usually as elongated "discrete clumps"¹¹ in open spaces between the Ag_2Hg_3 (γ_1) grains.

Dissolution of Sn from high-Cu alloy particles is different than dissolution of Sn from low-Cu alloy particles. Mitchell et al.¹² carried out a comparative study of two Ag-Sn-Cu alloy powders with 13 wt% Cu and 30 wt% Cu. The results showed that the Sn dissolution rate did not increase with time as in Ag-Sn low-Cu alloy. The initial dissolution rate constant of Sn was approximately 10^{-6} cm/s. After reaching 1/10 of its saturation in Hg, the Sn dissolution rate constant stopped increasing. These findings suggest that due to the gettering action of Cu, the Sn reacts with the Cu and never reaches supersaturation in Hg. This prevents $\text{HgSn}_{7.9}$ (γ_2) from forming. A previous TEM study of admixed high-Cu amalgam by Boswell¹³ suggested that the suppression of $\text{HgSn}_{7.9}$ (γ_2) is determined by the gettering rate of Sn during the growth of the reaction layers formed around the Ag-Cu eutectic particles.

2.3.2 Nucleation and Growth of Precipitates

The amount of each phase in a hardened amalgam depends not only on the dissolution rate and saturation time, but also on the nucleation and relative growth of each phase. Crystal defects, such as grain or interphase boundaries in particles, are fast diffusion pathways for Hg. Since there is a loss of Hg by diffusion into the alloy particles, this reduced amount of solvent results in the supersaturation of Ag and Sn in liquid Hg. The nucleation rates of phases forming in the liquid depend upon the diffusion rate of Hg. Phases can nucleate either homogeneously or heterogeneously from the liquid.

Low-Cu Amalgam: Since the ratio of liquid Hg to alloy particles (1:1) mixed during amalgamation is insufficient to entirely consume the alloy particles, the microstructure of dental amalgams always contains unconsumed alloy particles embedded in the aggregate of the reaction-formed matrix grains, Ag_2Hg_3 (γ_1) and $\text{HgSn}_{7.9}$ (γ_2). During reaction, the alloy powder and all precipitates coexist with liquid Hg, retaining the plastic consistency of the mixture for a short period of time (approximately 10-15 minutes), depending on the alloy system. The material completely solidifies within 3-10 hours. Figure 2.3 illustrates the sequence of amalgamation reactions in Ag-Sn alloys. Low-Cu alloy consists mainly of the Ag_3Sn (γ) phase. The equilibrium reaction can be represented by the following equation:¹⁴

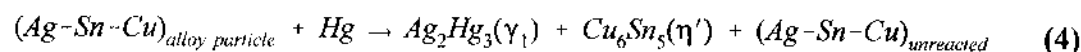


where all the unconsumed particles are considered to be Ag_3Sn and the unreacted 8.78 Ag_3Sn final product is 31% of the volume fraction of the solid amalgam. As explained above, Fig 2.3 shows that due to Ag saturation in liquid Hg, Ag_2Hg_3 (γ_1) nucleates first from the liquid. Later, $\text{HgSn}_{7.9}$ (γ_2) nucleates heterogeneously on γ_1 and alloy particles. Transmission electron microscopy (TEM) study of replicas¹⁵ of the surfaces of low-Cu amalgam suggested that Ag_2Hg_3 (γ_1) nucleates homogeneously from the liquid, whereas $\text{HgSn}_{7.9}$ (γ_2) nucleates heterogeneously. Observations by Reynolds et al.^{16,17} using SEM support this theory. Boswell¹³ argued that for high-Cu alloys, after dissolution of the particles, competitive growth of γ_1 , γ_2 , and η' takes place heterogeneously on the impurity particles present in the liquid Hg and on the unreacted particles.

Okabe et al.¹⁸ and Reynolds et al.¹⁷ reported the growth rate of γ_2 rods to be proportional to $t^{1/2}$. It was also suggested that the growth rate is controlled by the diffusion of Sn atoms in liquid Hg. The early growth of γ_1 in freshly mixed amalgam is difficult to observe because of the time required to obtain a usable vacuum in an SEM. Although the early growth of γ_1 could not be observed in the SEM, Reynolds determined the growth of γ_1 crystals to be proportional to $t^{1/3}$. It is believed that the growth of both phases is controlled by diffusion of Ag and Sn in liquid Hg.

Single Composition High-Cu Amalgam: Since Cu has the lowest solubility in Hg of all component elements of this type of amalgam, Cu_6Sn_5 (η') is the first phase to nucleate from the solution. It can nucleate homogeneously from the liquid or heterogeneously on another solid phase. Later, Ag_2Hg_3 (γ_1) forms around the Cu_6Sn_5 (η') precipitates. Since

Sn is scavenged by the Cu, only a small (or zero) amount of HgSn_{7-9} (γ_2) will form. The reaction of Hg with high-Cu alloy particles can be summarized as:¹⁴



There have been no studies of the growth of γ_1 in high-Cu amalgam, but it is reasonable to believe that the mechanism is similar to that found in low-Cu amalgam.⁴ When sufficient Cu is present in the alloy powder, very little γ_2 is present in the final amalgam microstructure. The presence of Cu delays the supersaturation of Sn in the liquid because Cu removes Sn from the solution by precipitating it as Cu_6Sn_5 (η'). It can be assumed that all the Cu from the dissolved particles reacts with Sn to form Cu_6Sn_5 (η'). Only the remainder of the Sn can precipitate as γ_2 . Assuming that alloy particles contain only Ag_3Sn (γ) and Cu_3Sn (ϵ), the mass of Hg and γ_2 in an amalgam in grams per 100g of alloy powder can be expressed by Jensen's mass analysis of amalgam¹⁹:

$$\gamma_2 = 0.24 (100 - p) y - 0.60 px \quad (5)$$

$$\text{Hg} = 1.72 (100 - p) y - 0.05 px \quad (6)$$

where p is the mass of Cu_3Sn (ϵ) in 100 g of alloy powder, y represents the fraction of γ phase consumed = $(\gamma - \text{unreacted } \gamma)/\gamma$, and x is the fraction of ϵ phase consumed = $(\epsilon - \text{unreacted } \epsilon)/\epsilon$ during amalgamation. After solving these equations, the mass of γ_2 per mass of amalgam can be expressed as:

$$\gamma_2 = \frac{0.24 \text{ Hg} - 1.02 \text{ px}}{(1.72) (10 + \text{Hg})} \quad (7)$$

Equation 7 gives the limiting value of Cu containing phase needed to eliminate γ_2 formation in an amalgam:

$$p \geq \frac{0.235 \text{ Hg}}{x} \quad (8)$$

There are two proposed mechanisms for Cu_6Sn_5 (η') precipitation. Rod-shaped Cu_6Sn_5 (η') may precipitate initially because Cu has the lowest solubility in Hg. Alternatively, dissolved Sn may react with a Cu-containing phase to form Cu_6Sn_5 (η'). Previous studies have suggested that the Cu_6Sn_5 (η') nucleates on Cu_3Sn (ϵ).^{2,4} Okabe's study²⁰ on a fractured surface of freshly mixed amalgam revealed that rod-shaped η' crystals ($0.5\text{-}1.0 \mu\text{m} \times 2.0\text{-}3 \mu\text{m}$) formed after 9 minutes of trituration. This was the fastest they could image the amalgam in an SEM. It appeared that η' never grew after that, but polyhedral-shaped γ_1 crystals grew around the η' for up to 30 minutes after trituration.

2.4 Reaction Products

2.4.1 Ag_2Hg_3 (γ_1)

Fairhurst in 1966²¹ determined the crystal structure of the γ_1 phase as cubic and its chemical composition as Ag_2Hg_3 . Andersen and Jensen²² gave the chemical composition as $\text{Ag}_{11}\text{Hg}_{15}$. Later, Jensen²³ suggested that γ_1 is stable from 68 wt% Hg to 72 wt% Hg.

The phase diagram in Fig. 2.4 illustrates that γ_1 may be in equilibrium with either Ag-Hg (β_1) or liquid mercury for compositions between 68 wt% to 72 wt% Hg at room temperature. Sn has some solubility in Ag_2Hg_3 (γ_1) and in dental amalgams γ_1 is considered a ternary Ag-Sn-Hg phase. Microprobe analysis by Mahler et al. determined the solubility of Sn in Ag_2Hg_3 (γ_1) as 1.6 wt%.²⁴ Most other results give a Sn solubility between 1 and 2 wt% Sn in Ag_2Hg_3 (γ_1). However, values of 8.5 wt%, 3.1 wt%, and 2-3 wt% have also been reported.⁴ Ag_2Hg_3 (γ_1) grains are equiaxed and approximately 1-2 μm across.²⁵ The size of the Ag_2Hg_3 (γ_1) grains influences the creep characteristics of the amalgam, but the factors controlling the γ_1 grain size are not yet understood. Dependence on the composition and microstructure of the alloy particles is assumed.

2.4.2. $\text{HgSn}_{7.9}$ (γ_2)

Gayler²⁶ identified the $\text{HgSn}_{7.9}$ (γ_2) phase in amalgams as forming from a peritectic reaction at 213.9°C. Fairhurst and Ryge²⁷ determined its crystal structure by x-ray diffraction. They concluded that there is only one Sn-Hg phase at room temperature. It is a hexagonal structure with $c/a = 0.931$. Other low-Cu amalgam studies showed that γ_2 contains between 16.8 and 17.3 wt% Hg. It is believed (according to the Sn/Hg ratio) that dental amalgam contains $\text{Sn}_7\text{Hg}/\text{Sn}_8\text{Hg}$. Other x-ray diffraction investigations have also confirmed the presence of only one Sn-Hg phase in amalgams. A differential scanning calorimetry study by Sarkar²⁸ suggested another Sn-Hg phase exists with an orthorhombic crystal structure. This is still a controversial subject.

In low-Cu amalgam, as discussed before, Sn becomes supersaturated later in time

than Ag. Less Hg is left after the formation of Ag_2Hg_3 (γ_1) and diffusion of the Hg into the alloy particles. Loss of Hg results in supersaturation of Sn and the subsequent formation of $\text{HgSn}_{7.9}$ (γ_2).

2.4.3. Cu_6Sn_5 (η')

The structure of Cu_6Sn_5 is of the NiAs type with $a = 4.19 \text{ \AA}$ and $c = 5.086 \text{ \AA}$ ($c/a=1.214$). The high temperature η -phase transforms from an unordered phase to a long-period superlattice η' -phase at approximately 227°C .²⁹ The unit cell of the η' superlattice is about 5 times larger than the unit cell of η . **Previous studies in dental amalgams did not make any effort to distinguish between η and η' .** Since the amount of η' is very small in low-Cu amalgam, its location and morphology are not very well defined. In high-Cu single composition amalgams, η' forms as clusters of rods (0.1-0.5 μm diameter).³⁰ η' crystals are also scattered in the matrix, but higher concentrations of η' were found around unreacted particles. The sizes of the η' crystals depends on the microstructure of the alloy particle, particularly on the size of the initial Cu_3Sn (ϵ). After observing amalgamation of alloy particles with various sizes of Cu_3Sn (ϵ), it was found that larger η' crystals were produced by increasing the Cu containing phase areas in the particles.³¹ Thus, it was concluded that η' grew on the Cu containing phases.

2.4.4. Ag-Hg (β_1) phase

Since the solidified dental amalgam microstructure described above is a non-equilibrium composite structure, it changes over time at body temperature due to solid-

state diffusion. Some of the notable changes which occur during aging are a reduction in the amount of $\text{HgSn}_{7.9}$ (γ_2) and the formation and growth of a new phase, Ag-Hg (β_1).¹ With regard to Ag-Hg (β_1) formation in amalgams, Aldinger's isothermal section (37°C) of the Ag-Hg-Sn ternary phase diagram³² (Fig. 2.5) suggests that Ag-Hg-Sn (β_1) could be an additional reaction product in fully hardened low-Cu amalgams. This ternary phase is a solid solution of Ag + 15 at% Sn (β) and Ag + 46 at% Hg (β_1); both of these binary phases are more Ag-rich than Ag_3Sn (γ) and Ag_2Hg_3 (γ_1), respectively. In the dental literature, the single Ag-Hg-Sn ternary phase is also known as β_1 . Okabe found ternary β_1 in a γ/γ_1 diffusion couple aged at 60°C for at least one week.³³ Binary β_1 has been found in amalgams aged at room temperature for two years.^{34,35} Some researchers have discovered small Ag-Hg (β_1) grains on the surface of Ag-Sn-Cu particles plated with small amounts of mercury without heating or aging, either by electroplating Hg,³ or by placing the Hg directly onto the surface.³⁶ Possible mechanisms for the formation of β_1 have been suggested in Okabe and Mitchell's reviews.^{3,4} However, the presence of Ag-Hg (β_1) in freshly made amalgams has not been clearly established.⁴ Both of the classical techniques of detecting the presence of small volume fractions of β_1 in amalgams suffer from ambiguities. X-ray diffraction (XRD) spectra are complicated by the fact that most β_1 peaks coincide with peaks due to Ag_3Sn (γ). Moreover, x-ray energy dispersive spectroscopy (XEDS) analyses in the scanning electron microscope (SEM) are limited by inadequate spatial resolution to reliably discriminate small volumes of Ag-Hg (β_1) from the surrounding phases. Since the Ag-Hg (β_1) and Ag_3Sn (γ) phases have different crystal structures, single crystal electron diffraction in the transmission electron

microscope (TEM) should be able to distinguish these phases within the general amalgam microstructure. Such TEM studies will be described in Chapters 4 and 5.

2.5. Previous TEM Studies of Dental Amalgams

The only previous transmission electron microscopy (TEM) study of amalgams by Boswell³⁸ examined high-Cu amalgams. The study did not completely characterize the reaction zones, although fine Cu_6Sn_5 (η') rods were observed in reaction zones between the alloy particles and the matrix. While high-Cu amalgam reaction zones are thick enough to be observed even in the SEM, no studies have found or examined low-Cu amalgam reaction zones. Boswell's TEM results verified the dissolution/precipitation mechanisms discussed above. It was also found that Cu_6Sn_5 (η') suppresses $\text{HgSn}_{7.9}$ (γ_2) formation by gettering the Sn in the liquid solution before Sn reacts with Hg. The majority of Cu_6Sn_5 (η') crystals grow in solution, not via solid-state transformation of Cu_3Sn (ϵ). The growth of the intermetallic in admixed high-Cu amalgam can be described by a parabolic growth law, but the enhanced growth rates observed imply that diffusion occurs via interfaces or grain boundaries rather than through the bulk solid phases. Finally, Boswell's studies showed that Zn appears to suppress faulting within the Ag_2Hg_3 (γ_1) matrix grains, but a specific Zn-rich phase was not identified. Boswell did not propose a mechanism for this observed property of the Zn-additions.

TEM studies of low-Cu and high-Cu amalgams reported in this dissertation are the most complete studies of the details of amalgam microstructure to date.

Ag-Sn

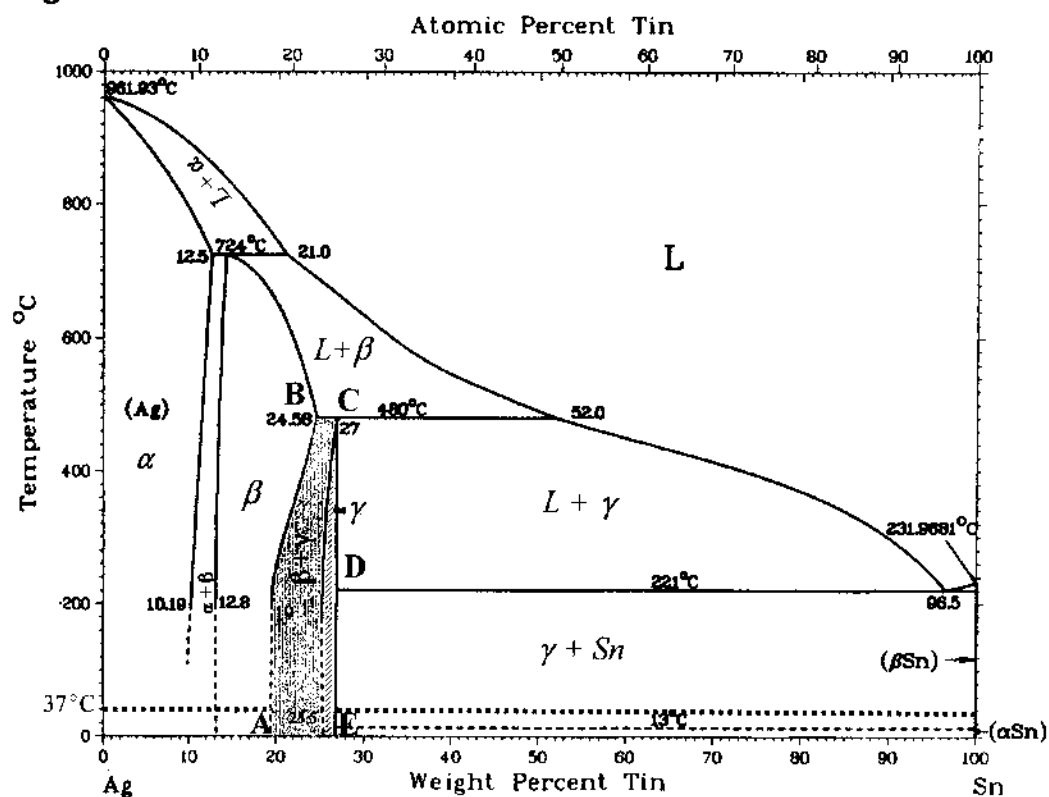


Figure 2.1. Equilibrium Ag-Sn phase diagram. Dental amalgam compositions fall in the shaded area ABCDE.³⁷

Cu-Sn

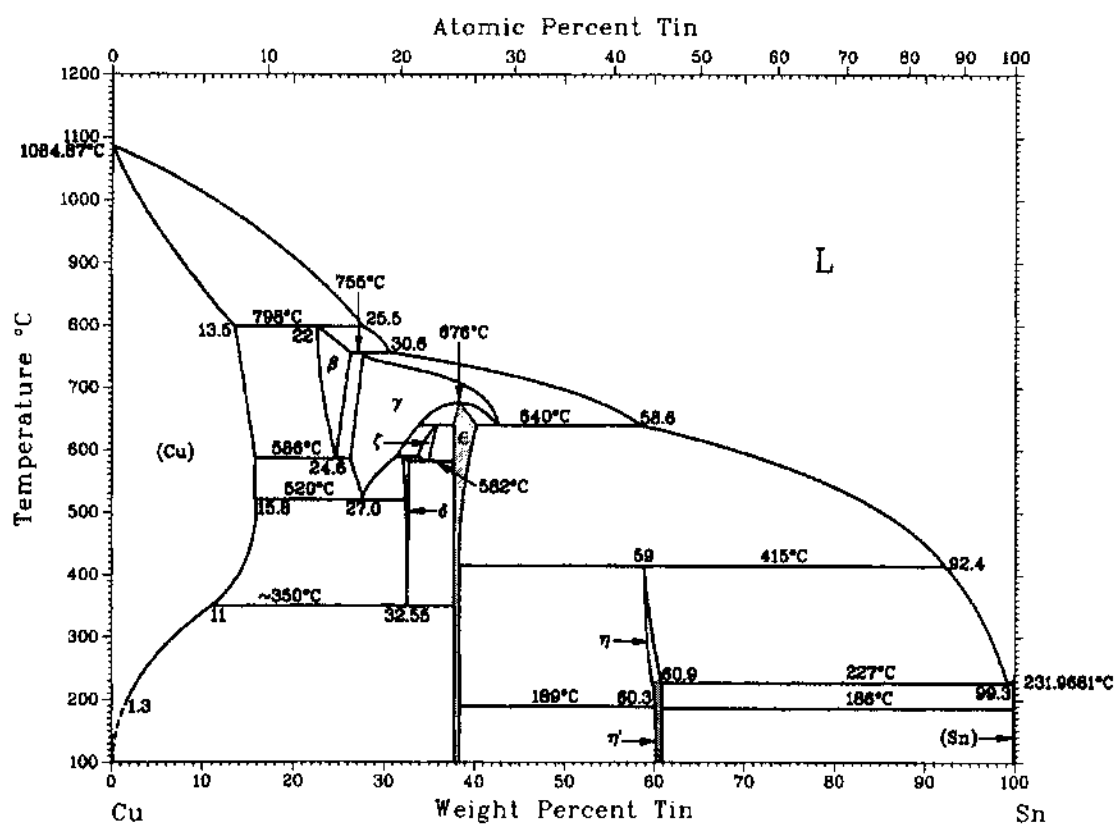


Figure 2.2. Cu-Sn equilibrium phase diagram.³⁷ The ϵ , η , and η' phase fields are shaded.

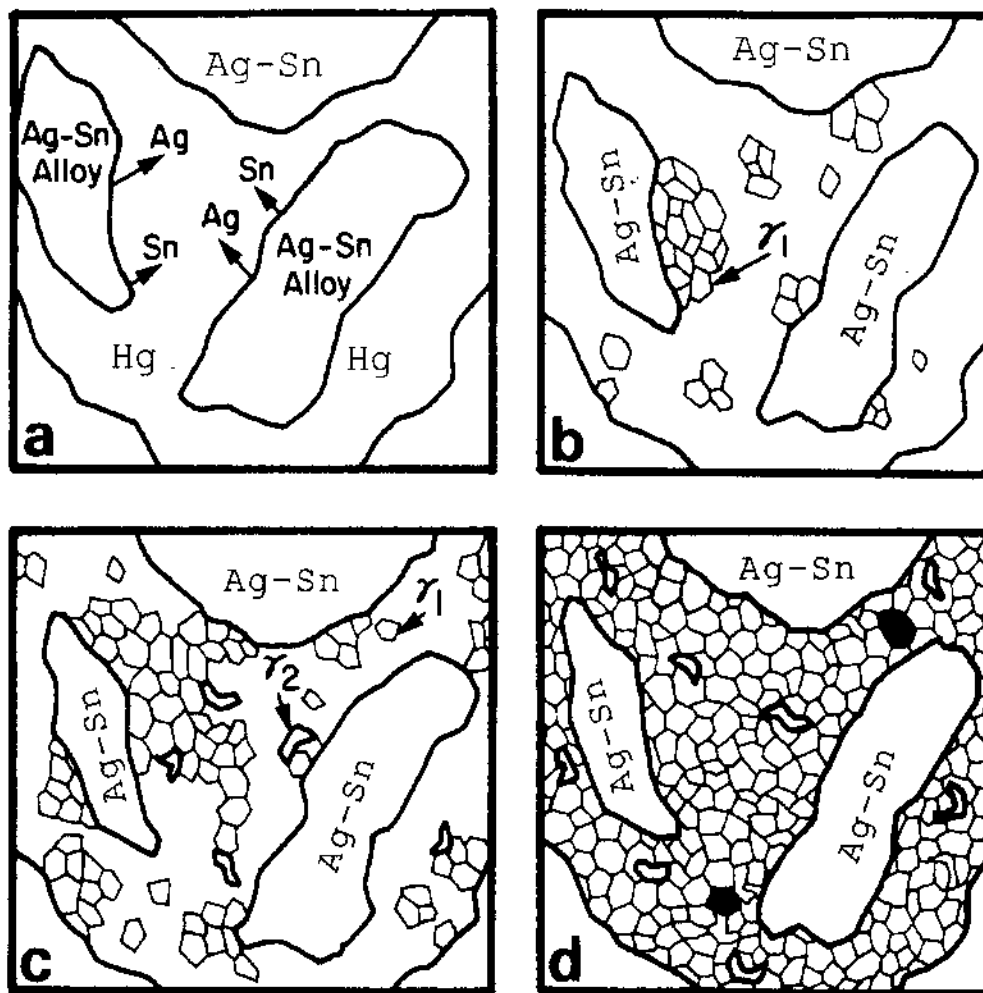


Figure 2.3. Schematic drawings showing the development sequence of the microstructure of low-Cu amalgam after mixing lathe-cut Ag-Sn particles with mercury: (a) dissolution of Ag and Sn in mercury; (b) precipitation of γ_1 from liquid; (c) growth of γ_1 and precipitation of γ_2 ; (d) final hardened amalgam.¹⁴

Ag-Hg

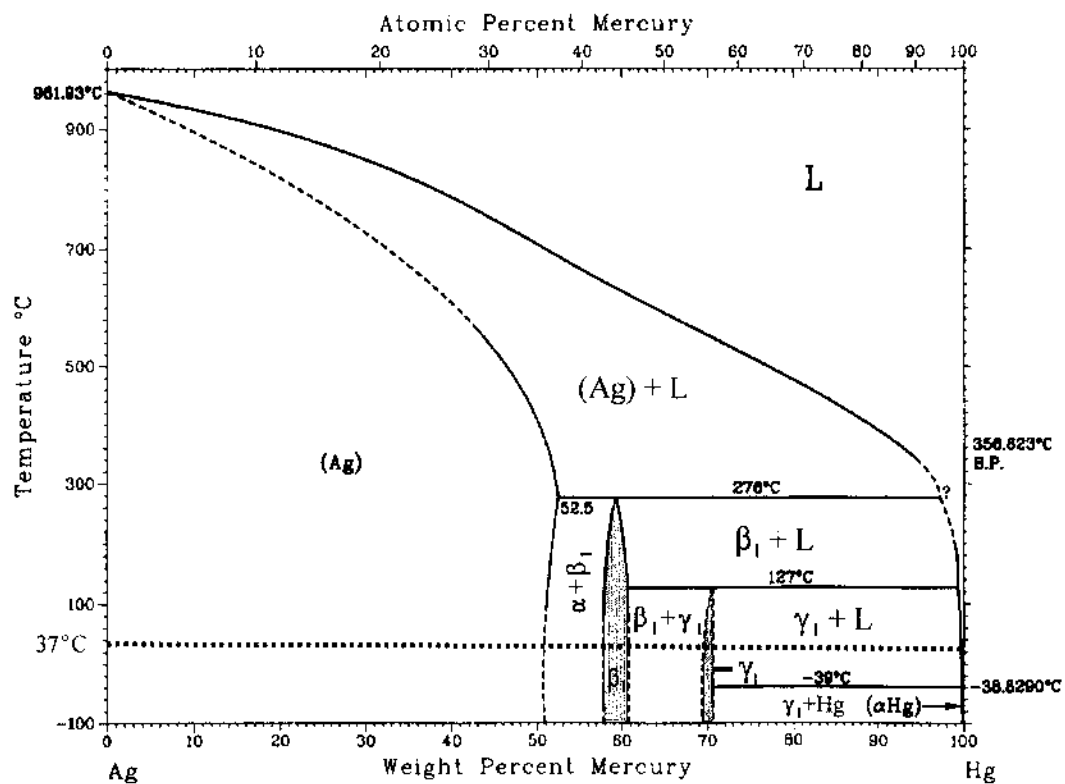


Figure 2.4. The Ag-Hg equilibrium phase diagram.³⁷ The β_1 and γ_1 phase fields are shaded.

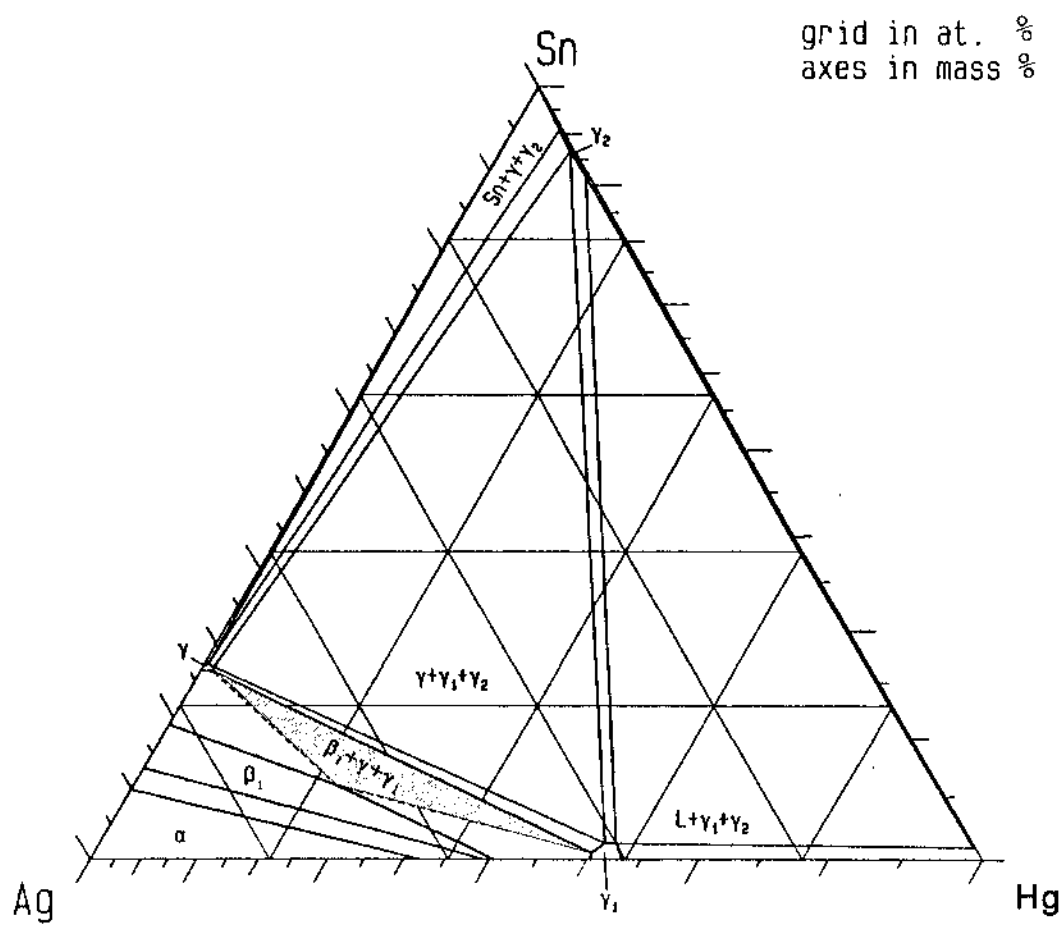


Figure 2.5. Isothermal section of Ag-Hg-Sn ternary phase diagram at 37°C.³² The $\beta_1 + \gamma_1 + \gamma$ phase field is shaded.

CHAPTER 2 REFERENCES

1. T. Okabe, in *Encyclopedia of Materials Science and Engineering*, edited by R.W. Cahn (Pergamon Press, Oxford), Suppl. Vol. 2, 866 (1990).
2. R.M. Waterstrat and T. Okabe, *Intermetallic Compounds* (John Wiley & Sons Ltd., 1994), Vol. 2, p.575.
3. R.J. Mitchell and T. Okabe, Critical Rev. in Oral Biology and Medicine **7**, 12 (1996).
4. T. Okabe and R.J. Mitchell, Critical Rev. in Oral Biology and Medicine **7**, 23 (1996).
5. J.F. DeFreitas, Australian Dent. J. **24**, 17 (1979).
6. R.M. Waterstrat, J. O. M. **42**, 8 (1990).
7. S. J. Jensen, K. B. Olsen, and L. Utoft, Scand. J. Dent. Res. **81**, 572 (1979).
8. R. Mitchell, T. Okabe, and C.W. Fairhurst, J. Dent. Res (Special. Issue. B) **56**, 146 (1977).
9. T. Okabe, R. F. Hochman, and L. O. Sims, J. Biomed. Mater. Res. **9**, 221 (1975).
10. M. Hansen and K. Anderko, *Constitution of Binary Alloys*, (McGraw-Hill, New York 1958).
11. R. W. Bryant, Aust. Dent. J. **29**, 163 (1984).
12. R. Mitchell, T. Okabe, and C.W. Fairhurst, J. Dent. Res. (Special. Issue. A) **57**, 125 (1978).
13. P.G. Boswell, J. Mater. Sci. **15**, 1311 (1980).
14. R.W. Phillips, *Skinner's Science of Dental Materials* (W.B. Saunders Company, West Washington Square, PA 19105, 8th Ed. 1982).
15. E.H. Greener, J.K. Yang, A.A. Grant, and M. Meshii, Aust. Dent. J. Oct., 363 (1968).
16. C.L. Reynolds, Jr., F.E. Wawner, and H.G.F. Wilsdorf, Scrip. Metall. **8**, 657 (1974).
17. C.L. Reynolds, Jr., F.E. Wawner, and H.G.F. Wilsdorf, J. Appl. Phys. **5**, 171 (1975).

18. T. Okabe, A.L. Hines, R.F. Hochman, and L.O. Sims, *Biomed. Mater. Res.* **9**, 389 (1975).
 19. S.J. Jensen, *Scand. J. Dent. Res.* **85**, 297 (1977).
 20. T. Okabe, R.J. Mitchell, M.B. Butts, and C.W. Fairhurst, *J. Dent Res.* **57**, 975 (1978).
 21. C. W. Fairhurst, Ph.D. Dissertation, Northwestern University, IL (1966).
 22. P. Andersen and S.J. Jensen, *Scand J. Dent. Res.* **79**, 466 (1971).
 23. S.J. Jensen, *Scand. J. Dent Res.* **93**, 84 (1984).
 24. D.B. Mahler, J.D. Adey, and J.V. Eysden, *J. Dent. Res.* **54**, 218 (1975).
 25. D.B. Mahler and J.D. Adey, *J. Dent. Res.* **70**, 1384 (1991).
 26. M. Gayler, *J. Inst. Metals* **60**, 376 (1937).
 27. C.W. Fairhurst and G. Ryge, in *Advances in X-ray Analysis*, Plenum Press Vol. 5, 64 (1961).
 28. N.K. Sarkar, *J. Mater. Res: Mater. in Medicine* **5**, 171 (1994).
 29. A. Gangulee, G.C. Das, and M.B. Bever, *Metallurgical Transactions* **4**, 2063 (1973).
 30. T. Okabe, R. J. Mitchell, M.B Butts, and C.W. Fairhurst, *J. Dent. Res.* **57**, 975 (1978).
 31. R.J. Mitchell, T. Okabe, and M.B. Butts, *J. Dent. Res.* **60**, 480 (1981).
 32. F. Aldinger and W. Kraft, *Z. Metallkde.* **68**, 523 (1977).
 33. T. Okabe, F. Ling, and R. F. Hochman, *J. Dent. Res.* **54**, L162, (1975).
 34. L. B. Jonson, Jr., *J. Biomed. Mater. Res.* **1**, 285 (1967).
 35. L. B. Jonson, Jr. , *J. Biomed. Mater. Res.* **1**, 415 (1967).
 36. J. R. Abbott, D. R. Miller, and D. J. Netherway, *J. Biomed. Mat. Res.* **20**, 1391 (1986).
 37. *ASM Handbook*, edited by Hugh Baker, Vol. 3 (ASM International, Materials Park, Ohio 44073, 1992).
 38. P. G. Boswell, *Scripta Metallurgica* **13**, 383 (1979).
-

CHAPTER 3

EXPERIMENTAL DETAILS

3.1 Preparation and Processing of Alloy Particles

Amalgams are prepared by mixing alloy powders with mercury. The clinical properties and quality of performance depend on the manufacturer of the alloy and how they are mixed together by a dentist. The metallurgical aspects which control the mechanical properties are discussed here.

The preparation of alloy powder involves several steps controlled by the manufacturer which greatly influence the properties of the amalgam:

- (1) chemical composition of the alloy powder
- (2) preparation technique, which controls the shape and size of the alloy particles
- (3) heat treatment or annealing of the alloy
- (4) surface chemical treatment.

As per the ADA specifications, the chemical compositions of alloy powders are essentially silver and tin. However, copper, zinc, gold and/or mercury are sometimes included in the alloy, the only caveat being that the amount of silver and tin in any given alloy must be greater than the other included elements. Alloy powders containing greater than 0.01 wt% zinc are designated as “zinc containing.” Powders containing less than or equal to 0.01 wt% zinc are designated as “non-zinc containing.”

Similarly, alloy powders containing less than 6 wt% copper are classified as low

copper alloys, and alloys containing greater than 8-10 wt% copper are generally classified as high copper alloys. Amalgams made from these alloy powders are classified as low copper and high copper amalgams, respectively.

Commercially, two processes are used to prepare amalgam alloy powders:

1) milling or lathe-cutting of a cast ingot, 2) atomization of the molten alloy.

When Ag-Sn (+Cu) is cast into ingots, rapid cooling of the ingots produces an inhomogeneous cored grain structure with varying composition. Therefore, cast ingots are subsequently heated in an oven just below the solidus temperature (480°C) to produce a homogeneous, equilibrium microstructure. Annealing is done for sufficient time to allow atomic diffusion to take place, resulting in equilibrium phases. The cooling of the ingots after homogenizing treatments affects the proportions of the γ and β phases. In general, slow cooling of the ingots produces more of the γ phase than the β phase. This is closer to the expected equilibrium structure at room temperature. On the other hand, rapid quenching below the solidus temperature results in more retained β phase.

Lathe-cut particles are irregularly shaped and vary in size. The particle size is reduced, if required, by ball-milling. Smaller particles require more mercury to produce an acceptable amalgam due to the larger surface area. Hence, the distribution of particle sizes around the average is an important parameter that affects the mechanical properties of an amalgam. Furthermore, cutting and ball milling introduce internal microstresses. When stored, these stresses are relieved through room temperature annealing giving an unstable alloy. In addition, release of these microstresses during mixing with mercury causes a faster amalgamation reaction resulting in dimensional changes during

hardening.¹ Generally, annealing of the alloy particles is performed at approximately 100°C for several hours to develop a stable alloy.

Manufacturers generally use proprietary chemical treatments to remove films formed on the particle surfaces. For some unknown reason, acid washed particles seem to be more reactive during amalgamation than unwashed particles.²

Another production method of amalgam alloy is atomization of liquid metal. This method yields material with more homogeneity in structure and composition without internal stresses. The desired amounts of each element (wt%) are melted together and a continuous stream of liquid metal is broken into fine spherical droplets via a subsonic or supersonic gas stream or jet. Just like the lathe-cut particles, the spherical particles are also given a heat treatment and an acid bath for the reasons explained above. Manufacturers usually supply amalgam powder in the form of pellets or tablets. The alloy powder is put under pressure so that it loosely bonds together. This cohesion can be easily broken down during the amalgamation process.

3.2 Materials

3.2.1 Velvalloy

Velvalloy³ was selected as a material to examine because it is a typical commercial low-Cu amalgam. The alloy particles are produced by lathe-cutting the Ag-Sn (+Cu) ingot as described above. The average alloy particle size ranges between 25-35 μm . The chemical composition of the alloy particles (wt%) is: 70.3% Ag, 25.9% Sn, 2.8% Cu, 0.93% Zn, and 0.1% unknown impurities.⁴

3.2.2 Tytin

Tytin,⁵ a commercially popular “single composition” amalgam, was selected as representative of high-Cu amalgam. Each particle of this alloy has the same chemical composition. Clinical properties of high-Cu amalgams have been greatly improved over time by altering the composition of the alloy powder. Ag-Sn-Cu ternary alloy spherical particles are produced by gas atomization. The chemical composition of the currently used alloy powder is (wt%) 59.3% Ag, 27.1% Sn, 13.3 % Cu, and others (0.0207% Pb, 0.25% Hg).²

3.3 Amalgamation Procedure

A mechanical amalgamator is used to mix the powder or pellets with mercury. The mixing process is known as “trituration.” The alloy particles were vigorously mixed with liquid Hg in a 1:1 ratio for about 10-20 s, as recommended by the manufacturer. The cylindrical amalgam specimens (4 mm in diameter and 8 mm long) were made by compacting (condensing) the plastic mass at 14 MPa in a die following ANSI/ADA procedures.⁶ About 10% of the Hg is extracted during the compaction process. Initial hardening of the amalgam occurs within five minutes, while maximum strength is basically achieved within 24 hours of aging at room temperature. In our experiments, all samples were aged at room temperature for at least a week before TEM sample preparation. TEM samples were stored at room temperature.

3.4 TEM Sample Preparation

TEM sample preparation is the most critical step in this research. Our preliminary experiments revealed that the common techniques for preparing TEM specimens, namely, chemical and mechanical polishing, dimple grinding and ion milling, were unsuccessful when applied to dental amalgams. Chemical polishing was not appropriate since the different phases do not etch uniformly. Due to the different hardnesses of the phases, it is very difficult to homogeneously thin large areas of the sample to electron transparency using standard metallurgical polishing techniques. Dimple grinding introduces significant plastic deformation in soft materials and generally cannot be used without ion milling. We found that ion milling, even when a cold stage was used, did not remove material uniformly, but resulted in the formation of many small holes in the specimen. This is indicative of preferential removal of some phases compared to others, and shows that ion milling can produce artifacts in the specimen. Our TEM examinations of ion milled Velvalloy and Tytin specimens verified the presence of only Ag_3Sn (γ), Ag-Hg (β_1) and Cu_6Sn_5 (η'), but did not reveal the presence of Ag_2Hg_3 (γ_1), which is the major constituent of the matrix. Reynolds⁷ demonstrated that Ag_2Hg_3 (γ_1) partially transforms to Ag-Hg (β_1) at 70°C. Other studies have also proven that amalgams are temperature sensitive.⁸ During ion milling, such moderate temperature increases, especially locally, cannot be eliminated or ignored, even when a cold stage is used. In addition, the Ag_2Hg_3 (γ_1) was found to remain electron opaque after the other phases became electron transparent during ion milling. At longer ion milling times, these thinner phases were obliterated before the Ag_2Hg_3 (γ_1) became electron transparent. For these reasons, ion

milling is not a viable sample preparation methodology for dental amalgams. Therefore, another method of mechanical polishing was developed that completely eliminates the need for ion milling.

TEM specimens were prepared using a modified wedge polishing technique that was originally developed for semiconductors by Klepeis.^{9,10} However, it was found that the diamond lapping films normally used in this technique completely changed the amalgam microstructure, i.e., Ag_2Hg_3 (γ_1) transformed to recrystallized Ag-Hg-Sn (β_1). Hence, the diamond lapping films are too aggressive for use with the relatively soft amalgam. Details of our TEM specimen preparation technique, developed specifically for this study which enabled us to observe all the phases present in the amalgam sample, are presented below.

The cylindrical specimens of Velvalloy were cut into 300-500 μm thick discs using a low speed diamond wafering saw. A tripod from South Bay Technology¹¹ (Fig. 3.1) was used to mechanically polish the specimen into a wedge shape using the following procedure. The rear micrometers (C) were made coplanar with the tripod's glass insert (A). The specimen disc (B) was glued¹² to the glass insert as shown in Fig. 3.1. The specimen was first polished on one side with 1200 grit SiC paper, and 3, 1, 0.25, and 0.05 μm diamond pastes on a "Final A" polishing cloth from Allied High Tech.¹³ The specimen was then removed from the glass insert using acetone, and split approximately in half using a sharp blade to obtain a straight edge. The polished side of the half-moon shaped specimen was again glued to the glass insert of the tripod. Before polishing the reverse side, the rear micrometers of the tripod were advanced 0.5 mm

relative to the glass insert surface to produce a wedge-shaped specimen. The reverse side of the specimen was polished using the same steps described above.

Later in this study, the sample preparation was changed slightly from the technique described for the preparation of Velvalloy samples. The improved tripod polishing technique was developed to obtain thinner and larger electron transparent areas of Tytin samples. We obtained better TEM samples for two reasons: (1) the accuracy of sample thickness measurement increased after each polishing step, and (2) the matrix area in Tytin is easier to polish compared to Velvalloy. This could possibly be due to the fine Cu_6Sn_5 (η') precipitates embedded in the matrix which results in a stronger matrix material.

The tripod polisher was originally designed for preparing semiconductor integrated circuit samples. A glass insert is used to mount the sample and to monitor the thickness of the thin silicon samples which eventually become transparent to visible light. Unfortunately, amalgam samples remain opaque, requiring modifications of the technique. Instead of an L-shaped bracket used in the conventional tripod, an aluminum plate is used as shown in the Fig. 3.2(a). A piece of a glass microscope slide is glued to the plate and the sample is glued onto the glass slide. One side of the sample is polished on 1200 grit SiC, followed by polishing with 3 μm , 1 μm , 0.5 μm , and 0.05 μm diamond pastes. The sample is removed and cut in half. The sample is then glued on the side of the plate as shown in Fig. 3.2(b) to polish the cut edge of the sample to make it flat. The specimen is polished on 1200 grit SiC and with 1 μm diamond paste. The sample is again removed with acetone and is mounted with the originally polished side down and the cut

edge near the edge of the glass slide (Fig. 3.2(c)). The rear micrometers are made coplanar with the surface of the glass slide. A similar type of glass slide is put on the aluminum plate between the rear micrometers to raise it to the level of the other side and the micrometers are adjusted by putting the assembly on a flat surface. The rear micrometers are given the usual extra turn. Now the tripod assembly is ready for final polishing. The sample is polished on 1200 grit SiC until it is 50 μm thick. The sample thickness is monitored with a micrometer across the thickness of the plate. The polishing is done progressively on 3 μm , 1 μm , and 0.25 μm diamond paste to achieve a 25-30 μm thick sample on the thicker edge of the sample. Final polishing is done using 0.05 μm diamond spray.¹³ The final sample is wedge-shaped in cross-section, and is electron transparent along the thinner edge.

The specimen was removed by soaking it in acetone until it separated from the glass insert. To avoid aggressive cleaning methods which might damage the newly thinned wedge tip, the specimen was soaked in alcohol for 5 minutes to dissolve glue residues, and allowed to air dry. Finally, the specimen was carefully mounted in a standard JEOL EM-SCHS TEM sample holder. Sometimes, to prevent breakage, the sample was glued to a nickel or carbon TEM ring and trimmed to a 3 mm outside diameter disc to fit into the double tilt sample holder described below.

3.5 Microstructural Characterization

3.5.1 Transmission Electron Microscopy

Transmission electron microscopy (TEM) was the principal characterization technique used for our microstructural studies of amalgam samples. Due to the complexities of the microstructures, a combination of different TEM techniques was adopted for this work. Each of the techniques used and its objective are briefly described below. Since amalgams have more than six major phases, and since more than one phase have similar interplanar spacings and angles between the diffracting crystallographic planes, conventional bright field imaging and x-ray energy dispersive spectra (XEDS) were insufficient to identify all phases. Furthermore, some phases like Ag_3Sn (γ) and Ag_4Sn (β) yield similar XEDS spectra. In these cases, one crystal orientation was insufficient for phase identification. Controlled tilting of the sample to multiple orientations was performed to confirm the crystallography of the phase.

The completed TEM samples were examined using a JEOL 200CX operating at 200 kV. It has 1.4 Å lattice resolution and 3.5 Å point-to-point resolution. A standard JEOL EM-SCHS carbon sample holder was used for x-ray microanalysis. A JEOL double-tilt holder model number EM-BST with beryllium sample cups was used to achieve multiple orientations for crystallographic analysis. Bright/dark field imaging and selected area electron diffraction patterns (SADP) were recorded in conventional TEM mode. A specially made selected area aperture 10 μm in diameter was used to obtain information from the smallest possible area. Generally, this enabled us to obtain diffraction patterns and images from a single grain (\sim 500 nm). Bright/dark field

analysis was used to verify the grains which were contributing to the diffraction pattern and to identify small precipitates. X-ray energy dispersive spectroscopy (XEDS) in the scanning transmission electron microscopy (STEM) mode was used to determine the approximate chemical composition of each grain characterized in the conventional imaging mode. A Tracor-Northern high angle x-ray detector model number 108-39 with TN-2000 and TN-5500 computers were used for x-ray microanalysis.¹⁴ The data were recorded for 500 seconds for each sample area. JEOL 100CX and JEOL 200CX TEMs are basically the same electron microscopes except for the accelerating voltage. The basic principles and the alignment procedures are identical to those discussed in detail in the Ph.D. dissertation by Hong Yang.¹⁵

3.5.2 Micro-microdiffraction

For the characterization of smaller grains ($\sim < 500$ nm), the TEM was operated in STEM mode and micro-microdiffraction ($\mu\mu$ D) patterns were recorded. Additional detailed information about $\mu\mu$ D is given in Appendix A. The high spatial resolution (2-3 nm) of STEM, plus the ability to perform $\mu\mu$ D and XEDS at the same time in areas about 20 nm in diameter allowed us to observe and document even the finer grain structures of these amalgams. XEDS data were used to confirm phase identifications made using $\mu\mu$ D by approximately matching the expected stoichiometric ratios from previous studies.^{6,7} The $\mu\mu$ D electron optics were calibrated at each use to minimize experimental error. Large Ag_3Sn (γ) single crystal grains in the same TEM amalgam specimens were used as the standard reference material for calibration. SAD and $\mu\mu$ D patterns were recorded

from the same Ag_3Sn (γ) crystal (Fig. 3.3). Interplanar spacings for Ag_3Sn (γ) were obtained from previously reported XRD data (PDF #4-0800).¹⁶ The $\mu\mu\text{D}$ system was calibrated against the SADP "standard." Fig. 3.4 shows an indexed $\mu\mu\text{D}$ pattern. When switching from conventional mode to $\mu\mu\text{D}$ mode, all of the magnetic lenses were returned to their original current settings using individual lens controls in the same operating sequence as used for the calibration procedure. This is necessary to minimize the effects of magnetic hysteresis. Using this methodology, the $\mu\mu\text{D}$ patterns are fully focused, and the $\mu\mu\text{D}$ and SAD camera lengths are known to within 1%.

3.5.3 Scanning Electron Microscopy

A JEOL T-300 SEM operating at 25 kV in backscattered electron imaging mode was used to observe the same areas analyzed by TEM. Since amalgams have a composite structure, it was not possible to simultaneously obtain electron transparent areas of all phases in the same region of the specimen in these experiments. For this reason, SEM was used to place the electron transparent areas within the context of the overall microstructure of the specimen, and to correlate the TEM data with the SEM results previously reported in the literature.¹⁷

3.5.4 Indexing of Diffraction Patterns

Interplanar spacings for each phase reported in the x-ray diffraction (XRD) literature^{18,19} were calculated from the known lattice parameters, since more reflections were found in our diffraction patterns than were observed by XRD. Sometimes, more

than one possible crystal structure was reported for an individual phase; our analyses considered all reported structures. BCC diffraction patterns were indexed and verified by matching them against standard spot patterns.²⁰ Hexagonal and orthorhombic patterns were indexed using the calculated interplanar spacings and the angles calculated between the corresponding crystal directions.

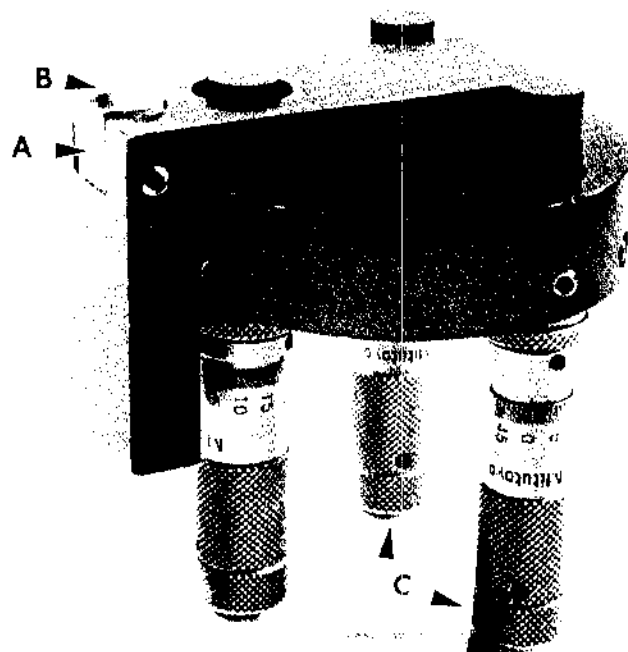


Figure. 3.1. The tripod polisher used for TEM specimen preparation. (A) glass insert, (B) sample, (C) rear micrometers.

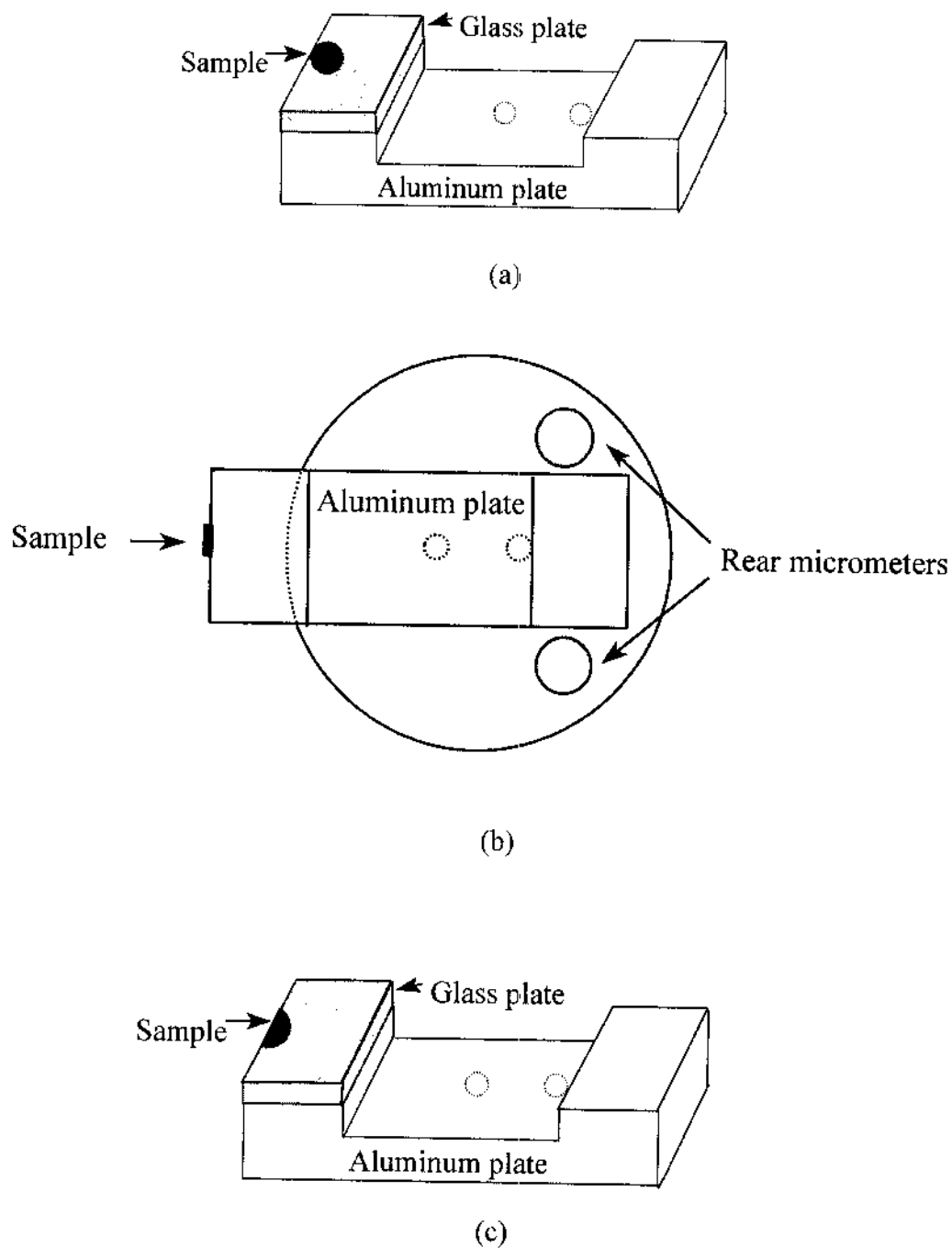
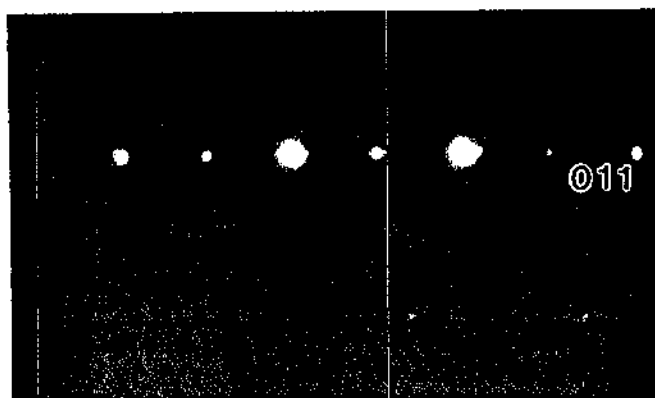
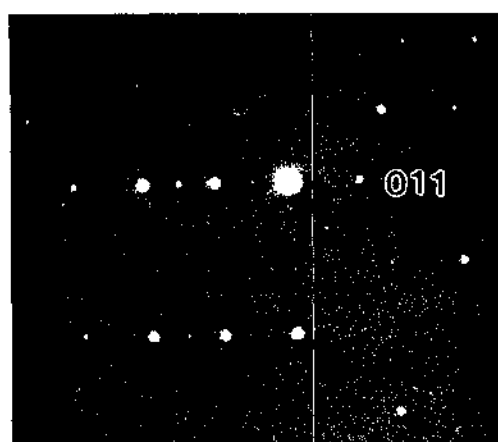


Figure. 3.2. (a) Sample mounted on aluminum plate for first side polishing; (b) bottom view of aluminum plate attached to tripod polisher with sample mounted on the side of plate for polishing the cut edge; (c) half moon sample mounted for reverse side polishing.

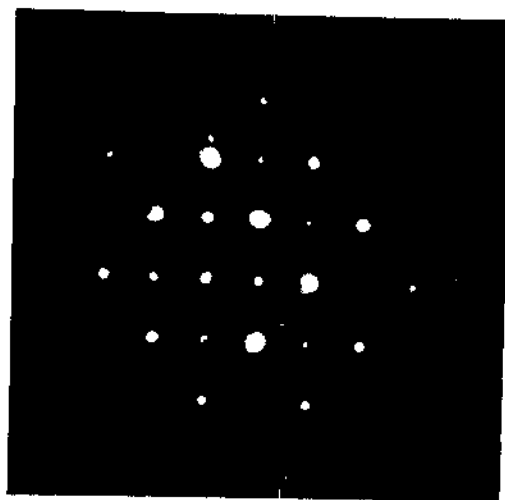


(a)

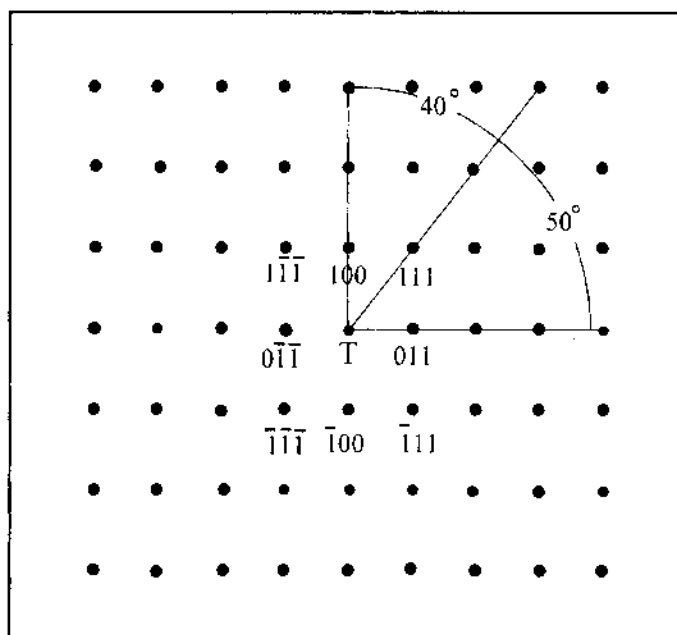


(b)

Figure. 3.3. (a) SADP from a Ag_3Sn (γ) grain. (b) Micro-microdiffraction pattern ($\mu\mu\text{D}$) from the same Ag_3Sn (γ) crystal.



(a)



(b)

Figure. 3.4. (a) Micro-microdiffraction pattern ($\mu\mu$ D) from Ag_3Sn (γ). (b) Indexed Ag_3Sn (γ) single crystal $\mu\mu$ D pattern.

CHAPTER 3 REFERENCES

1. R.M. Waterstrat and T Okabe, *Intermetallic Compounds* (John Wiley & Sons Ltd.), Vol. 2, p.580 (1994).
2. R.W. Phillips, *Skinner's Science of Dental Materials*, Eighth Edition (Saunders Co., West Washington Square, PA 19105), pp. 302-310 (1982).
3. S. S. White Dental Products International, Holmdel, NJ 07733.
4. J. F. DeFreitas, *Australian Dent. J.* **24**, 17 (1979).
5. Kerr Manufacturing Co., Romulus, MI 48174.
6. Addendum to American National Standards Institute/American Dental Association Specification No. 1 for Alloy Dental Amalgam, *JADA* **95**, 614 (1977).
7. C. L. Reynolds, Jr. and F. E. Wawner, Jr. , *Biomat., Med. Dev., Art. Org.* **2**, 67 (1974).
8. T. Okabe, F. Ling, and R. F. Hochman, *J. Dent. Res.* **54**, 162 (1975).
9. S. J. Klepeis, R. M. Anderson, and J. P. Benedict, *Mater. Res. Soc. Proc.* **115**, 179 (1988).
10. J. P. Benedict, R. M. Anderson, and S. J. Klepeis, *Mater. Res. Soc. Proc.* **254**, 121 (1991).
11. South Bay Technology, Inc., 1120 Via Callejon, San Clemente, California 92672.
12. Quick Bonding Nail Glue, Sally Hansen Div., Del Laboratories, Inc. Farmingdale, NY 11735.
13. Allied High Tech Products, Inc., 2376 East Pacifica Place, Rancho Dominguez, CA 90220.
14. Noran Instruments, 2551 W. Beltline Highway, Middleton, WI. 53562-2679.
15. H. Yang, Ph.D. Dissertation, University of North Texas, Denton, TX (1993).
16. International Center for Diffraction Data, 12 Campus Blvd., Newtown Square, PA 19073.

17. T. Okabe, R. J. Mitchell, M. B. Butts, and C. W. Fairhurst, *J. Dent Res.* **57**, 975 (1978).
 18. International Center for Diffraction Data (12 Campus Blvd., Newtown Square, PA 19073), Powder Diffraction File PDF#11-67, 4-0800, 27-618, 29-1151, 1-1240, 2-0713.
 19. G. Petzow and G. Effenberg, *Ternary Alloys - A Comprehensive Compendium of Evaluated Constitutional Data on Phase Diagrams*, (VCH Verlagsgesellschaft, Weinheim, Germany), pp. 256-261, 38-40, (1988).
 20. J. W. Edington, *Practical Electron Microscopy in Materials Science* (Van Nostrand Reinhold Co., 450 West 33rd Street, New York 10001), Appendix 4, pp. 303-312 (1976).
-

CHAPTER 4

MICROSTRUCTURE OF A LOW COPPER AMALGAM

Velvalloy

4.1 Introduction

Dental amalgam microstructure is the product of a number of solid-liquid and solid-solid interactions. In general, it is a composite structure consisting of a variety of intermetallic phases. The present-day low-Cu amalgam is characterized as an alloy containing less than 6% Cu, not much different than the one specified a century ago by Black. The microstructures of fully hardened low-Cu amalgams are largely understood^{1,2} through the use of optical and scanning electron microscopy (SEM), and x-ray diffractometry. However, until the present time, examination of fine microstructural details, such as the internal structures of phases, the grain boundary structures and the interfacial layers between phases, have been limited. These details often strongly affect the properties of materials, but can only be characterized using transmission electron microscopy (TEM). As the first step towards a more extensive investigation using TEM, this chapter presents the results of a study of a hardened low-Cu dental amalgam, Velvalloy, by analytical TEM.

The wedge mechanical polishing technique was used to prepare TEM samples, as described in Chapter 3. The samples were stored at room temperature in this

investigation. Since no other TEM microstructural study of a low-Cu amalgam, an overall picture of this composite microstructure was obtained to demonstrate the validity of the present results by verifying them against the previously reported SEM and XRD results^{1,2,3,4}

4.2 General Microstructure

Fig. 1 shows an SEM micrograph of a typical microstructure of Velvalloy amalgam and a segment of a prepared wedge specimen; the schematic diagram summarizes the phases found in our experiments. Velvalloy was found to consist of Ag_3Sn (γ) particles in a matrix primarily of Ag_2Hg_3 (γ_1) with a small amount ($\sim 10\%$) of HgSn_{7-9} (γ_2); these phases were identified in previous SEM³ and XRD⁴ studies. In addition, small amounts of Ag-Hg-Sn (β_1) and Cu_6Sn_5 (η'), not clearly identified in previous studies were observed. The crystal structures and lattice parameters for the phases confirmed by our analyses are summarized in Table 4.1, and a summary of the XEDS results is presented in Table 4.2. SAD, $\mu\mu\text{D}$ and XEDS analyses of numerous single crystals verified the identifications of these phases. The results of the TEM observations for each intermetallic phase observed in the hardened amalgam are discussed in separate sections for each phase. In addition, the microstructures of two reaction layers are presented: (1) between γ and γ_1 , as previously reported for high-Cu amalgam, and (2) between γ_1 and γ_2 , as reported in this work for the first time.

4.3 Alloy Particle Microstructure

4.3.1 Ag_3Sn (γ)

The Ag_3Sn (γ) alloy particles are dispersed throughout the Ag_2Hg_3 (γ_1) matrix (Fig. 1). SAD analyses of these particles verified the orthorhombic Ag_3Sn (γ) structure (Table 4.1). The single crystal patterns in Fig. 4.2 show the superlattice structure of Ag_3Sn (γ). The Ag_3Sn (γ) grains in the unreacted alloy particles are relatively large compared to the alloy particles (2-10 μm), suggesting that there are only a few grains per particle, consistent with slowly cooled ingots. XEDS analyses showed the approximate Ag_3Sn (γ) stoichiometry (Table 4.2). Smaller Ag_3Sn (γ) grains ($< 1 \mu\text{m}$) were also found in the Ag_2Hg_3 (γ_1)/ Ag_3Sn (γ) reaction layer (Section 4.5.1), and occasionally within large Ag_2Hg_3 (γ_1) crystals.

Fig. 4.3 shows a bright field TEM micrograph of part of a large unreacted Ag_3Sn (γ) particle and the SADP from the same grain. Imaging of the Ag_3Sn (γ) grains reveals numerous defects in the crystal structure, probably due to plastic deformation introduced during the lathe-cutting of the Ag-Sn-Cu alloy ingot during manufacture of the alloy powder. The curved streaks in the SADP may arise from two effects. First, the plastic deformation caused by the lathe-cutting resulted in the formation of cell walls and a mosaic type of microstructure. These small misorientations between the relatively defect-free areas are a form of preferred orientation, hence the streaking in the diffraction patterns. The range of misorientation is estimated to be approximately 8° . Second, dark field imaging suggests the presence of very fine precipitates within the Ag_3Sn (γ).

4.3.2 Cu_3Sn (ϵ)

In this examination of Velvalloy, we do not find any evidence of Cu_3Sn (ϵ) precipitates as reported for high-Cu amalgams,⁵ suggesting that Cu is mainly dissolved in the Ag_3Sn (γ) (the solubility of Cu is only a few wt%⁶). However, the streaks in the SADP may also be caused by very fine unobserved coherent precipitates which cause strain within the matrix. Elucidation of the details of the internal structure of the Ag_3Sn (γ) requires additional investigation.

4.4 Matrix Phases

4.4.1. Ag_2Hg_3 (γ_1)

TEM observations confirm that the predominant phase in the matrix of dental amalgam is Ag_2Hg_3 (γ_1) with a BCC crystal structure (Table 4.1). The γ_1 grains are polyhedral shaped, and the grain sizes range from 1-5 μm , as previously reported.⁷ The chemical composition of the Ag_2Hg_3 (γ_1) grains is uniform throughout the matrix regions (Table 4.2). Smaller grains ($< 0.5 \mu\text{m}$) were found in the discontinuous Ag_2Hg_3 (γ_1)/ Ag_3Sn (γ) reaction layer (Section 4.5.1).

Examination of the internal structure of Ag_2Hg_3 (γ_1) using bright field imaging does not show evidence of lattice defects such as twins, stacking faults, etc. (Fig. 4.4), unlike the previous TEM report on high-Cu amalgam. Single crystal diffraction patterns do not exhibit any extra spots (Fig. 4.5). The previous TEM study of Zn-containing and Zn-free high-Cu amalgams⁸ reported that the addition of Zn suppressed faulting in Ag_2Hg_3 (γ_1) grains. We cannot confirm this phenomenon for low-Cu amalgams because

we did not examine Zn-free Velvalloy amalgam. In addition, small Ag_3Sn (γ) grains are occasionally found embedded within the large Ag_2Hg_3 (γ_1) grains in the matrix, which were not found in previous SEM experiments (Fig. 4.6). The formation of these small grains is discussed in conjunction with the γ/γ_1 reaction layer in Section 4.5.1. Unlike high-Cu amalgams, Cu_6Sn_5 (η') precipitates are not observed in the Ag_2Hg_3 (γ_1) matrix. Cu_6Sn_5 (η') was not expected due to the low-Cu concentration in this amalgam.

The grain boundaries between the Ag_2Hg_3 (γ_1) grains are usually smooth, which is typical of polyhedral grain structures, and contain no additional phases (Fig. 4.4). On the other hand, the Ag_2Hg_3 (γ_1)/ Ag_3Sn (γ) grain boundaries are irregularly shaped (Fig. 4.7), which is typical of reaction interfaces, and a discontinuous reaction layer was present through these boundaries (Section 4.5.1). The Ag_2Hg_3 (γ_1)/ $\text{HgSn}_{7.9}$ (γ_2) grain boundaries were smooth, but were also separated by continuous reaction layers (Section 4.5.2).

The same areas of the TEM specimen were re-examined after aging at room temperature for 140 days. There were no noticeable changes in the size, shape or chemical composition of the Ag_2Hg_3 (γ_1) grains. This demonstrates the stability of the matrix phase at room temperature. In our specimens, only relatively poorly electron transparent γ_1 sections were found, although these regions were thin enough for SAD and μED analyses. The Ag_2Hg_3 (γ_1) sections may appear thick due to electron scattering by the heavy Hg atoms compared to Ag, Sn and Cu atoms. However, thinner, more electron transparent Hg-containing regions were prepared using diamond lapping films (Chapter 3). These regions were fine-grained Ag-Hg-Sn (β_1) as shown in Fig. 4.8(a), and after 24 hrs storage, these regions changed to include transparent films and dark Hg containing

regions (Fig. 4.8(b)). From our SEM observations we concluded that they were artifacts of the modified specimen preparation technique, and actually should have been Ag_2Hg_3 (γ_1). This apparent transformation from γ_1 to β_1 is thought to be due to Hg diffusion/evaporation out of sections too thin to form a protective oxide film. Hg diffusion through and evaporation from polished bulk specimens of amalgams are well known phenomena. The formation of surface oxide films on Ag_2Hg_3 (γ_1) by the diffusion of Sn and Zn have been shown to retard Hg evaporation.⁹ In fact, these small grains decomposed both under the electron beam and during 24 hour storage at room temperature, indicating that a protective oxide film did not form. Our results suggest that the section thickness of Ag_2Hg_3 (γ_1) affects oxide film formation, but even a thin section of Ag_2Hg_3 (γ_1) may become chemically stable at room temperature.

4.4.2 $\text{HgSn}_{7.9}$ (γ_2)

The second most prominent matrix phase in low-Cu amalgams, $\text{HgSn}_{7.9}$ (γ_2), has a hexagonal crystal structure (Table 4.1). The $\text{HgSn}_{7.9}$ (γ_2) phase is usually found in irregular and elongated shaped regions (approx. $2\text{ }\mu\text{m} \times 6\text{ }\mu\text{m}$) composed of several equiaxed grains. The $\text{HgSn}_{7.9}$ (γ_2) morphology can be explained by the reaction sequence which occurs during solidification of the amalgam (Chapter 2). XEDS analyses confirmed the approximate $\text{HgSn}_{7.9}$ (γ_2) stoichiometry (Table 4.2). Most of the $\text{HgSn}_{7.9}$ (γ_2) grains are embedded in the Ag_2Hg_3 (γ_1) matrix. Sometimes a few small Ag_3Sn (γ) crystals, and rarely Ag-Hg (β_1) crystals, were observed adjacent to the $\text{HgSn}_{7.9}$ (γ_2) (Fig. 4.9).

The microstructure of $\text{HgSn}_{7.9}$ (γ_2) and an SADP from one of the crystals are shown in Fig. 4.10. Note that this specimen was observed after aging the amalgam for sixty days. A characteristic feature of the $\text{HgSn}_{7.9}$ (γ_2) phase is the presence of defects in the crystal lattice accompanied by streaking in the diffraction pattern superimposed on the main diffraction spots. This suggests that the streaks are due to elastic distortion of the γ_2 grains arising from coherent precipitates which produce diffuse scattering in the direction of the distortion. However, a more detailed microstructural study of $\text{HgSn}_{7.9}$ (γ_2) is still required.

Further analyses of the SADP showed diffraction rings identified as ZnO (Fig. 11). The ZnO rings were most noticeable in the $\text{HgSn}_{7.9}$ (γ_2) phase compared to the other phases. The amount of oxide on the $\text{HgSn}_{7.9}$ (γ_2) phase was found to increase after room temperature aging of the specimen. This suggests a diffusion based reaction mechanism for the oxide formation, although whether the ZnO forms as a surface film or as internal precipitates is unclear from our experiments. The solubility of Zn in Ag_3Sn (γ), Ag_2Hg_3 (γ_1), and $\text{HgSn}_{7.9}$ (γ_2) is 0.1-1.3, 0.2-0.4, and 0-0.1 wt% respectively,¹⁰ i.e., Zn is the least soluble in $\text{HgSn}_{7.9}$ (γ_2). Thus, Zn probably diffuses to the $\text{HgSn}_{7.9}$ (γ_2) surface and forms ZnO.

The boundaries between the $\text{HgSn}_{7.9}$ (γ_2) grains are smooth and free of grain boundary precipitates (Fig. 10). In contrast, the $\text{HgSn}_{7.9}$ (γ_2)/ Ag_2Hg_3 (γ_1) grain boundaries are actually a continuous reaction layer as discussed in Section 4.5.2.

4.4.3. Ag-Hg-Sn (β_1)

The Ag-Hg-Sn (β_1) was verified to have a hexagonal crystal structure (Table 4.1). This phase was found to exist in two distinct compositions: the binary Ag-Hg phase and the ternary Ag-Hg-Sn phase (Tables 4.1 and 4.2). These phases were identified by $\mu\mu$ D and XEDS, but could not be distinguished by electron diffraction alone because of the small differences in the interplanar crystal spacings. As discussed in the Chapter 2, SEM has difficulty in identifying small grains of β_1 , and XRD has trouble detecting small volume fractions of this phase. In this examination, even the smallest grains in the microstructure could be characterized by XEDS and $\mu\mu$ D, so small β_1 grains were positively identified for the first time.

The binary Ag-Hg (β_1) phase is found randomly dispersed within the Ag_2Hg_3 (γ_1) as 0.5 to 1 μm grains (Table 4.2). The structure of these grains is similar to Ag_2Hg_3 (γ_1), which indicates their formation through a dissolution/precipitation mechanism. The ternary Ag-Hg-Sn (β_1) phase was found in the Ag_3Sn (γ)/ Ag_2Hg_3 (γ_1) reaction layer (Section 4.5.1) as smaller grains (<0.5 μm). While XEDS analyses showed that the binary phase has a consistent composition, the ternary phase has a range of compositions (Table 4.2). A continuous solid solution of Ag-Sn (β) and Ag-Hg (β_1) is expected based on the ternary phase diagram¹¹ as discussed in Chapter 2. The ternary β_1 has crystallographic defects similar to those found in the alloy particles. As explained in Chapter 2, dislocations and grain boundaries in the particles are enhanced diffusion paths for Hg. Ternary β_1 is a product of diffusion of Hg into the particles.

4.4.4. Cu_6Sn_5 (η')

Only a few Cu_6Sn_5 (η') precipitates were observed in our TEM specimens. However, the amount of Cu in Velvalloy is relatively small, so the probability of locating Cu_6Sn_5 (η') is also small. In our specimens, the grain size ranges from 0.1 to 0.5 μm with equiaxed shapes. Some Cu_6Sn_5 (η') grains are observed in the reaction layer between γ and γ_1 (Fig. 4.15), while other Cu_6Sn_5 (η') grains are found as small clusters in the Ag_2Hg_3 (γ_1) matrix (Fig. 4.12). There are two known forms of Cu_6Sn_5 : above 227°C , the η phase is a disordered solid solution, while at lower temperature the η' phase has a superlattice structure. In this research, no attempt was made to distinguish between η and η' . However, superlattice reflections were obtained in a few single crystal patterns as shown in Fig. 4.13. Extra diffraction spots observed in the SADPs of large unreacted Ag_3Sn (γ) alloy particles also suggest the presence of small Cu_6Sn_5 (η') precipitates (Fig. 4.14). Jensen and Anderson have reported the formation of Cu_6Sn_5 (η') in some low-Cu amalgams.¹² However, there is no evidence of rod-shaped Cu_6Sn_5 (η') precipitates in the matrix as reported by Boswell for high-Cu amalgams.⁸

4.5. Reaction Layers

4.5.1. γ/γ_1 reaction layer

Our TEM investigation shows that a discontinuous reaction layer exists around the large Ag_3Sn (γ) particles, which separates these particles from the Ag_2Hg_3 (γ_1) matrix. Of the Ag_3Sn (γ) particles observed, more than half of the particle surfaces were covered by this reaction layer, although it was usually less than 0.5 μm thick. This thin layer was

not found in previous SEM examinations, perhaps explaining why no previous TEM reports have been published on low-Cu amalgam reaction layers.

The reaction layer has a relatively fine grain structure (between 0.1 μm and 0.5 μm). A schematic diagram is shown in Fig. 4.15(a) and a bright field image of a part of the reaction layer illustrating all the identified phases is shown in Fig. 4.15(b). XEDS and μED show that these grains were primarily a mixture of Ag_3Sn (γ) and a ternary Ag-Hg-Sn (β_1) phase, although Cu_6Sn_5 (η') grains were occasionally found. As found in high-Cu amalgam γ/γ_1 reaction layers, an inner and an outer reaction layer are observed. The inner layer consists primarily of fine grains of Ag_3Sn (γ) and Ag-Hg-Sn (β_1), while the outer layer contains fine grains of Ag_2Hg_3 (γ_1) and occasionally Cu_6Sn_5 (η').

The XEDS analyses of the ternary Ag-Hg-Sn (β_1) phase (Table 4.2) showed that its composition varied from grain to grain. The Ag-Hg-Sn ternary phase diagram¹¹ (Fig. 2.5) shows a hexagonal Ag-Hg-Sn (β_1) phase field (Table 4.1) which is a solid solution of the Ag-Sn (β) and Ag-Hg (β_1) binary phases; the composition ranges for the ternary phase are not well defined. Okabe et al.¹³ demonstrated that a ternary Ag-Hg-Sn (β_1) phase forms at the interface when γ/γ_1 diffusion couples are heated above 60°C for up to 3 months, with a composition of 38-49 wt% Ag, 41-58 wt% Hg, and 4-13 wt% Sn. Our XEDS data for the β_1 phase are qualitatively close to this reported composition range. However, the present results show that only a very thin reaction layer forms in fresh low-Cu amalgam at room temperature. The discontinuous nature of the reaction layer suggests that the β_1 phase is thermodynamically less stable than the Ag_3Sn (γ) and Ag_2Hg_3 (γ_1) phases at room temperature.

The shape of the Ag_3Sn (γ)/ Ag_2Hg_3 (γ_1) interface, Fig. 4.7, showed that some regions of the Ag_3Sn (γ) particles had been chemically attacked more than other regions during the reaction. Close inspection of the interface revealed that in many of these heavily attacked regions, the Ag-Hg-Sn (β_1) phase was observed, even when no reaction layer was present. The boundaries between the Ag_3Sn (γ) and Ag-Hg-Sn (β_1) phases are generally not well defined, suggesting a diffusion reaction mechanism. The observation of small Ag_3Sn (γ) grains within the Ag_2Hg_3 (γ_1) grains and at the γ/γ_1 reaction layer interface (Figs. 4.6, 4.7), which probably formed during the early stages of the amalgamation reaction, implies a non-uniform chemical attack of the Ag_3Sn (γ) phase by Hg.

The presence of Cu_6Sn_5 (η') in the low-Cu amalgam reaction layer is consistent with high-Cu amalgam reaction layers as earlier identified by Mahler.¹⁴ As discussed in Chapter 2, Cu has the lowest solubility in Hg for the Ag, Sn, and Cu from the alloy particles. In fact, the Cu solubility is 35 times lower than that of Ag in Hg, and 88 times lower than that of Sn in Hg. Hence, even for small Cu concentrations as found in low-Cu amalgams, Cu_6Sn_5 (η') should precipitate first and be located near the original alloy particle boundaries. Our results show that Cu_6Sn_5 (η') is the stable Cu-Sn phase and that it precipitates from Sn-rich, Cu-containing Hg liquids, even for low-Cu concentrations. The discontinuous nature of the reaction layer suggests that the Cu is not homogeneously distributed in the initial Ag-Sn-Cu alloy particles.

4.5.2. γ_2/γ_1 reaction layer

A continuous reaction layer was found to exist between the Ag_2Hg_3 (γ_1) and $\text{HgSn}_{7.9}$ (γ_2) phases. It is approximately 0.1 μm thick (Figs. 4.9, 4.10). This reaction layer is much more electron transparent than the surrounding phases. Using $\mu\mu\text{D}$, we found that electron beam easily damaged this layer, making it difficult to obtain a diffraction pattern. However, XEDS did yield indications of Zn. Lacking additional information, conclusions on the microstructure of this layer cannot be made.

4.6. Location of Zn

The present examination found that the $\text{HgSn}_{7.9}$ (γ_2) phase has a more obvious layer of ZnO than any other phase. This can be explained by the lower solubility of Zn in $\text{HgSn}_{7.9}$ (γ_2) compared to Ag_2Hg_3 (γ_1).¹⁵ The effect of Zn on the microstructure of amalgams is not completely understood, although it apparently improves compressive strength, fatigue, and creep resistance.^{16,17} The Zn concentration in Velvalloy is very small. Therefore, it is difficult to detect its location within the microstructure. However, Zn is the primary element in the oxide on the surface of the specimen. X-ray photoelectron spectroscopy (XPS or ESCA) of surface films formed on Zn-containing amalgams showed that the surface films were primarily composed of a mixed oxide-hydroxide compound which may contain a hydrate of Sn and Zn.⁹ Additional studies of amalgams with larger Zn concentrations are required to more fully understand the effects of Zn on amalgam microstructure. These results are consistent with the γ_2/γ_1 reaction layer being a form of Zn oxide, although this identification must remain speculative.

4.7. Summary and Conclusions

TEM specimens of Velvalloy low-Cu dental amalgams were prepared using the "wedge technique." Our experiments demonstrated that the microstructure of this amalgam was not damaged during fabrication of the samples. Subsequent TEM examination and microanalysis found that the microstructure consists mainly of a Ag_2Hg_3 (γ_1) and $\text{HgSn}_{7.9}$ (γ_2) matrix surrounding Ag_3Sn (γ) particles, consistent with previous SEM^{1,2,3} and XRD studies.⁴ In addition, minor amounts of Ag-Hg-Sn (β_1), Ag-Hg (β_1), and Cu_6Sn_5 (η'), that were not clearly identified in previous studies, are also observed. SAD, $\mu\mu\text{D}$, and XEDS analyses of numerous single crystals verified the identification of these phases.

The Ag_2Hg_3 (γ_1) matrix is made up of equiaxed grains 1-5 μm in size with few lattice defects and smooth, precipitate free γ_1/γ_1 grain boundaries. The smooth nature of the γ_1/γ_1 grain boundaries explains the low creep resistance of low-Cu amalgam, i.e., there is no resistance to grain boundary sliding.

Unreacted alloy particles are composed primarily of Ag_3Sn (γ) grains (2-10 μm). The Ag_3Sn (γ) phase has a high density of lattice defects. No separate Cu_3Sn (ϵ) is found in the alloy particles, consistent with previous findings.²

For the first time, the Ag-Hg-Sn (β_1) and Ag-Hg (β_1) phases are identified in freshly amalgamated samples stored at room temperature. The β_1 found in the reaction layer between Ag_3Sn (γ)/ Ag_2Hg_3 (γ_1) is primarily a ternary Ag-Hg-Sn (β_1) phase, as suggested by the ternary phase diagram. Binary Ag-Hg (β_1) is occasionally found in the matrix with a morphology similar to that of Ag_2Hg_3 (γ_1).

There is a discontinuous reaction layer formed around unreacted alloy particles. TEM study around numerous unreacted particles revealed the fine structure of this ill-defined layer. In general, the reaction layer between Ag_3Sn (γ) and the Ag_2Hg_3 (γ_1) matrix is composed of two layers. The inner layer, which is next to the particle, contains fine grains of Ag_3Sn (γ) and Ag-Hg-Sn (β_1), and the outer layer is primarily composed of smaller Ag_2Hg_3 (γ_1) compared to matrix grains. Occasionally, Cu_6Sn_5 (η') is also found in the outer layer.

Irregularly shaped $\text{HgSn}_{7.9}$ (γ_2) regions are dispersed in the Ag_2Hg_3 (γ_1) matrix. Polycrystalline regions of $\text{HgSn}_{7.9}$ (γ_2) are mainly surrounded by Ag_2Hg_3 (γ_1) grains. A few Ag_3Sn (γ) crystals are also found on the outer periphery of $\text{HgSn}_{7.9}$ (γ_2). A more electron transparent layer exists surrounding $\text{HgSn}_{7.9}$ (γ_2), which separates $\text{HgSn}_{7.9}$ (γ_2) and Ag_2Hg_3 (γ_1). SADPs from $\text{HgSn}_{7.9}$ (γ_2) show extra diffraction rings due to ZnO . Since Zn has the lowest solubility in $\text{HgSn}_{7.9}$ (γ_2) compared to other amalgam phases, it probably precipitates as ZnO or diffuses out to form ZnO .

Electron transparent regions of TEM samples are unchanged after 140 days at room temperature. This demonstrates the stability of Ag_2Hg_3 (γ_1) in the amalgam microstructure at room temperature.

Table 4.1. Lattice parameters of the phases in Velvalloy.

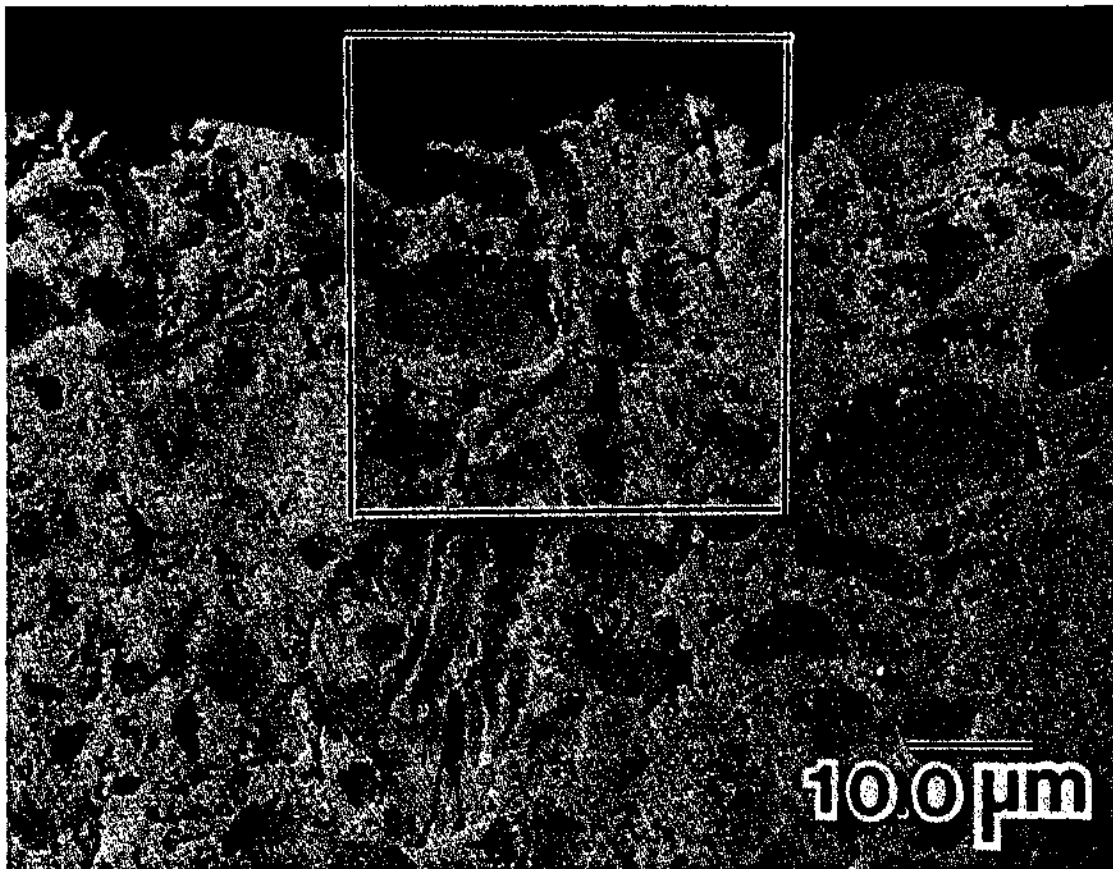
Phase	Crystal structure	Lattice parameters (Å)
$\text{Ag}_2\text{Hg}_3 (\gamma_1)$	BCC	$a = 10.04$
$\text{Ag}_3\text{Sn} (\gamma)$	orthorhombic superlattice	$a = 2.99 ; b = 5.15 ; c = 4.78$ $a = 5.97 ; b = 4.78 ; c = 5.18$
$\text{HgSn}_{7.9} (\gamma_2)$	hexagonal	$a = 3.21 ; c = 2.99$
Ag-Hg-Sn (β_1) is a solid solution of: Ag + 46 at. % Hg (β_1) Ag + 15 at. % Sn (β)	hexagonal hexagonal	$a = 2.99 ; c = 4.84$ $a = 2.93 ; c = 4.78$
$\text{Cu}_6\text{Sn}_5 (\eta')^a$	hexagonal superlattice	$a = 4.19 ; c = 5.086$ $a = 20.95 ; c = 25.43$

^a η' is the superlattice structure, NiAs (B8₂) type.

Table 4.2. Ratio of areas of prominent x-ray peaks. ZAF corrections were not performed.

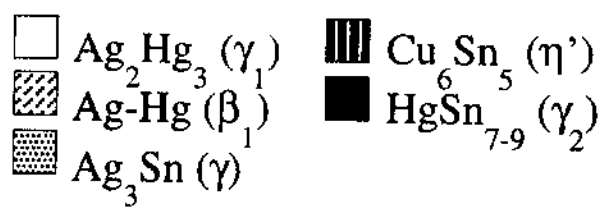
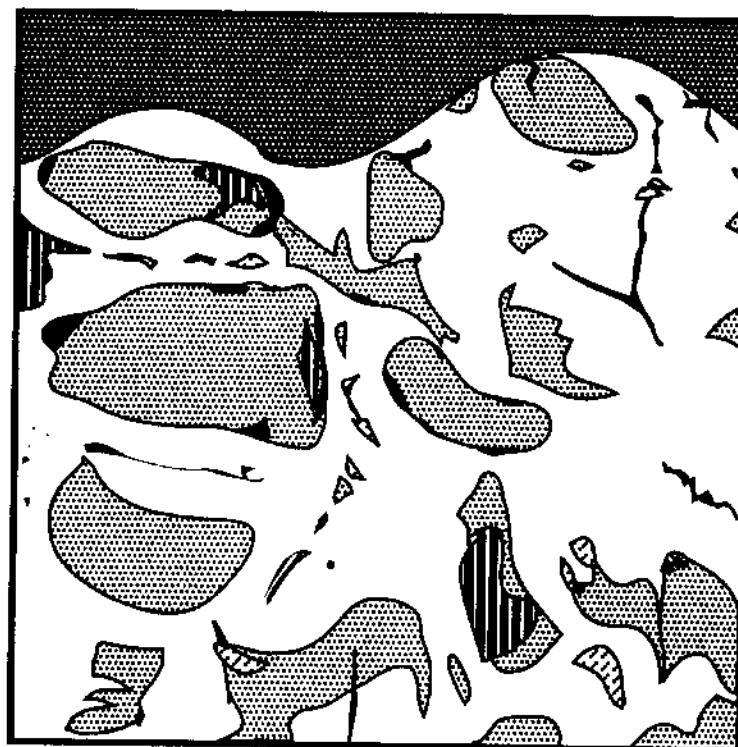
Phase	Elements	Ratio of area of peaks $L\alpha/L\alpha$
Ag_2Hg_3 (γ_1)	Hg, Ag	1.49
Ag_3Sn (γ)	Ag, Sn	2.97
$\text{HgSn}_{7.9}$ (γ_2)	Sn, Hg	7.43
HgAg (β_1)	Hg, Ag	0.64
Ag-Hg-Sn (β_1) reaction layer	Hg, Ag; Ag, Sn	0.7, 5.34
Cu_6Sn_5 (η')	Cu, Sn	1.72 ^b

^b For Cu_6Sn_5 (η'), the $K\alpha/L\alpha$ ratio was used.

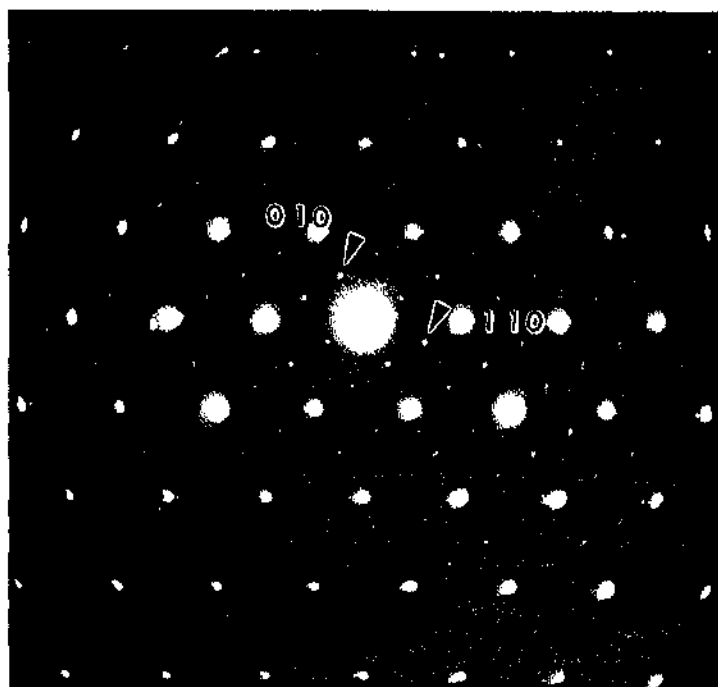


(a)

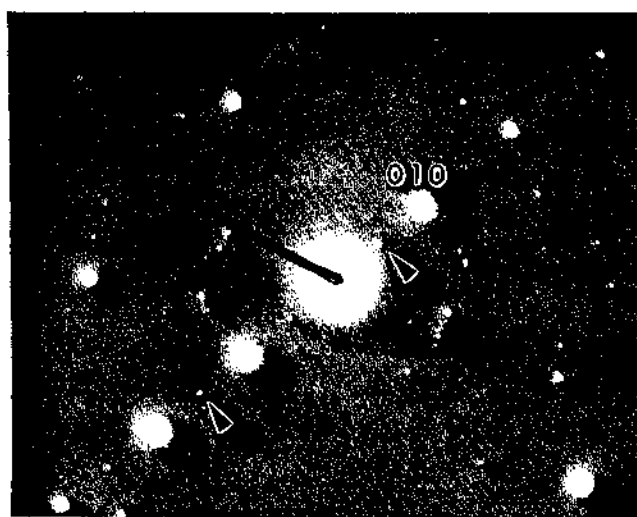
Figure. 4.1. (a) SEM image of TEM specimen showing the straight edge achieved by mechanical polishing. (b) Schematic diagram of the general microstructure of Velvalloy.



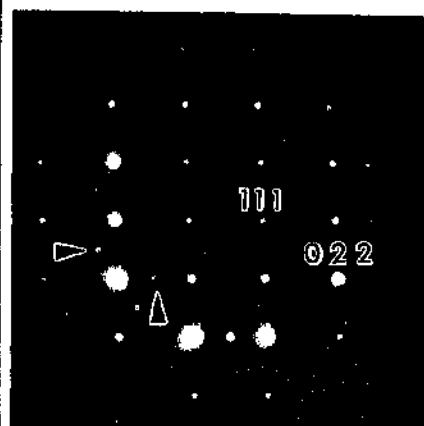
(b)



(a)

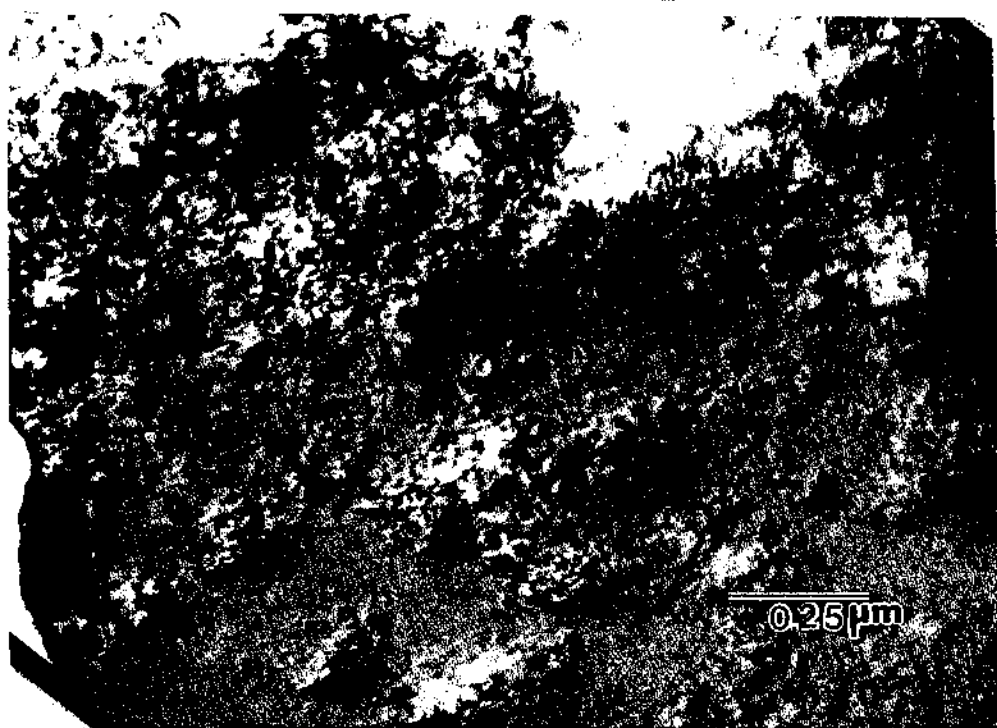


(b)

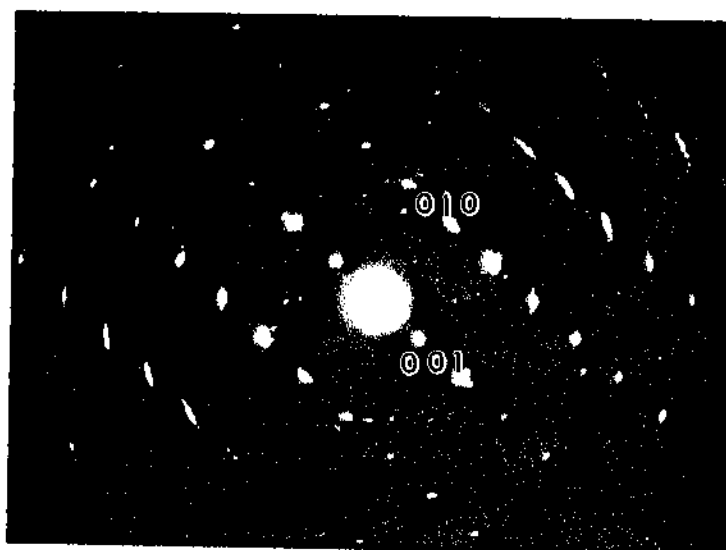


(c)

Figure 4.2. Single crystal patterns from three different Ag_3Sn (γ) grains showing superlattice reflections. (a) $[0\ 0\ 1]\gamma$, (b) $[2\ 0\ \bar{1}]\gamma$, (c) $[0\ \bar{1}\ 1]\gamma$.



(a)



(b)

Figure 4.3. (a) Bright field image of part of a large unreacted Ag_3Sn (γ) particle. (b) SADP from the same crystal showing streaking in the pattern. $[1\ 0\ 0]\gamma$.

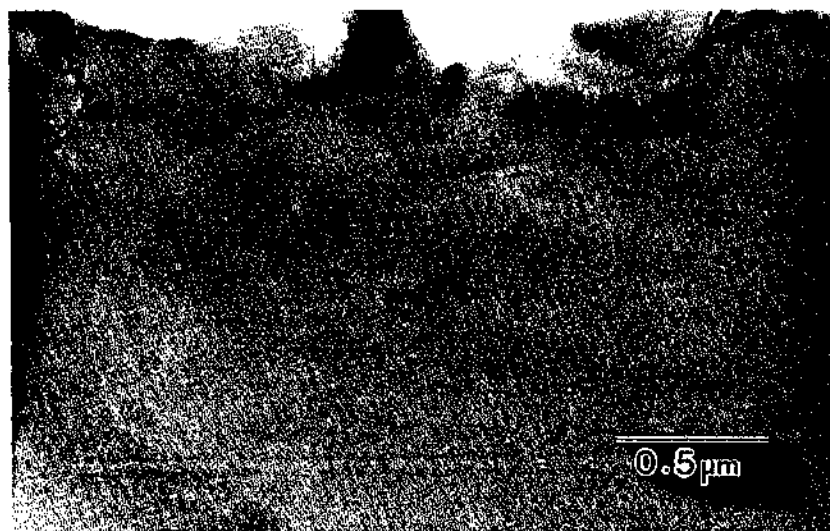


Figure 4.4. Micrograph of matrix illustrating smooth grain boundaries of Ag_2Hg_3 (γ_1).

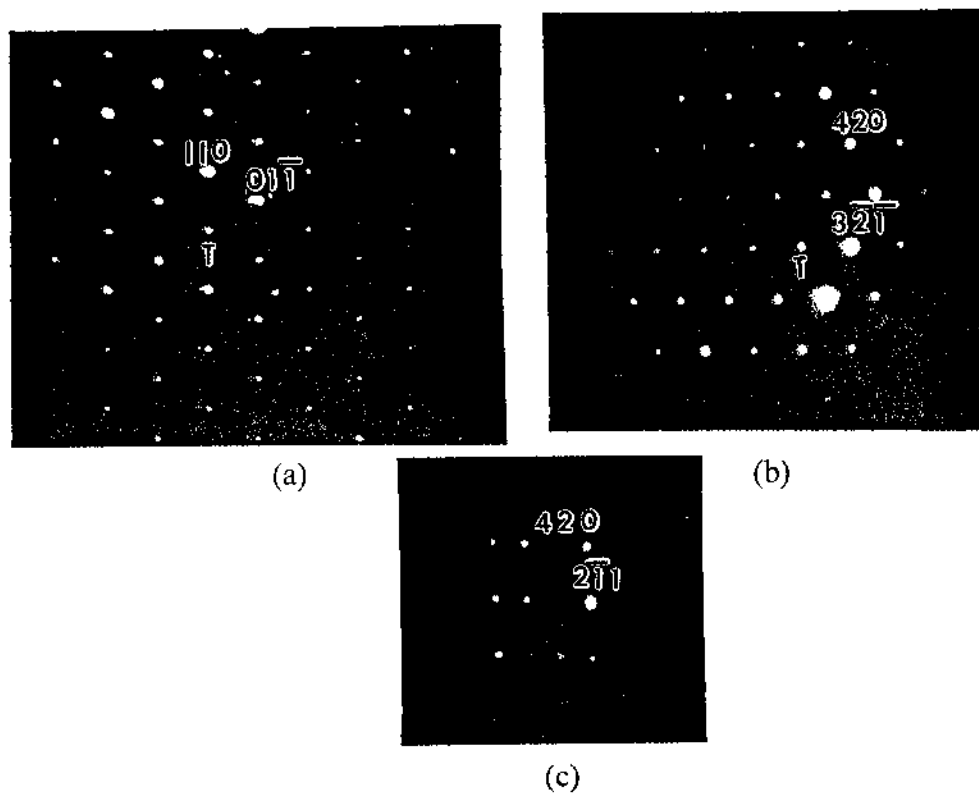


Figure 4.5. Diffraction patterns from Ag_2Hg_3 (γ_1) (a) SADP $[\bar{1} \ 1 \ 1]_{\gamma_1}$, (b) $\mu\mu\text{D}$ $[1 \ \bar{2} \ 7]_{\gamma_1}$, and (c) $\mu\mu\text{D}$ $[\bar{5} \ 1 \ 9]_{\gamma_1}$.

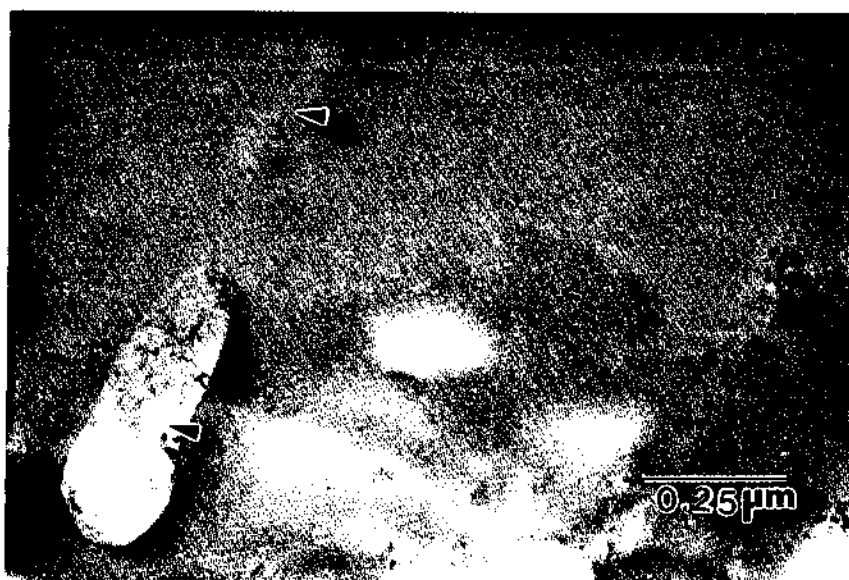
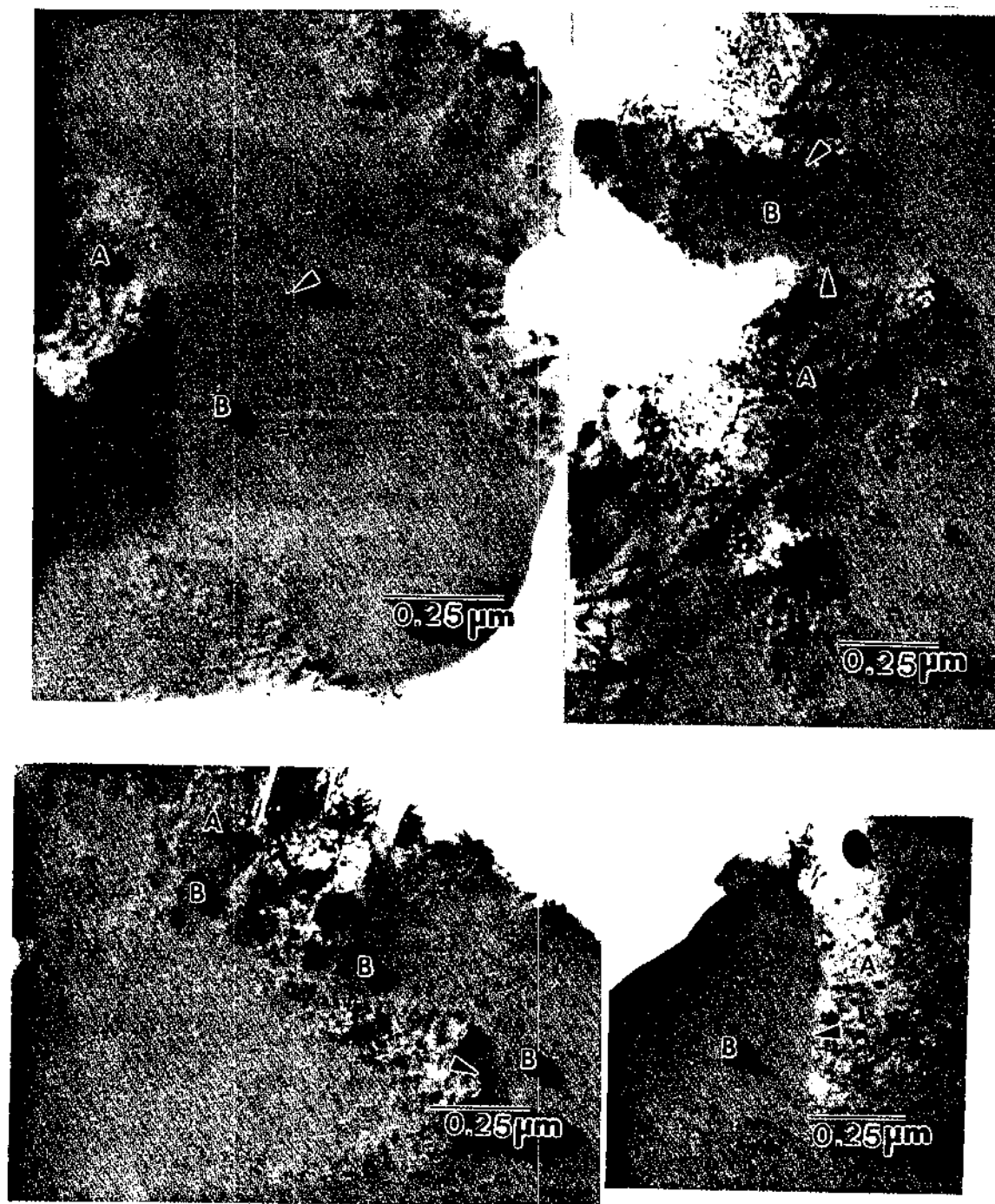


Figure 4.6. TEM micrograph of Ag_2Hg_3 (γ_1) grain showing small Ag_3Sn (γ) grains inside it.

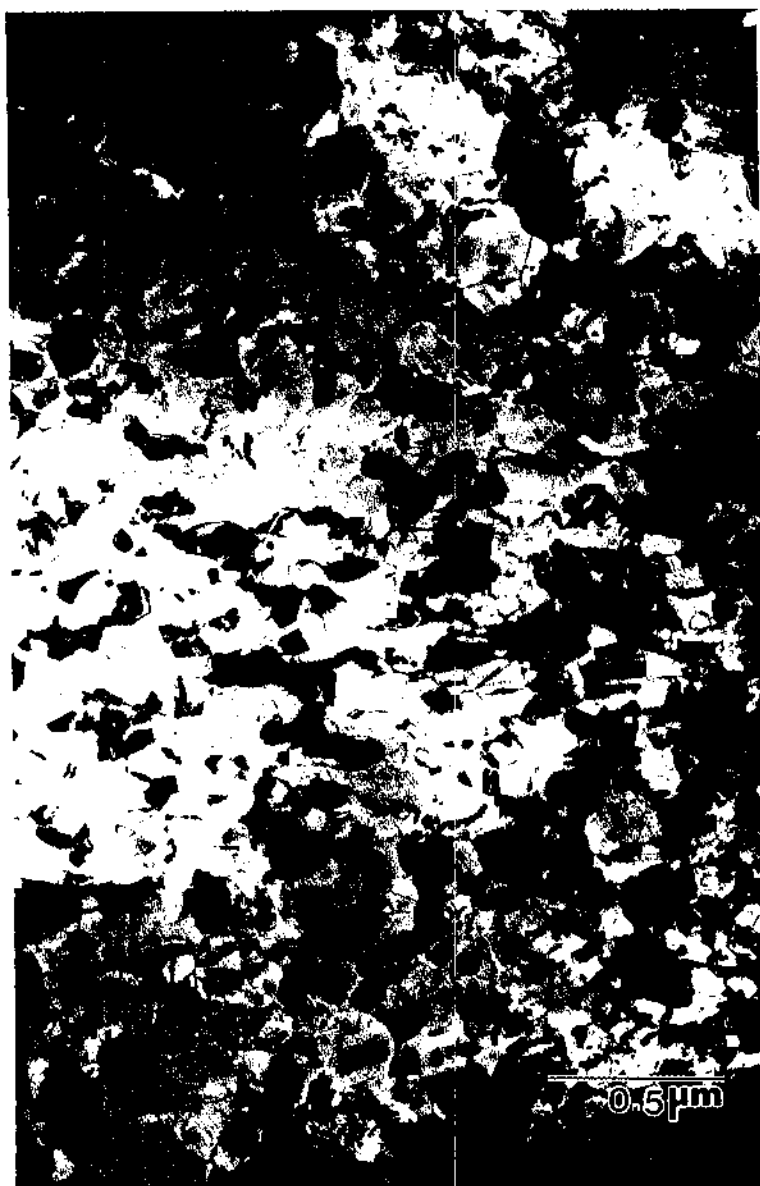


(a)

Figure 4.7. (a) Irregular grain boundaries between Ag_3Sn (γ) and Ag_2Hg_3 (γ_1), (b) Hg reacting with large Ag_3Sn (γ) particle. (A) Ag_3Sn (γ), (B) Ag_2Hg_3 (γ_1).



(b)



(a)

Figure 4.8. (a) Bright field image of thin regions prepared with lapping film showing equiaxed Ag-Hg-Sn (β_1) crystals. (b) After 24 hrs storage, the microstructure was changed to include transparent films and dark mercury containing regions.



(b)

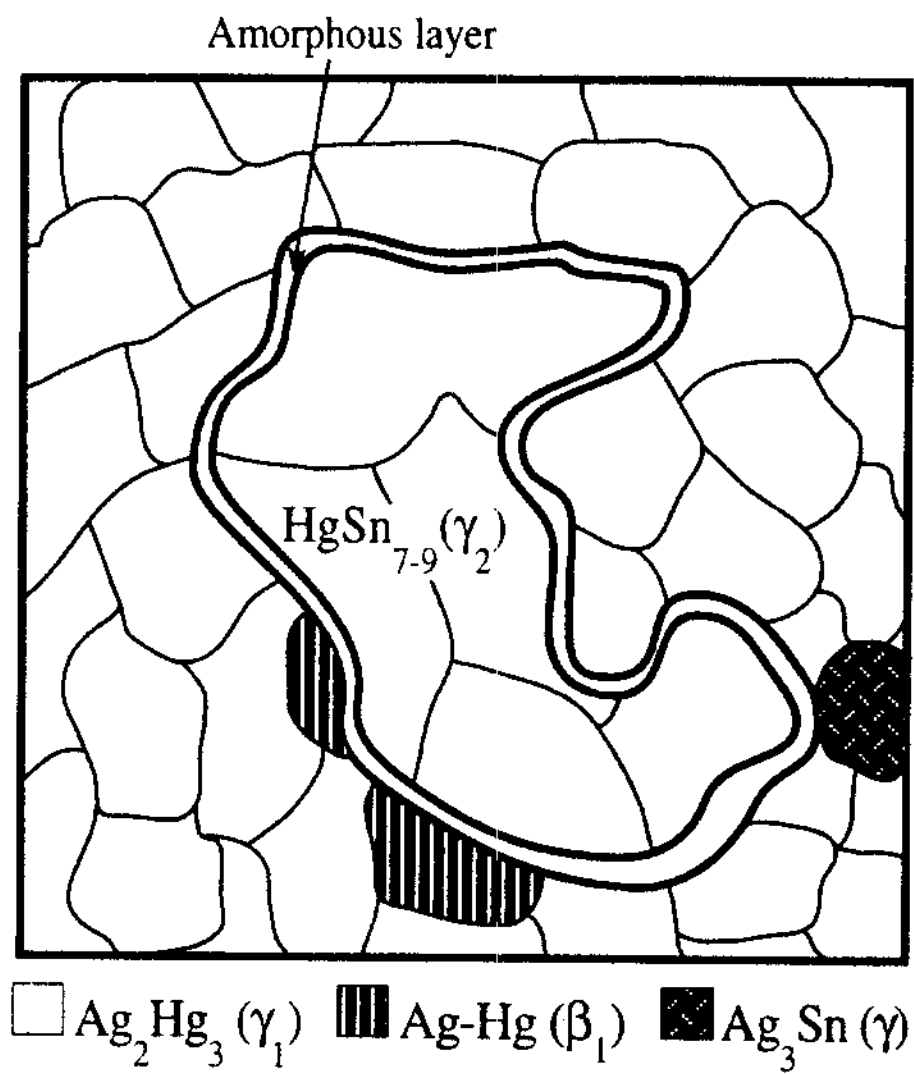
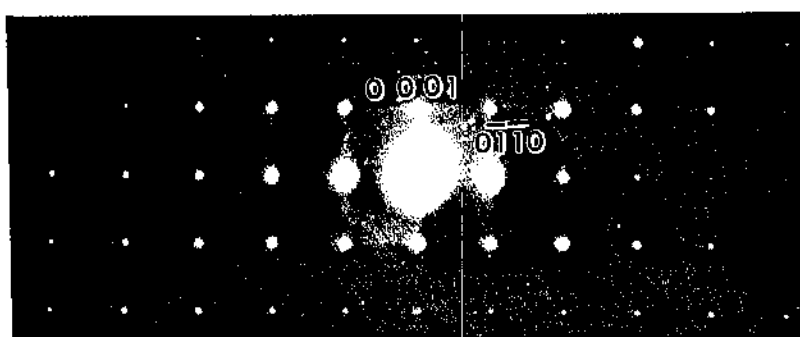


Figure 4.9. A sketch of the reaction layer between γ_2 and γ_1 .



(a)



(b)

Figure 4.10. TEM micrograph of $\text{HgSn}_{7.9}$ (γ_2) showing an amorphous layer between γ_2 and Ag_2Hg_3 (γ_1). Arrows indicate the amorphous layer. (b) Single crystal pattern of γ_2 illustrating streaks. $[2\bar{1}\bar{1}0]$.

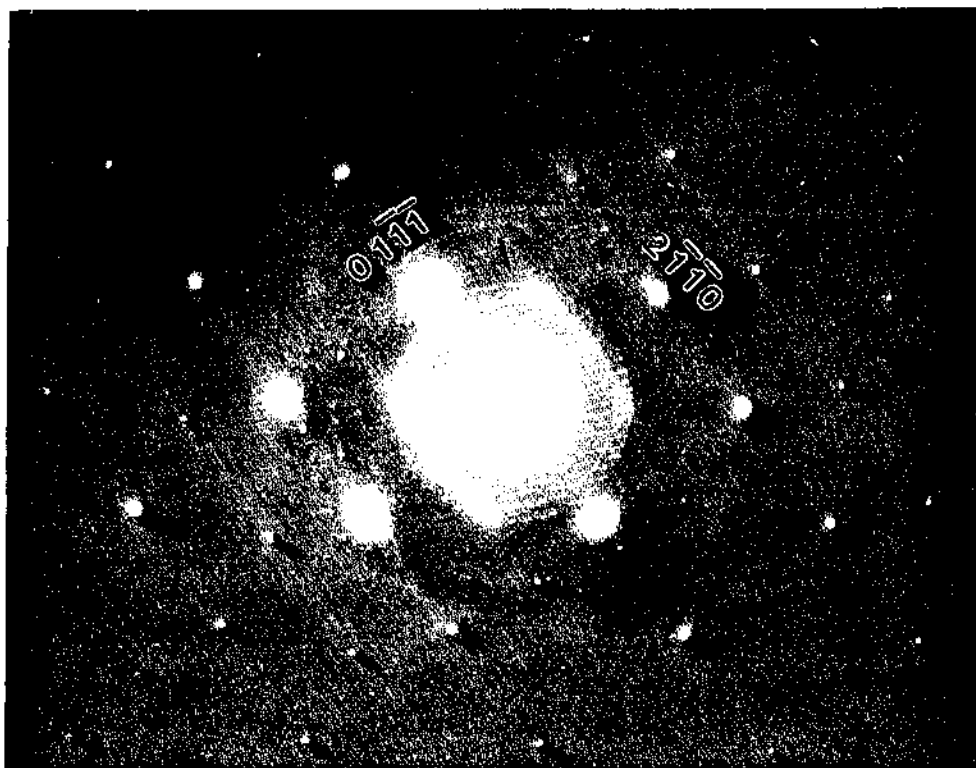
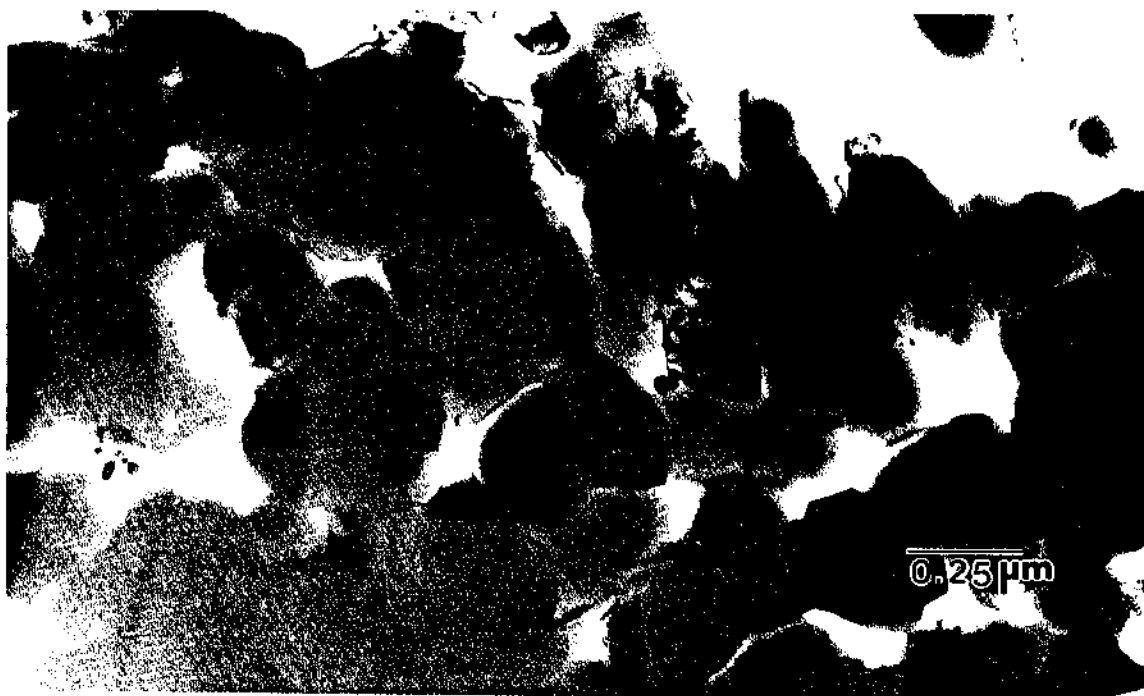
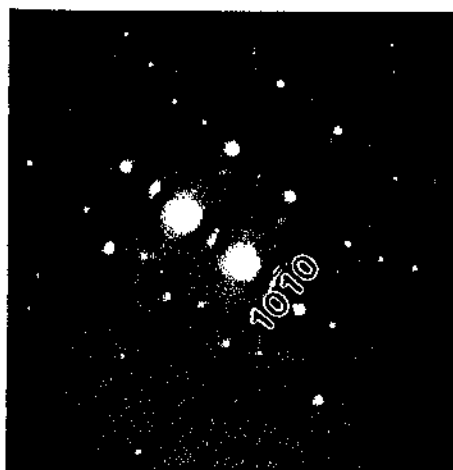


Figure 4.11. Single crystal pattern of γ_2 illustrating streaks and ZnO diffraction rings.

$[0\ 1\ \bar{1}\ 2]$.



(a)



(b)

Figure 4.12. (a) Bright-field TEM image of a small cluster of Cu_6Sn_5 (η') equiaxed grains found in the matrix. (b) $\mu\mu\text{D}$ pattern.



Figure 4.13. (a) SADP from a Cu_6Sn_5 (η') grain showing superlattice spots. $[7 \bar{2} \bar{5} 3]$.

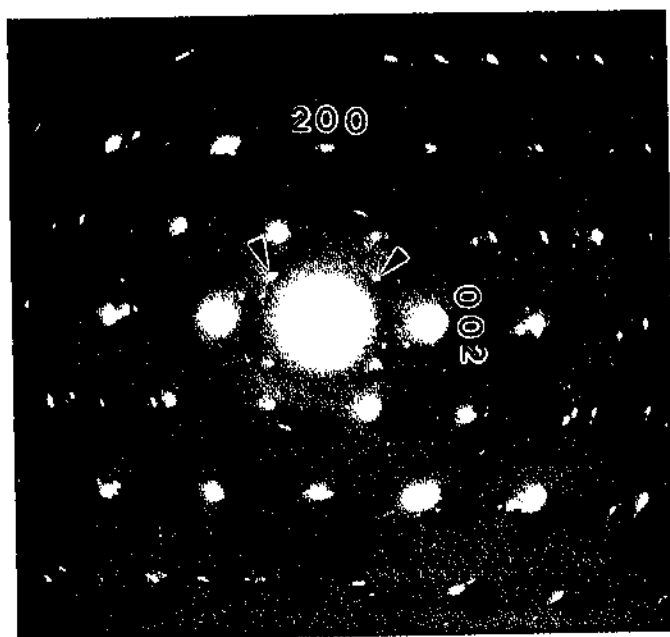


Figure 4.14. SADP from a Ag_3Sn (γ) crystal with zone axis $[0\ 1\ 0]$ showing extra spots which indicate the presence of Cu_6Sn_5 (η'). The arrows indicate $(1\ 0\ \bar{1}\ 0)$ spots from Cu_6Sn_5 (η').

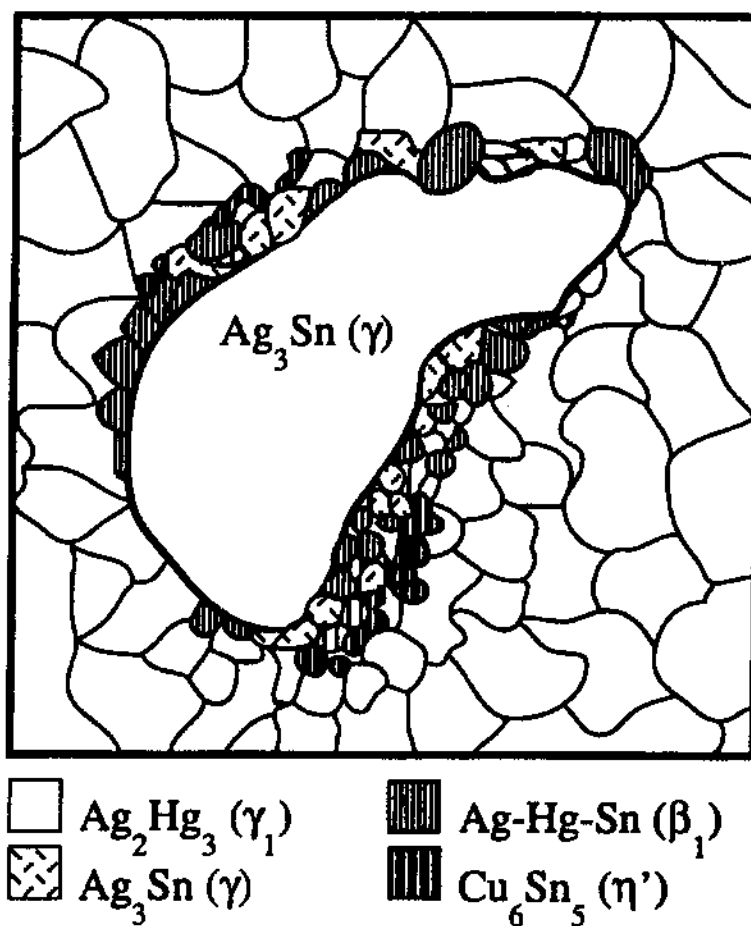
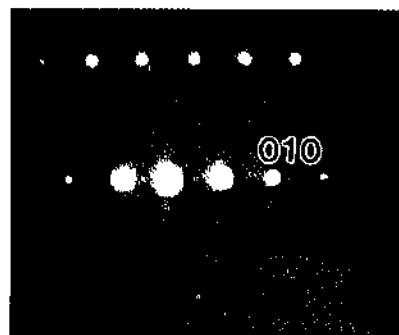
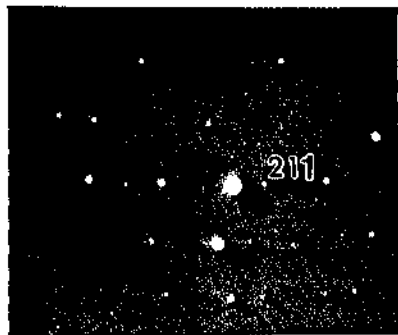


Figure 4.15 (a) A sketch of the reaction layer between γ and γ_1 . (b) Bright field image showing part of the reaction layer: (A) $\text{Ag}_2\text{Hg}_3 (\gamma_1)$, (B) $\text{Ag}_3\text{Sn} (\gamma)$, (C) $\text{Ag-Hg-Sn} (\beta_1)$, and (D) $\text{Cu}_6\text{Sn}_5 (\eta')$. (c), (d), (e) $\mu\mu\text{Ds}$ from the marked grains in (b).



(b)



(d) Ag_3Sn (γ)



(c) Ag_2Hg_3 (γ_1)



(e) Ag-Hg-Sn (β_1)

CHAPTER 4 REFERENCES

1. T. Okabe and R.J. Mitchell, Critical Rev. in Oral Biology and Medicine **7**, 23 (1996).
2. R.J. Mitchell and T. Okabe, Critical Rev. in Oral Biology and Medicine **7**, 12 (1996).
3. T. Okabe, R.J. Mitchell, M.B. Butts, and C.W. Fairhurst, J. Dent. Res. **57**, 975 (1978).
4. C. W. Fairhurst, Ph. D. Thesis, Northwestern University, Evanston IL (1966).
5. Y.C. Durandet, R.J. Finch, and D.R. Miller, Mater. Forum **17**, 51 (1993).
6. G. Petzow and G. Effenberg, *Ternary Alloys-A Comprehensive Compendium of Evaluated Constitutional Data on Phase Diagrams*, (VCH Verlagsgesellschaft, Weinheim, Germany), pp. 38-40, 256-261, (1988).
7. T. Okabe, in *Encyclopedia of Materials Science and Engineering*, edited by R.W. Cahn (Pergamon Press, Oxford), Suppl. Vol. 2, 866 (1990).
8. P.G. Boswell, Scripta Metallurgica **13**, 383 (1979).
9. T. Hanawa, H. Takahasi, M. Ota, R. F. Pinizzotto, J. L. Ferracane, and T. Okabe, J. Dent. Res. **66**, 1470 (1987).
10. D. B. Mahler, J. D. Adey and J. V. Eysden, J. Dent. Res. **54**, 218 (1975).
11. F. Aldinger and W. Kraft, Z. Metallkde. **68**, 523 (1977).
12. S. J. Jensen and P. Anderson, Scan. J. Dent. Res. **80**, 158 (1972).
13. T. Okabe, F. Ling, and R.F. Hochman, J. Dent. Res. **54**, L162 (1975).
14. D. B. Mahler and J. D. Adey, J. Dent. Res. **63**, 921 (1984).
15. R.M. Waterstrat and T. Okabe, *Intermetallic Compounds* (John Wiley & Sons Ltd.), Vol. 2, p. 575 (1994).
16. J.H. Watkins, H. Nakajima, K. Hanaoka, L. Zhao, T. Iwamoto, and T. Okabe, Dent. Mater. **11**, 24 (1995).
17. L.B. Johnson and G.C. Paffenbarger, J. Dent. Res. **59**, 1412 (1980).

CHAPTER 5

MICROSTRUCTURE OF A HIGH COPPER AMALGAM

Tytin

5.1. Introduction

Constant efforts are being made to improve the quality of existing Ag-Sn-Hg dental amalgams as described in Chapter 1. After 1960, mechanical testing of conventional amalgams revealed three different types of responses in conventional stress-strain tests. Individual tests on each phase showed: (1) unreacted particles are the strongest, (2) Ag_2Hg_3 (γ_1) is the next component, and (3) $\text{Hg-Sn}_{7.9}$ (γ_2) is the weakest component.^{1,2,3} Further corrosion tests showed that $\text{Hg-Sn}_{7.9}$ (γ_2) is the most easily corroded phase. This test led to the development of an amalgam without the γ_2 phase. The addition of Ag-Cu dispersant particles to conventional Ag-Sn particles accomplished this goal. The new amalgam proved to be more durable and showed better corrosion resistance than the older conventional one.

Asgar⁴ introduced a single composition high-Cu amalgam in 1974. Instead of using two different particles, a single ternary Ag-Sn-Cu composition was used for the alloy particles. Tytin, a commercially popular amalgam, was used in this high-Cu amalgam study. Each particle of Tytin has a single Ag-Sn-Cu composition. This chapter presents the overall microstructure⁵ and the fine details of the Tytin microstructure.

5.2. General Microstructure

The overall microstructure of Tytin amalgam is presented in Fig. 5.1(a), a backscattered scanning electron micrograph of a TEM sample. A schematic diagram of the same area (Fig. 5.1(b)), indicates the prominent phases found and verified in the present research. Unreacted spherical particles are intentionally dispersed in the matrix, since the recommended amount of Hg is insufficient to react completely with all the powder particles. The phases found in the TEM study which are predominant in the unreacted alloy particles are Ag_3Sn (γ), Ag_4Sn (β), and Cu_3Sn (ϵ). The amalgam matrix contains Ag_2Hg_3 (γ_1) as the primary phase, and fine precipitates of Cu_6Sn_5 (η'). Small amounts of Ag-Hg (β_1) are also occasionally found. The Ag-Hg-Sn (β_1) ternary phase is present in a layer surrounding the unreacted particles. The crystal structures verified in the present study are presented in Table 5.1. XEDS results are presented in Table 5.2.

The presence and location of Ag-Hg-Sn (β_1) has been clearly defined by this research. In addition, our TEM investigation shows two types of morphologies for Cu_6Sn_5 (η'): (1) small rod shaped precipitates in the matrix, and (2) large grains surrounding unreacted particles. The distribution of small Cu_6Sn_5 (η') precipitates in the matrix explains the improved mechanical properties of Tytin compared to low-Cu amalgams such as Velvalloy. The internal structure of the large Cu_6Sn_5 (η') grains was observed and documented for the first time. Furthermore, this study has revealed the fine details of the microstructure of the alloy particles.

5.3. Unreacted Particles

5.3.1. Ag_3Sn (γ)

Our study of various regions of many unreacted particles revealed a complex and inhomogeneous microstructure within the alloy particles. The main matrix is Ag_3Sn (γ) with some Ag_4Sn (β). Fig. 5.2 shows some diffraction patterns from the particles verifying the Ag_3Sn (γ) phase in the matrix.

A low magnification SEM backscattered image of a particle (Fig. 5.3) shows what appears to be a dendritic structure. Actually, TEM analysis showed this to be a two phase structure containing Ag-Sn and Cu-Sn phases. Dendrite microstructures are three-dimensional. TEM plane-section micrographs are two-dimensional representations of the three-dimensional complex structure and must be carefully interpreted.

Spherical Tytin particles are produced by atomization of the liquid alloy. The microstructure of the particle depends on the cooling rate, hence, particle size influences the scale of the microstructure because cooling rate increases with decreasing particle size. Furthermore, the outer regions of a spherical particle will have a different cooling rate than the interior. Sometimes the outer regions of particles exhibited an elongated cellular type structure. Fig. 5.4 illustrates the varied microstructure within one particle. Different types of morphologies are shown in Fig. 5.5. Studies of several rapidly solidified alloys have shown three different morphologies for samples solidified after various degrees of undercooling of the melt. With increasing undercooling, the change in nucleation and growth changes the morphology from dendritic to cylindrical (cellular) to spherical (microcrystalline). The most common morphology observed is a branched

dendritic structure.⁶

Unlike the lathe-cut particles of Velvalloy which contain large grains, Tytin particles have a fine grain structure. Fig. 5.6 is a low magnification micrograph of Tytin and the diffraction pattern. Note the difference between this diffraction pattern and the one shown in Fig. 4.3. Both patterns are from equal areas in size. However, the grain boundaries are not clearly defined in Tytin. Bright/dark field analysis and the curved streaking in the SADP suggest a mosaic crystal structure as shown in Fig. 5.7.

Dislocation networks are observed to make cell walls and low angle grain boundaries, as shown in Fig. 5.8. These dislocation tangles cause orientation variations over a range of 10° .

5.3.2. Ag_4Sn (β)

Some SAD patterns suggest the presence of Ag_4Sn (β) in the microstructure of the particles. This hexagonal, Ag-rich phase has interplanar spacings very close to those of Ag_3Sn (γ). A number of orientations of both yield indistinguishable diffraction patterns. One example is shown in Fig. 5.9. XEDS of some of the grains in the particles give a composition very close to Ag_3Sn (γ) and the results observed for Velvalloy particles. Note, however, that the large grains in Velvalloy make it easier to confirm the crystal structure. A study of splat-quenched particles of Tytin⁷ reported $\text{Ag}_4\text{Sn}(\beta)$ as the main matrix and Ag_3Sn (γ) as precipitates. The cooling rate for splat-quenched particles is much higher than that used for commercially prepared Tytin particles. Moreover, Tytin particles are heat treated by the manufacturer after they are formed by atomization. We

found only a few diffraction patterns indicating Ag_3Sn (γ) precipitates in Ag_4Sn (β) (Fig. 5.10). Our preliminary results using multiple orientations of a few crystals indicate Ag_3Sn (γ) as the main phase of the particle matrix.

5.3.3. Cu_3Sn (ϵ)

A second phase is present in the interdendritic regions of the particles. XEDS and microdiffraction verified the presence of orthorhombic Cu_3Sn (ϵ) (Tables 5.1 and 5.2). SEM observation at higher magnification revealed a dendritic structure having a blocky morphology, rather than the more familiar tree-like appearance (Fig. 5.11(a)). The Cu_3Sn (ϵ) morphology is discrete and the grains are separated from one another. The TEM micrograph in Fig. 5.11(b) shows some Cu_3Sn (ϵ) grains in the particle matrix. These grains do not have any orientation relationship with the matrix. In metallic systems, the amount of undercooling prior to solidification influences the dendritic morphology.⁸

Tilting experiments showed that the Cu_3Sn (ϵ) grains are heavily twinned and/or faulted as shown in Fig. 5.12. Occasionally, along the outer regions of the unreacted particles, grains of Cu_6Sn (η') are found, having a similar morphology (Fig. 5.13). Although XEDS was capable of distinguishing between the two phases, $\mu\mu\text{D}$ patterns were obtained to verify the results.

Careful examination of the dendritic regions revealed small Cu_3Sn (ϵ) precipitates (approximately 50 nm in diameter) in the matrix (Fig. 5.14). Figs. 5.14(a), (b), and (c) show Moiré fringes and the SADP from the same area. Analyses of Figs. 5.14, 5.15, and

other diffraction patterns show that Cu_3Sn (ϵ) diffraction spots have a symmetric relation with respect to the matrix spots. Due to the complex structure and smaller size of the matrix grains, it is difficult to obtain diffraction patterns with uniformly intense diffraction spots, that is, with **B** (incident beam direction) as close as possible to the zone axis. It is concluded that the Cu_3Sn (ϵ) phase usually has a specific crystallographic orientation relationship with the matrix. However, the details of this phenomenon to be determined by additional experimentation.

5.4. Matrix Phases

5.4.1. Ag_2Hg_3 (γ_1)

The crystal structure and chemical composition of Ag_2Hg_3 (γ_1) are given in Tables 5.1 and 5.2. BCC polycrystalline crystals of Ag_2Hg_3 (γ_1) in Tytin do not show any obvious differences compared to Velvalloy.⁹ However, unlike Velvalloy, there was no evidence of $\text{HgSn}_{7.9}$ (γ_2) in the Tytin matrix. The additional copper has completely eliminated the formation of this unwanted phase. In general, SAD patterns from a number of Ag_2Hg_3 (γ_1) grains do not show any extra spots, satellite spots or streaking (Fig. 5.10). Bright field imaging of these grains does not reveal any unusual defects, except for a few dislocations. The chemical composition also appeared uniform and consistent with the results found in the low-Cu Velvalloy samples. The previous TEM study by Boswell¹⁰ of Tytin reported faulting on (001) planes. Since standard metallurgical TEM sample preparation methods such as dimple grinding and ion milling were used in that study, the soft phases like Ag_2Hg_3 (γ_1) could have been damaged, and

defects introduced. Our results suggest that our sample preparation method does not produce defects in the TEM samples. The bright field image and SADP of Ag_2Hg_3 (γ_1) in Fig. 5.17 illustrate crystals without any obvious defects.

Cu_6Sn_5 (η') precipitates are embedded inside the Ag_2Hg_3 (γ_1) and along the grain boundaries. In addition, regions are found where the grain boundaries are not smooth (Fig. 5.18), which suggests the presence of another phase. The chemical composition of this phase has not yet been established. Detailed information about the Cu_6Sn_5 (η') precipitates is presented below.

5.4.2. Ag-Hg (β_1)

Binary Ag-Hg (β_1) phase is occasionally found in the matrix along with Ag_2Hg_3 (γ_1). The morphology is similar to that of the Ag_2Hg_3 (γ_1). Fig. 5.19 shows a large Ag-Hg (β_1) grain with Cu_6Sn_5 (η') precipitates embedded. The SADP from the same grain does not show extra spots or streaking. Therefore, it is probable that small amounts of binary Ag-Hg (β_1) form in freshly mixed amalgam via a dissolution and precipitation mechanism.

5.4.3. Cu_6Sn_5 (η')

Microdiffraction and x-ray analysis of a number of grains confirmed the presence of hexagonal Cu-Sn η' precipitates in the matrix. These rod shaped grains range from 20 - 300 nm in diameter and 60 - 800 nm in length. The distribution of these precipitates is not uniform throughout the matrix. Some regions have a large number of precipitates

embedded inside the Ag_2Hg_3 (γ_1) and at the grain boundaries. Other regions of the Ag_2Hg_3 (γ_1) matrix have hardly any precipitates. Figs. 5.17, 5.19, and 5.20 show the variation in size and distribution of these precipitates. The Cu_6Sn_5 (η') precipitates do not have a specific orientation relationship with the matrix.

The high-Cu amalgams studies by Boswell¹⁰ led to his suggesting two models for the origin of the Cu_6Sn_5 (η') precipitates: (1) dissolution of Ag-Sn-Cu alloy particles and nucleation of η' precipitates, and (2) solid-state transformation of Cu_3Sn (ϵ) particles initially present in the alloy powder to η' . Solid-state transformation by the diffusion of Sn to Cu_3Sn (ϵ) to form Cu_6Sn_5 (η') is not supported here since the morphology of the Cu_6Sn_5 (η') in the matrix is quite different than that of the Cu_3Sn (ϵ) in the particles. Okabe¹¹ has suggested a dissolution and precipitation mechanism for the formation of small rod-shaped precipitates. As mentioned previously, the low solubility of Cu in Hg leads to the rapid supersaturation of Cu in Hg. Hence, the Cu_6Sn_5 (η') precipitates nucleate and grow in the liquid Hg in the early stages of the reaction between the Hg and the alloy powder. Later in the process, the Ag_2Hg_3 (γ_1) forms around the rod shaped Cu_6Sn_5 (η') precipitates, forming the basic matrix of the amalgam. Larger Cu_6Sn_5 (η') grains are found around the periphery of unreacted particles. This observation is discussed further in section 5.5.2.

5.5. The Layer Surrounding Unreacted Particles

5.5.1. Ag-Hg-Sn (β_1)

Unreacted alloy particles in Tytin have a discontinuous and inhomogeneous

reaction layer around them. SADP and XEDS confirmed the ternary phase Ag-Hg-Sn (β_1) in the periphery of the unreacted particles. Imaging of these grains reveals a type of internal structure similar to that observed in the unreacted particles. This is an indication that the grains are not a product of a dissolution and precipitation mechanism, since Ag_2Hg_3 (γ_1) grains produced by this mechanism have very few crystal defects. Hence, Ag-Hg-Sn (β_1) is a reaction product due to diffusion of mercury into the unreacted particle. Okabe et al. studied the interface between a diffusion couple of Ag_3Sn (γ) and Ag_2Hg_3 (γ_1) using Kirkendall-type markers.¹² Their work revealed the formation of a new phase consisting of Ag-Sn-Hg, leading to the conclusion that the ternary phase was formed by interfacial reaction, not by ordinary diffusion of atoms.

5.5.2. Cu_6Sn_5 (η')

The peripheral regions of the particles also contain large, irregularly shaped Cu_6Sn_5 (η') grains approximately 1-2 μm in size. The chemical composition is the same as that of the small rod-shaped Cu_6Sn_5 (η') grains observed in the matrix. Sometimes these grains appear to grow on the residual particles, and they often show internal structure. The SEM backscattered image of Fig. 5.21 illustrates these large crystals in the microstructure. The previous TEM study by Boswell reported the same results,¹⁰ but the composition of the η' was not verified. Our results indicate the presence of small grains of Ag_3Sn (γ), Ag-Hg-Sn (β_1) and/or Ag_2Hg_3 (γ_1) inside the Cu_6Sn_5 (η'). Fig. 5.22 shows a large Cu_6Sn_5 (η') grain with internal structure. The embedded grains are Ag_2Hg_3 (γ_1) and Ag_3Sn (γ). We did not find any orientation relationship between the Cu_6Sn_5 (η') and

the embedded grains. Also, there was no evidence of Cu_3Sn (ϵ) inside the Cu_6Sn_5 (η'). Apparently, these grains are not the result of the transformation of Cu_3Sn (ϵ) to Cu_6Sn_5 (η'). They appear to be trapped inside the Cu_6Sn_5 (η') during the growth process.

The binary phase diagram suggests two forms of Cu_6Sn_5 (η'). Above 227°C , the η phase is a disordered solid solution. At a lower temperature, the η' phase has a superlattice structure with lattice parameters approximately 5 times those of the η phase (Table 5.1). Fig. 5.23 demonstrates this phenomenon. Tilting experiments were performed on a few grains to observe superlattice reflections. The grains next to the unreacted particles displayed superlattice reflections, but the few large grains far from the particles did not show evidence of any superlattice reflections (Fig. 5.22 b,c,d). There may be insufficient data about η' to reach a definitive conclusion, but it is likely that there are two different formation mechanisms for η' . Tilting experiments were not performed on the small Cu_6Sn_5 (η') grains within the γ_1 matrix.

5.6 Stability of the Phases

TEM samples were stored at room temperature. Reexaminations of the samples after 10 months storage do not show any changes in the microstructure. However, the thin edges seemed to have developed an amorphous layer, which is expected to occur due to surface oxidation. The compositions of the oxide layers on individual phases were not determined. Some particle regions gave obvious diffraction rings from SnO_2 as shown in Fig. 5.24.

5.7. Summary and Conclusions

A TEM study of Tytin, a high-Cu amalgam, was performed in the continuation of our research on the microstructure of dental amalgams. The morphology, stoichiometry and crystal structures of the major phases were established. The Tytin microstructure is the result of dissolution of the alloy particles in liquid mercury, and precipitation of different intermetallic phases in the liquid. There are always unreacted alloy particles within the microstructure. The Tytin study was focused on three different areas: (1) alloy particles, (2) the matrix formed after mixing with mercury, and (3) the reaction layer between the unreacted alloy particles and the matrix. Since TEM analyses provide information from very small regions of a sample, and amalgams have a composite structure, the overall microstructure was obtained by comparing the TEM results with corresponding SEM images.

Alloy particles have a two phase dendritic structure: Ag-Sn and Cu-Sn. The Ag-Sn regions containing Ag_3Sn (γ) + Ag_4Sn (β) phases make up the main matrix of the alloy particle. The Cu-Sn regions were identified as Cu_3Sn (ϵ) precipitates. Compared to Velvalloy, Tytin alloy particles have a fine grained structure due to multiple nucleation sites in a particle.

Ag_3Sn (γ) and Ag_4Sn (β) matrix grains show a large number of dislocations. The tangles of dislocations produce a mosaic structure. There are fine Cu_3Sn (ϵ) precipitates in the matrix with a preferred orientation within the matrix.

Addition of mercury results in a Ag_2Hg_3 (γ_1) matrix and Cu_6Sn_5 (η') rod-shaped precipitates. The additional Cu added to conventional alloy powder (low-Cu) suppresses

the formation of $\text{HgSn}_{7.9}$ (γ_2) in the matrix. The present research did not find any evidence of $\text{HgSn}_{7.9}$ (γ_2) in Tytin. The elimination of the mechanically weak γ_2 phase and the distribution of Cu_6Sn_5 (η') precipitates in the matrix explain the better mechanical properties of Tytin compared to Velvalloy.

Larger Cu_6Sn_5 (η') grains are formed in the periphery of the unreacted particles. Usually, these grains include smaller grains of unreacted alloy and/or Ag_2Hg_3 (γ_1). No orientation relation was found between the Cu_6Sn_5 (η') and the included grains. This indicates that alloy particles or other grains are nucleation sites for Cu_6Sn_5 (η'). There is no indication of a transformation from Cu_3Sn (ϵ) to Cu_6Sn_5 (η').

Occasionally, a binary Ag-Hg (β_1) phase is found in the matrix with a similar morphology to that of Ag_2Hg_3 (γ_1). Hence small amounts of Ag-Hg (β_1) form in fresh amalgam.

A well defined reaction layer is not present around the unreacted particles. However, Ag-Hg-Sn (β_1) is found in the reaction layer between the matrix and the alloy particles. These grains have crystal defects similar to those found in the alloy particles implying that the Ag-Hg-Sn (β_1) in the reaction layer is the result of solid state-diffusion of mercury into the particle, and not the result of dissolution of the particles and precipitation from the liquid.

The long-term stability of the amalgam phases was established by re-examining TEM samples after 10 months. A SnO_2 layer was observed to form on the particles.

Table 5.1. Lattice parameters of the phases in Tytin.

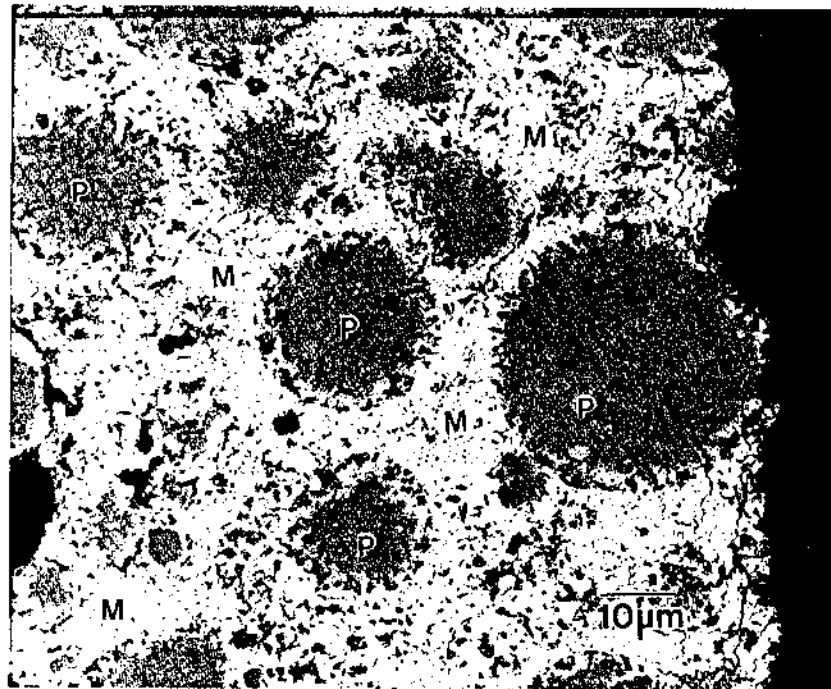
Phase	Crystal structure	Lattice parameters (Å)
$\text{Ag}_2\text{Hg}_3 (\gamma_1)$	BCC	$a = 10.04$
$\text{Ag}_3\text{Sn} (\gamma)$	orthorhombic superlattice	$a = 2.995; b = 5.159; c = 4.78$ $a = 5.968; b = 4.78; c = 5.184$
$\text{Cu}_3\text{Sn} (\epsilon)$	orthorhombic superlattice	$a = 4.56; b = 5.37; c = 4.32$ $a = 5.51; b = 38.1; c = 4.32$
Ag-Hg-Sn (β_1) is a solid solution of: Ag + 46 at. % Hg (β_1) Ag + 15 at. % Sn (β)	hexagonal hexagonal	$a = 2.99; c = 4.84$ $a = 2.93; c = 4.78$
$\text{Cu}_6\text{Sn}_5 (\eta)$ $\text{Cu}_6\text{Sn}_5 (\eta')^a$	hexagonal superlattice	$a = 4.19; c = 5.086$ $a = 20.95; c = 25.43$

^a η' is the superlattice structure, NiAs (B8₂) type.

Table 5.2. Ratios of the areas of prominent x-ray peaks. ZAF corrections were not performed.

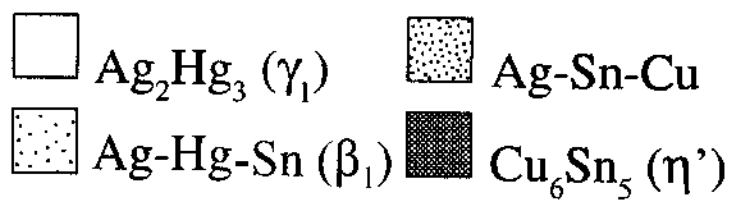
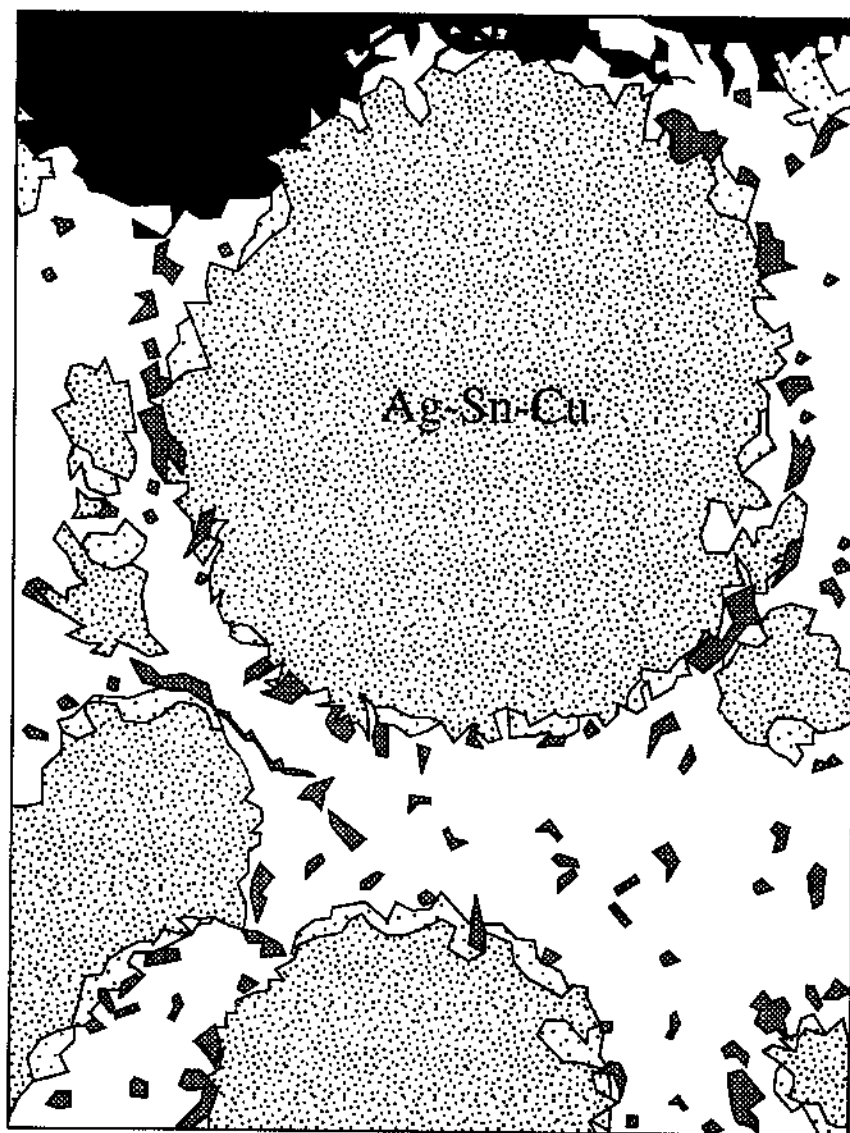
Phase	Elements	Ratio of area of peaks $L\alpha/L\alpha$
$Ag_2Hg_3 (\gamma_1)$	Hg, Ag	1.49
$Ag_3Sn (\gamma)$	Ag, Sn	2.99
$Cu_3Sn (\epsilon)$	Cu, Sn	2.92
$HgAg (\beta_1)$	Hg, Ag	0.64
Ag-Hg-Sn (β_1) reaction layer	Hg, Ag; Ag, Sn	0.4, 5.4
$Cu_6Sn_5 (\eta')$	Cu, Sn	1.34 ^b

^b For $Cu_6Sn_5 (\eta')$, the $K\alpha/L\alpha$ ratio was used.

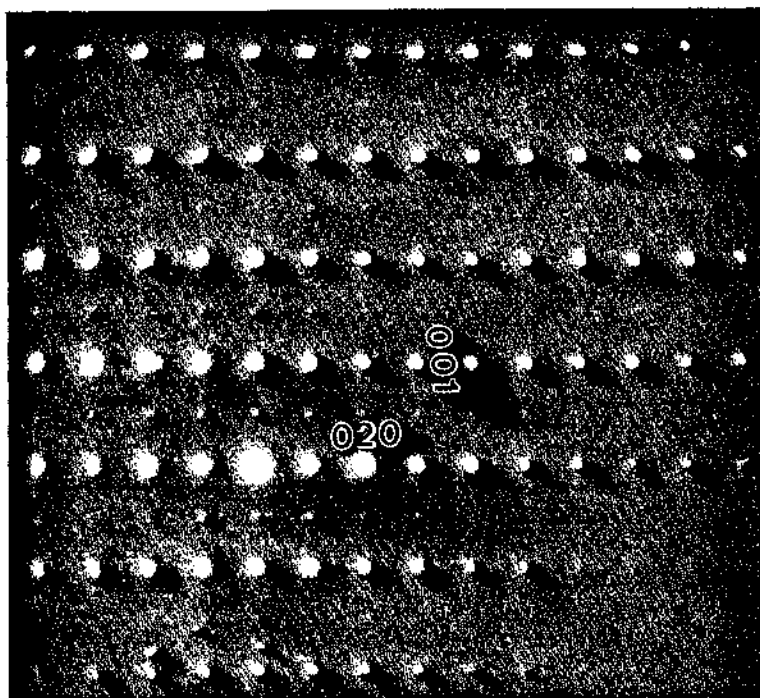


(a)

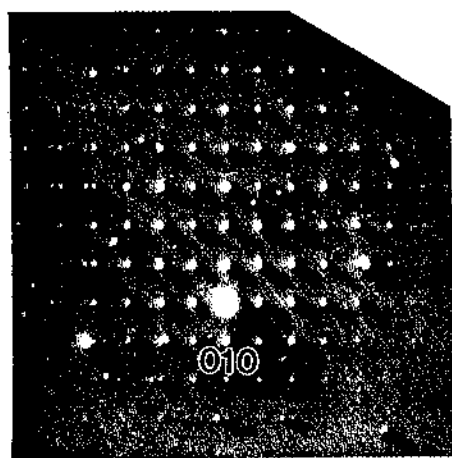
Figure 5.1. (a) Backscattered electron SEM image of a TEM Tytin sample. M, the lighter contrast areas are the matrix, and P, the dark circular regions, are the alloy particles. (b) Schematic diagram of a smaller region of (a) illustrating the locations of all the phases.



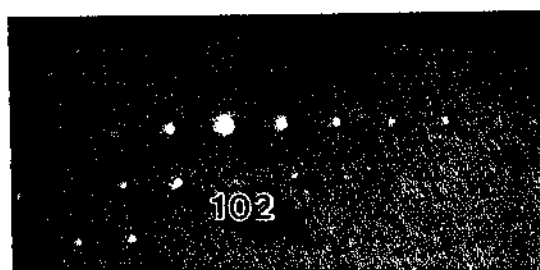
(b)



(a)



(b)



(c)

Figure 5.2. Diffraction patterns obtained from alloy particles verifying Ag_3Sn (γ).

(a) $[100]\gamma$ SADP showing superlattice spots in $[010]$ direction; (b) $[100]\gamma$, SADP zone axis close to beam direction; (c) $\mu\mu\text{D } [2 \bar{5} \bar{1}]\gamma$.

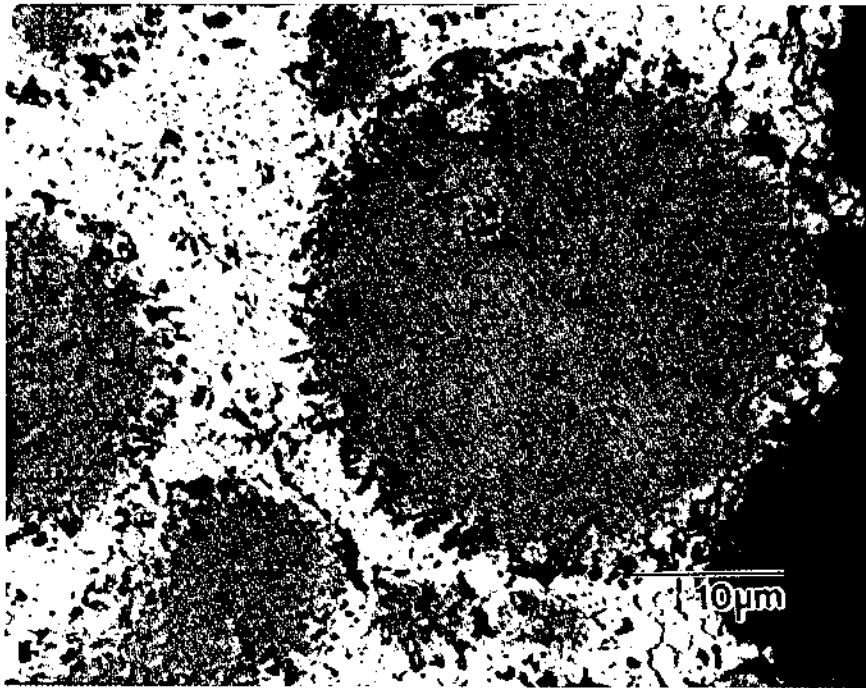


Figure 5.3. Backscattered electron SEM image of a Tytin alloy particle showing its dendritic structure.



Figure 5.4. TEM bright field micrographs showing varied microstructure from outer regions of particles to inner regions. Arrows indicate outer to inner region.

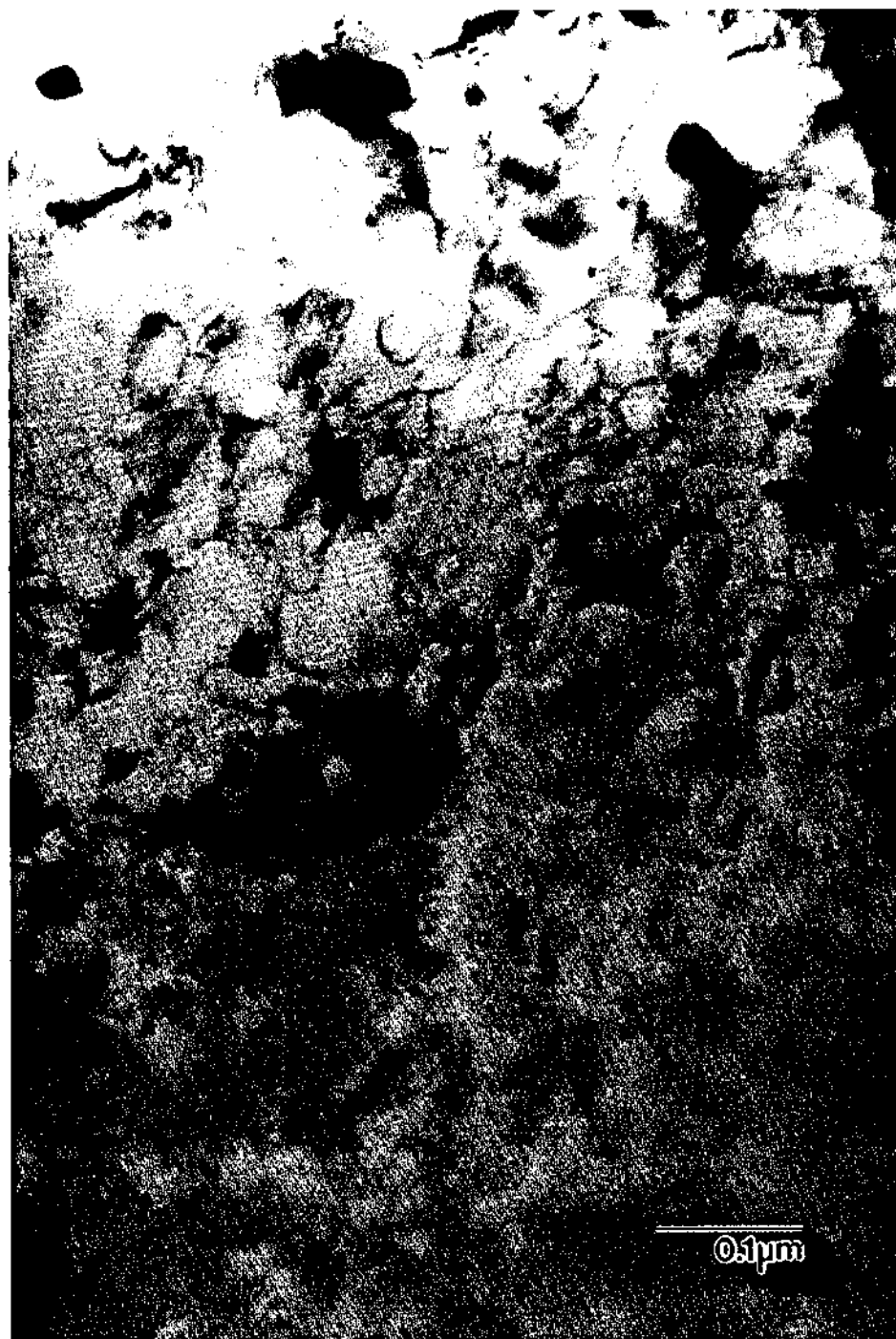


(b)



(a)

Figure 5.5. TEM images show different microstructures within the alloy particles.



(b)



(c)

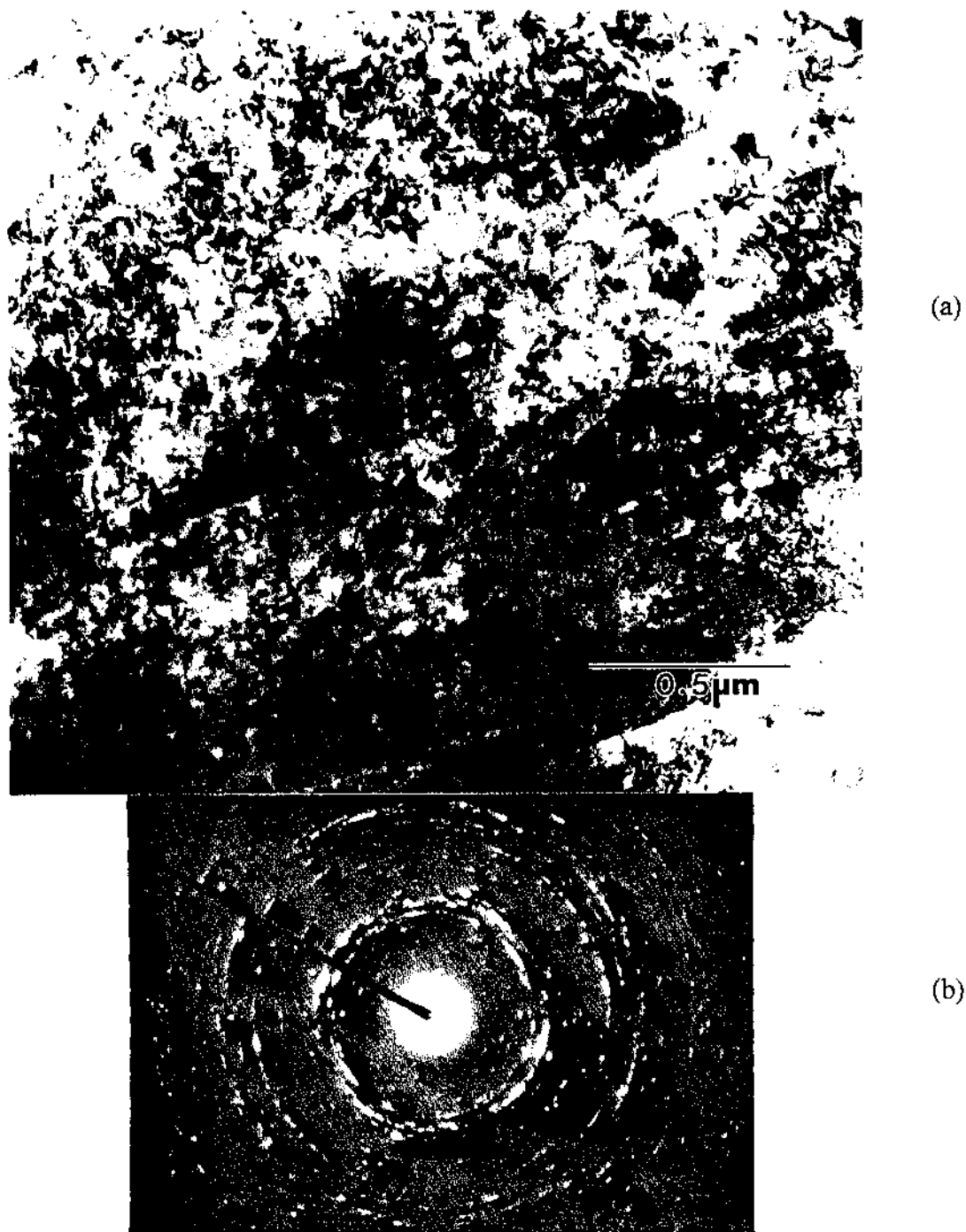


Figure 5.6. (a) Low magnification TEM image of Tytin alloy particle. (b) SADP from the same area with ring pattern showing the polycrystalline nature of alloy particles.



(a)

Figure 5.7. (a) Bright field image of the particle with diffraction pattern, $[100]\gamma$. The (020) pointer is indicates the diffraction spot used for the dark field image. (b) dark field image of (a).



(b)



Figure 5.8. Bright field image of a Tytin particle. Arrows indicate dislocation bands.

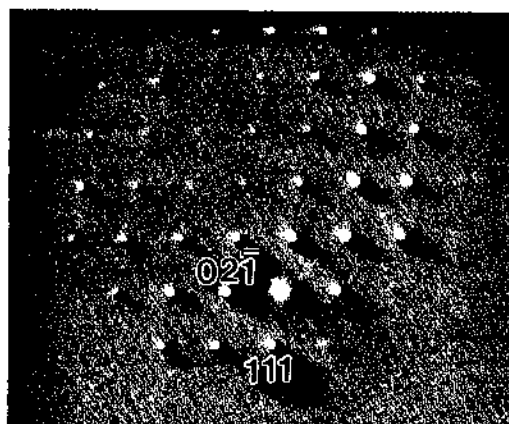


Figure 5.9. $\mu\mu$ D can be indexed as Ag_3Sn (γ) with zone axis as $[\bar{3} \ 1 \ 2]\gamma$ or as Ag_4Sn (β) with zone axis $[2 \ \bar{1} \ \bar{1} \ 3]\beta$. $(1 \ 1 \ 1)\gamma = (1 \ 0 \ \bar{1})\beta$, $(0 \ 2 \ \bar{1})\gamma = (0 \ 1 \ 1)\beta$. The angles between the planes are the same.

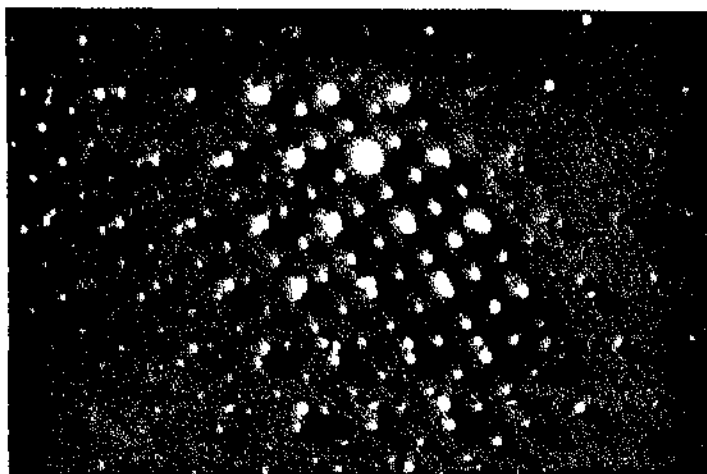
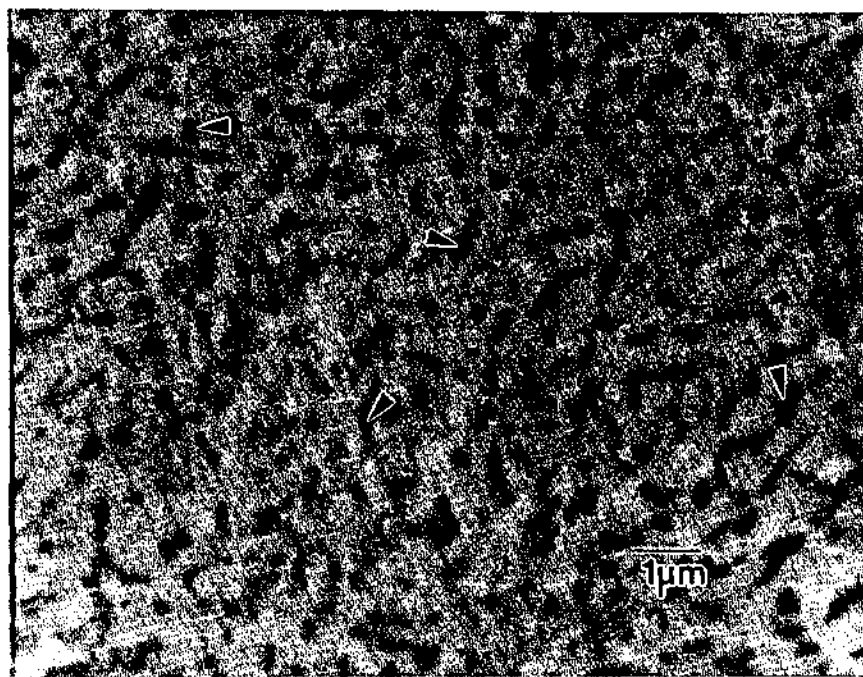
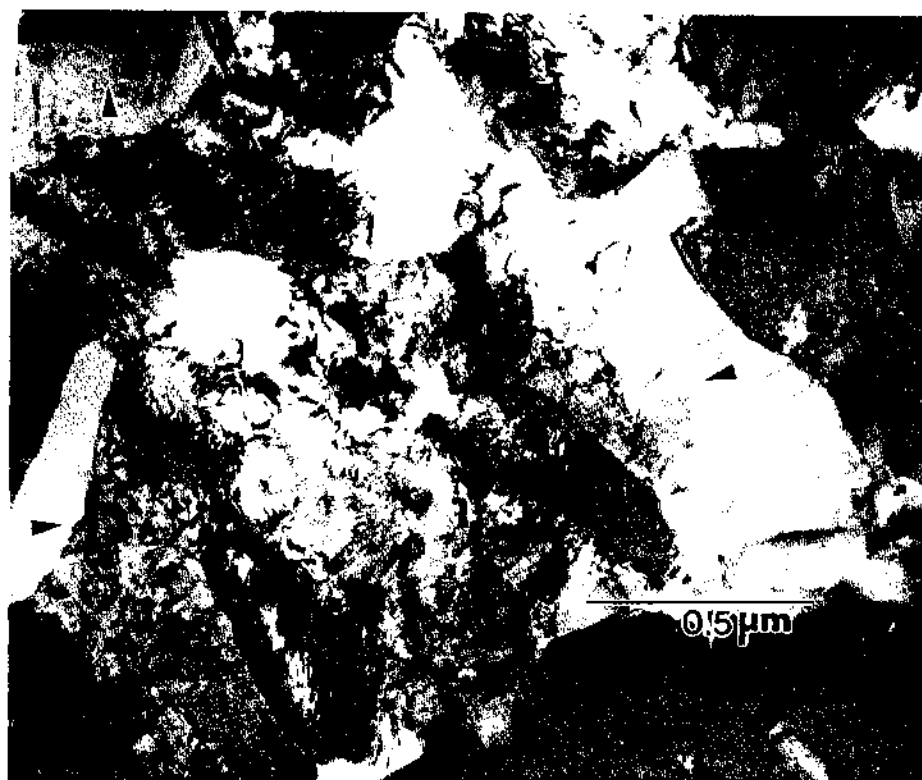


Figure 5.10. SADP from a particle grain. $[1 \ 0 \ 0]\gamma$ zone axis pattern superimposed with $[0 \ 0 \ 0 \ 1]\beta$ pattern. Darker diffraction spots are from β and lighter spots are from γ .



(a)

Figure 5.11. (a) SEM backscattered image at 10,000x showing the blocky morphology of Cu₃Sn (ε) in the particle matrix. (b) TEM image of a particle at 60,000x showing discrete Cu₃Sn (ε) grains. Arrows indicate Cu₃Sn (ε).



(b)

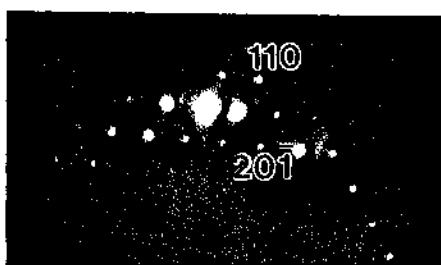


(a)

Figure 5.12. Bright field TEM images of Cu_3Sn (ϵ) grains in the particle matrix showing the heavily twinned and/or faulted substructure.



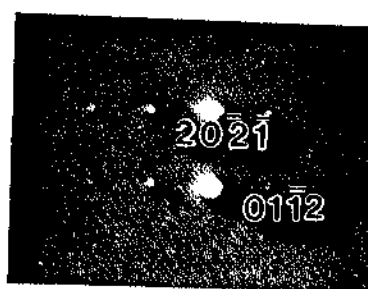
(b)



(a)



(b)

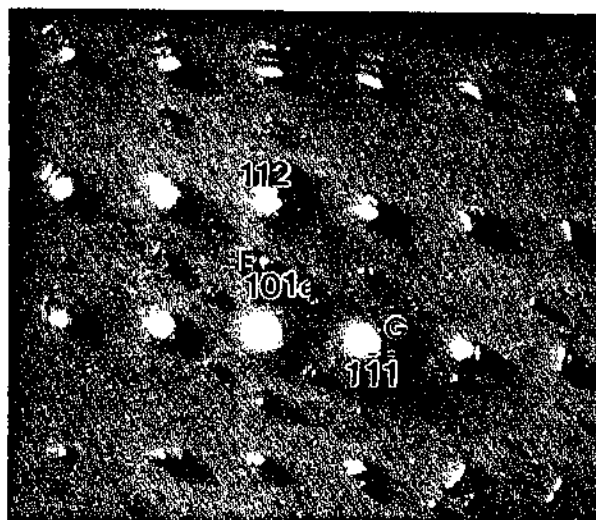


(c)

Figure 5.13. (a) $\mu\mu$ D pattern which can be indexed as orthorhombic Cu_3Sn (ϵ), $[1 \bar{1} \bar{1}]_\epsilon$. (b) Bright field TEM image showing the morphology of Cu_6Sn_5 (η') in the particle matrix. (c) $\mu\mu$ D pattern from Cu_6Sn_5 (η'), $[2 \bar{3} 1 2]$. The arrows indicate Cu_6Sn_5 (η')

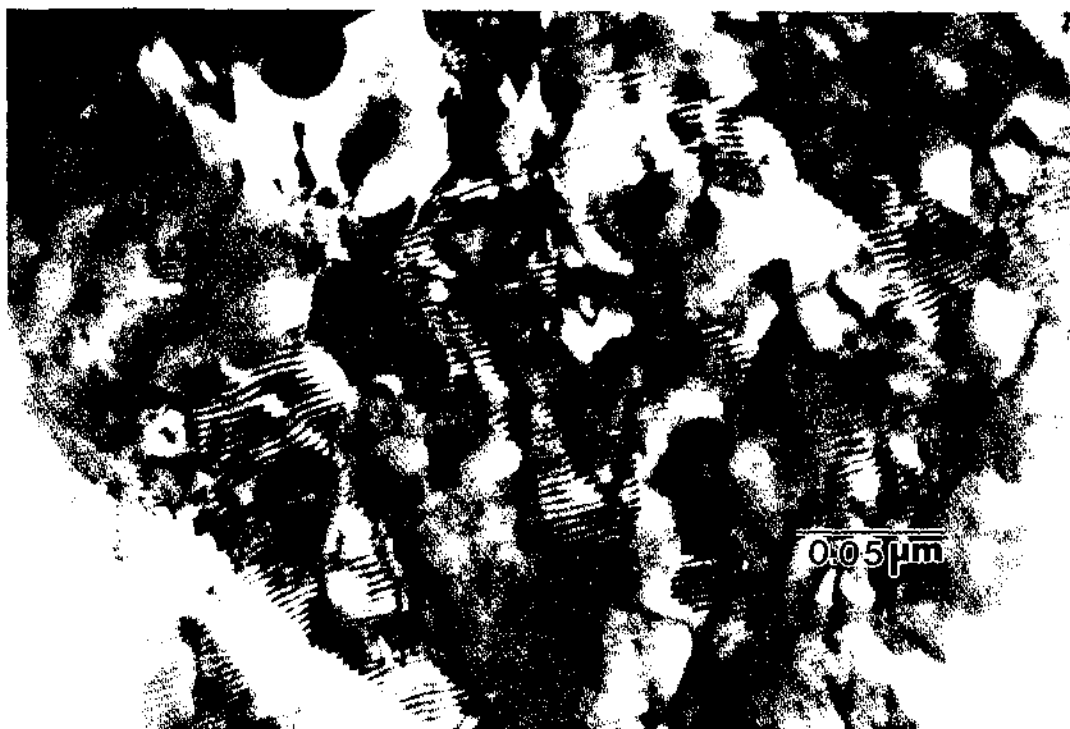


(a)

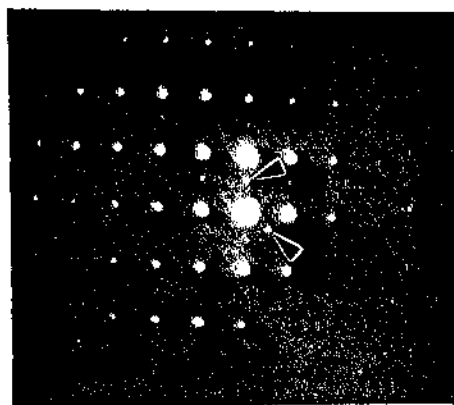


(b)

Figure 5.14. (a) Bright field image from a particle showing Moiré fringes. (b) SADP $[\bar{1} \bar{3} 2]\gamma$ or $[4 \bar{5} 1 \bar{3}]\beta$ superimposed with $[\bar{1} \bar{1} 1]\epsilon$. (c) Dark field image from spot G corresponding to $(1 \bar{1} \bar{1})\gamma$ or $(0 \bar{1} \bar{1} \bar{1})\beta$. (d) $\mu\mu$ D from the same area showing similar ϵ spots. (e) Dark field image from spot F $(1 0 1)\epsilon$ showing small precipitates of ϵ .



(c)



(d)

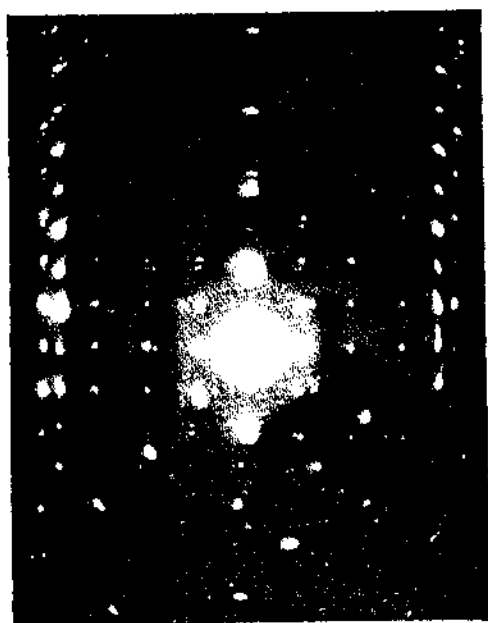


(e)

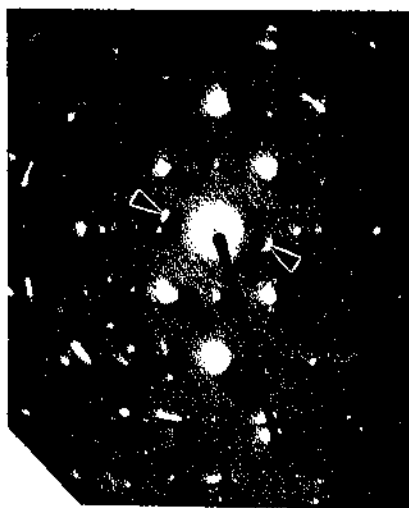


(a)

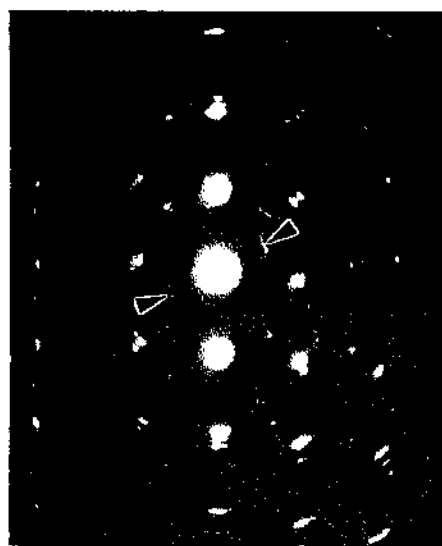
Figure 5.15. (a) Another bright field image from a Tytin particle showing Moiré fringes; (b) SADP from (a) showing extra diffraction spots from ϵ precipitates; (c), (d), and (e) SADPs showing symmetric spots from ϵ .



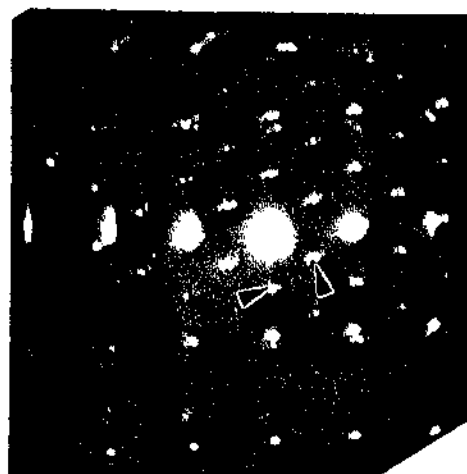
(b)



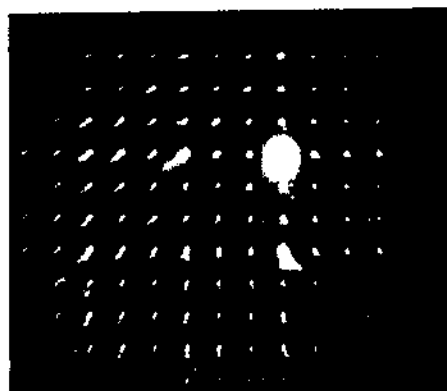
(c)



(d)



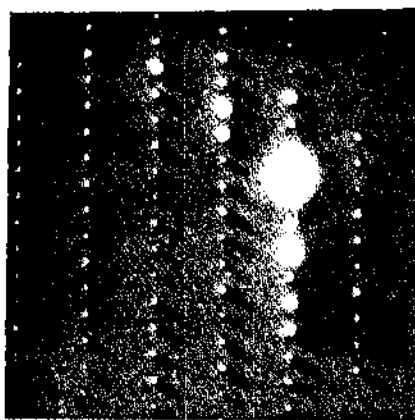
(e)



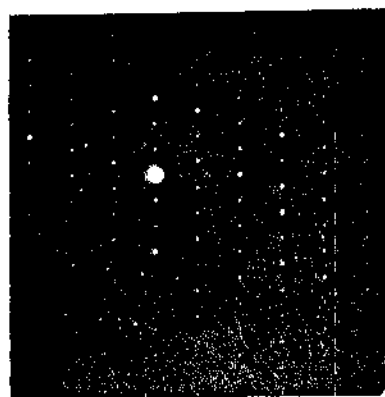
(a)



(b)



(c)



(d)

Figure 5.16. SADPs from Ag_2Hg_3 (γ_1): (a) $[0\ 0\ 1]$, (b) $[0\ 1\ 2]$, (c) $[1\ 1\ \bar{5}]$, (d) $[1\ 1\ 3]$.



Figure 5.17. TEM image from Ag_2Hg_3 (γ_1) with no obvious crystallographic defects.

Cu_6Sn_5 (η') precipitates are visible (arrows).



(a)

Figure 5.18. (a), (b) Some Ag_2Hg_3 (γ_1) grain boundaries in Tytin have a second phase present.



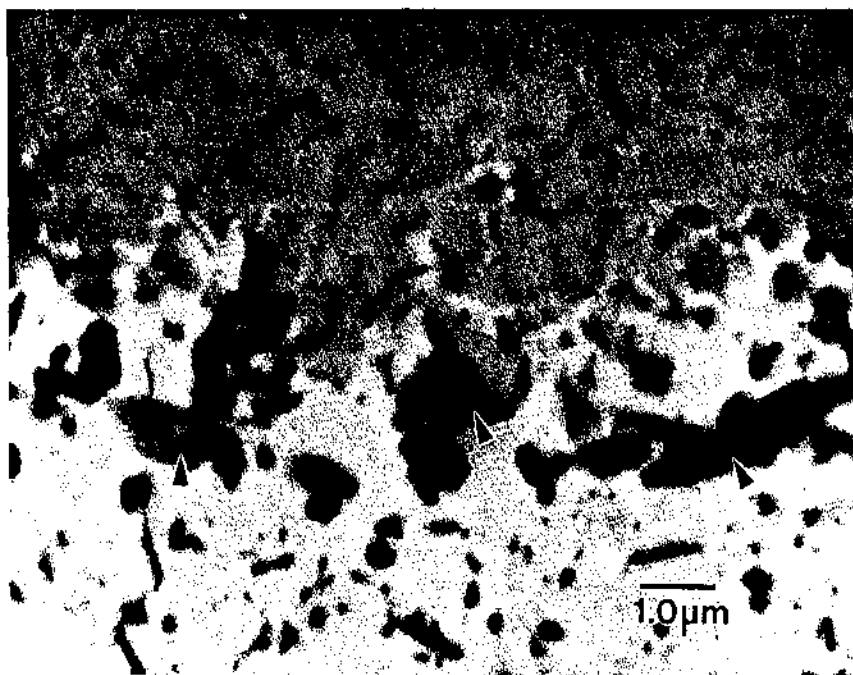
(b)



Figure 5.19. Bright field image of Ag-Hg (β_1) randomly found in the matrix. The insert is the SADP from the same grain $[2 \bar{1} \bar{1} 0]$. Arrows indicate Cu_6Sn_5 (η') precipitates.



Figure 5.20. Ag_2Hg_3 (γ_1) matrix region showing a number of small rod-shaped Cu_6Sn_5 (η') precipitates, indicated with arrows.



(a)

Figure 5.21. (a) SEM backscattered image showing the location of large Cu_6Sn_5 (η') grows around unreacted particles. (b) TEM image of Cu_6Sn_5 (η') growing on an unreacted particle. (P) unreacted particle, (N) Cu_6Sn_5 (η'), (G) Ag_2Hg_3 (γ_1).

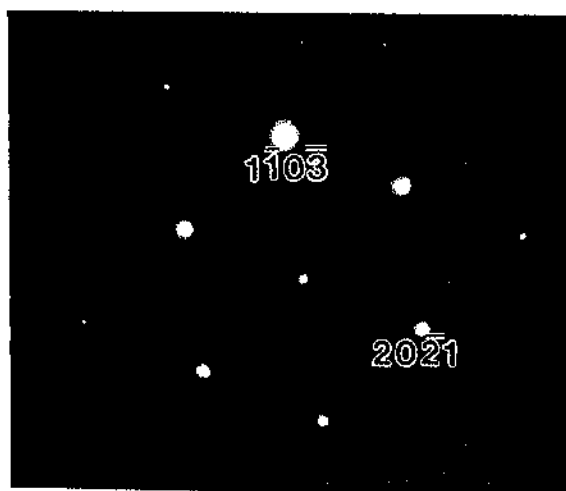


(b)



(a)

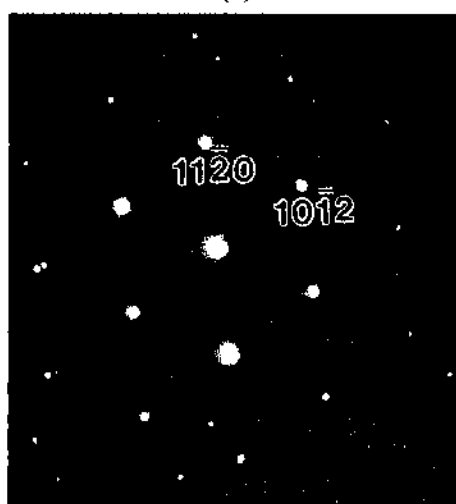
Figure 5.22. (a) Large Cu_6Sn_5 (η') grain with γ and γ_1 grains inside it; (b) SADP from the same grain, $[\bar{7} \ 11 \ \bar{4} \ 6]$ (b) SADP with a different orientation after tilting 10° , $[\bar{5} \ 4 \ 1 \ 3]$; (c) after tilting 20° , $[\bar{2} \ 2 \ 0 \ 1]$. Neither SADP shows superlattice reflections



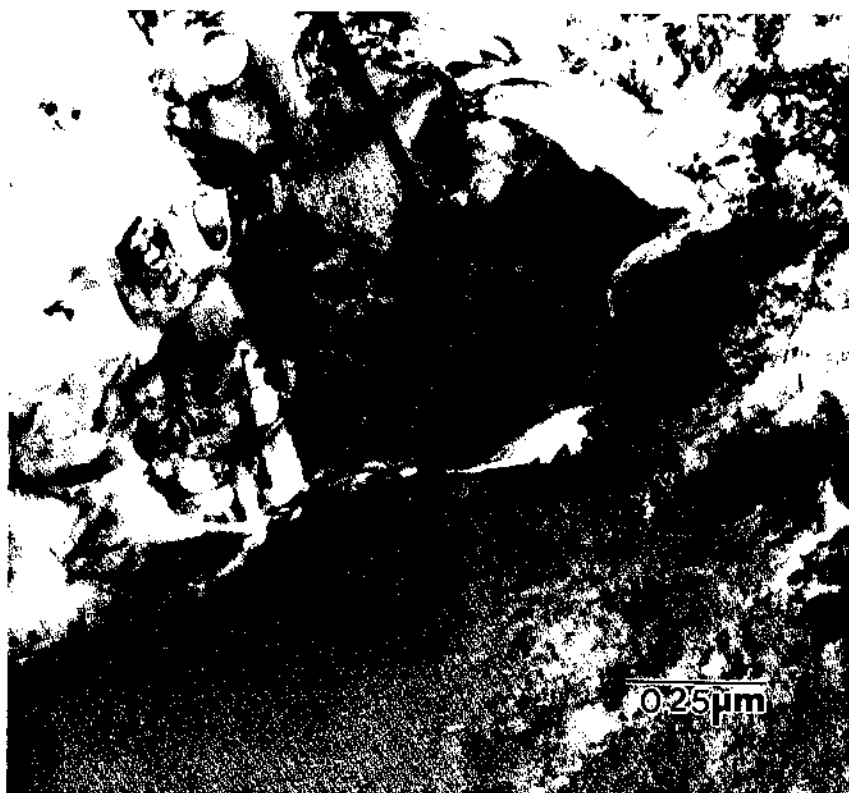
(b)



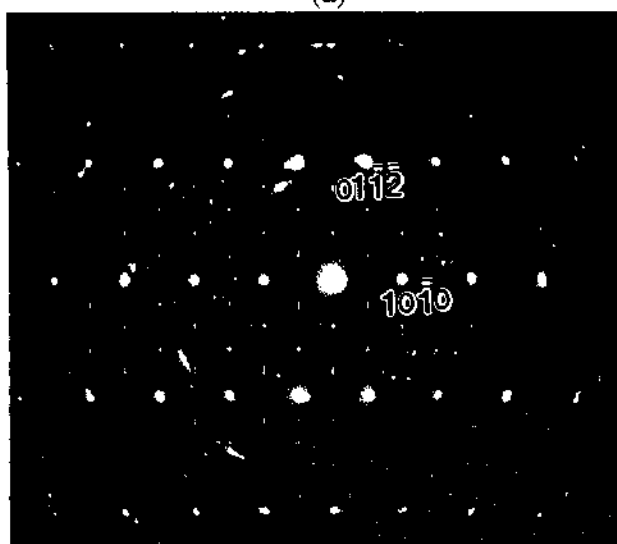
(c)



(e)



(a)



(b)

Figure 5.23. (a) Cu_6Sn_5 (η') grain in an alloy particle; (b) SADP from the same grain showing superlattice reflections. The zone axis is $[\bar{2} \ 4 \ \bar{2} \ 3]$.

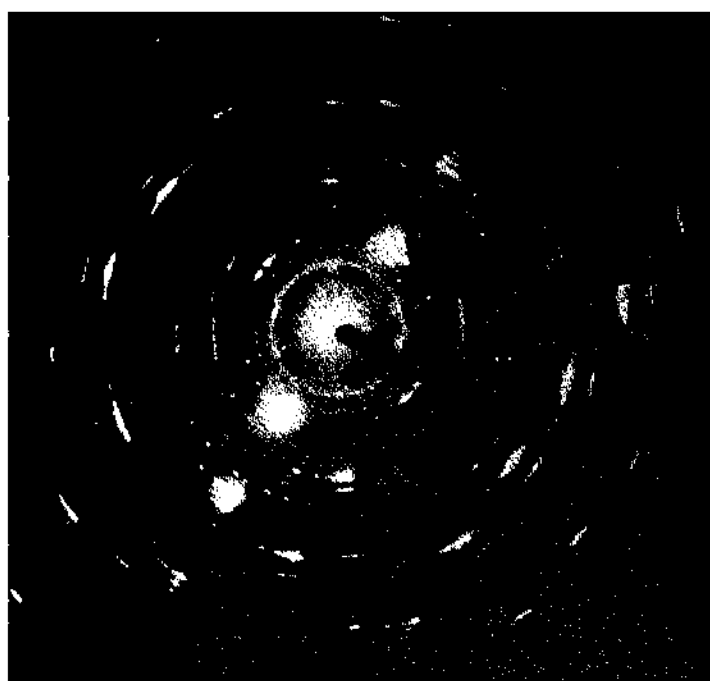


Figure 5.24. SADP from a particle showing SnO_2 rings after storing the TEM sample for 10 months at room temperature.

CHAPTER 5 REFERENCES

1. R.M. Waterstrat, J. O. M. **42**, 8 (1990).
2. T. Okabe, R.J. Mitchell, M.B. Butts, S.S. Galloway, and W.S. Twiggs, J. Biomedical Mat. Res. **19**, 727 (1985).
3. T. Okabe, R.J. Mitchell, M.B. Butts, and C.W. Fairhurst, in *Metallurgie Dentaire* (PYC editions), 395 (1981).
4. K. Asgar, in *IADR Prog. and Abst.* 53, No. 23 (1974).
5. T. Okabe, in *Encyclopedia of Materials Science and Engineering*, edited by R.W. Cahn (Pergman Press, Oxford), Suppl. Vol. 2, 866 (1990).
6. R.D. Field, A.R. Cox, and H.L. Fraser, in *Rapid Solidification Technology Source Book* (American Society for Metals, Metals Park, Ohio 44073), 420 (1983).
7. Y.C. Durandet, R.J. Finch and D.R. Miller, Materials Forum **17**, 51 (1993).
8. P.G. Shewmon, *Transformation in Metals* (McGraw Hill, Inc. New York), 156 (1969).
9. T.K. Hooghan, R.F. Pinizzotto, J.H. Watkins, and T. Okabe, J. Mater. Res. **11**, 2474 (1996).
10. P.G. Boswell, Scripta Met. **13**, 383 (1979).
11. T. Okabe and R.J. Mitchell, Crit. Rev. Oral. Bio. Med. **7**, 23 (1996).
12. T. Okabe, F. Ling, and R.F. Hochman, J. Dent. Res. **54**, L162 (1975).

CHAPTER 6

SUMMARY

Dental amalgams are a major restorative material for the filling of tooth cavities. Since it is the oldest material in dentistry for tooth restoration, numerous researchers have studied this material since the late 1800s, and constant efforts have been made to improve its clinical performance. Indeed, today's amalgams are more durable than ever before. Mr. G. V. Black, the pioneer of amalgams, was the first person to systematically study the properties of dental amalgams versus their elemental composition. His empirical observation regarding the amount of Sn necessary for minimal dimensional change is valid even today. Later, in the 1950s, optical microscopy (OM) and x-ray diffraction (XRD) helped identify the phases in low Cu amalgams and the formation reactions. In 1970, high Cu amalgams were developed. Also in the 1970s, scanning electron microscopy (SEM) with x-ray energy dispersive spectrometry (XEDS) and wave length dispersive spectrometry (WDS) helped explain the sequence of reactions in freshly made amalgams. Qualitative and quantitative information from even smaller volumes of the sample have been achieved since that time. Although other composite materials have been introduced in dentistry, amalgams are still predominant because of their superior clinical properties, mechanical properties, corrosive properties, and durability. Also contributing to the popularity of amalgams is their low cost and ease of preparation prior to compaction into a prepared tooth cavity.

In order to improve the properties of existing amalgams, it is necessary to understand the associated amalgamation and setting reactions. This can be achieved by high resolution microstructural characterization of the amalgams. This dissertation is a microstructural study of dental amalgams using analytical transmission electron microscopy (TEM).

Amalgams are prepared by mixing alloy particles, which contain Ag, Sn and Cu as the major constituent elements, with liquid Hg. The resultant plastic mass is compacted into the prepared tooth cavity where it solidifies and hardens by chemical reaction. Two types of amalgams were studied: low Cu and high Cu. Although low Cu amalgams are not now clinically popular, they are a valid starting material for this research since they are relatively simple. Velvalloy, a low Cu amalgam, was studied first, followed by a study of Tytin, a high Cu amalgam.

Extreme TEM sample preparation difficulties were overcome by developing a mechanical polishing methodology. A tripod polisher was used to successfully produce electron transparent areas using the "wedge technique." This unconventional technique, designed for semiconductor materials, was modified for dental amalgam samples. This technique eliminates the need of dimple grinding and ion milling which damage the microstructure.

The superior spatial resolution of the TEM made it an obvious choice to study amalgam microstructures. Amalgams have a composite structure. Unreacted particles of different sizes are embedded in a Hg containing matrix. It is not possible to produce an electron transparent area wide enough to show all the phases at one location. At times,

the TEM was operated in SEM mode in order to correlate the electron transparent areas in the context of the overall microstructure of the amalgam. Backscattered electron images were obtained in an SEM for the same areas analyzed in the TEM, and the results were found to be consistent with those previously published in the literature.

Selected area electron diffraction and XEDS were employed to identify grain structures $> 0.5 \mu\text{m}$ in size. Bright/dark field analysis was used to confirm the locations of grains and small precipitates within the microstructure. Smaller grain structures and small precipitates ($< 0.5 \mu\text{m}$) were studied by simultaneous use of micro-microdiffraction ($\mu\mu\text{D}$) and XEDS. Single crystal electron diffraction patterns were used to identify the different phases. Experimental d-spacings were compared to interplanar spacings calculated from the known lattice parameters. A double-tilt beryllium TEM sample holder was used to obtain multiple crystal orientations in order to: (1) distinguish between crystals with similar chemical composition and similar interplanar spacings, (2) determine the orientation relationships of the phases, and (3) observe superlattice reflections for selected phases.

TEM specimens of Velvalloy (low Cu amalgam) and Tytin (high Cu amalgam) were prepared using the wedge technique. Subsequent TEM examination and microanalysis of both samples gave fine microstructural details hitherto unknown. The morphology, chemical composition, and crystal structures of the phases in Velvalloy and Tytin were established.

1. Velvalloy Low-Cu Amalgam

- (i). The microstructure consists mainly of a Ag_2Hg_3 (γ_1) plus HgSn_{7-9} (γ_2) matrix surrounding unreacted Ag-Sn (+Cu) particles. This observation supports the previously published dissolution/precipitation mechanism.
- (ii). Unreacted lathe-cut particles consist of a few crystals of Ag_3Sn (γ) per large particle ($\sim 5\text{-}10\ \mu\text{m}$). No evidence of a Cu containing phase was found. The Ag_3Sn (γ) grains have a mosaic internal structure.
- (iii). Small amounts of binary Ag-Hg (β_1) with the same morphology as Ag_2Hg_3 (γ_1) are occasionally found in the matrix.
- (iv). A small amount of Cu_6Sn_5 (η') is observed. Clusters of equiaxed grains are present in the matrix.
- (v). A thin, discontinuous reaction layer exists between the Ag_3Sn (γ) alloy particles and the Ag_2Hg_3 (γ_1) matrix. It consists of two distinct layers: the inner layer (next to the Ag_3Sn (γ) alloy particles) is a mixture of fine grains of Ag_3Sn (γ) and Ag-Hg-Sn (β_1); the outer layer is composed of fine grains of Ag_2Hg_3 (γ_1) and occasionally Cu_6Sn_5 (η').
- (vi). For the first time, the Ag-Hg-Sn (β_1) ternary phase was clearly identified in fresh amalgam at room temperature. The β_1 found in a reaction layer between Ag_3Sn (γ) / Ag_2Hg_3 (γ_1) is primarily a ternary Ag-Hg-Sn phase, as suggested by the ternary phase diagram. These grains have crystal defects similar to those found in the unreacted particles. This indicates that these grains are formed through solid state diffusion of Hg into the

particles and not via dissolution/precipitation.

- (vii). A thin, fine grained ZnO layer may exist between the $\text{HgSn}_{7.9}$ (γ_2) phase and the surrounding Ag_2Hg_3 (γ_1) matrix.
- (viii). Electron transparent sections of Ag_2Hg_3 (γ_1) are stable at room temperature for at least 140 days, unless they are too thin to form protective oxide films.
- (ix). Ag_2Hg_3 (γ_1)/ Ag_2Hg_3 (γ_1) grain boundaries are smooth.
- (x). The $\text{HgSn}_{7.9}$ (γ_2) phase is polycrystalline, not a single crystal.
- (xi). A ZnO layer is associated with the $\text{HgSn}_{7.9}$ (γ_2) phase.

(2) Tytin High-Cu Amalgam

- (i). The microstructure consists of a Ag_2Hg_3 (γ_1) matrix surrounding spherically shaped unreacted Ag-Sn-Cu particles. This observation supports a dissolution/precipitation mechanism.
- (ii). No evidence of $\text{HgSn}_{7.9}$ (γ_2) is found in the matrix. The addition of Cu has completely suppressed the formation of $\text{HgSn}_{7.9}$ (γ_2) in the matrix.
- (iii). Rod-shaped Cu_6Sn_5 (η') precipitates are embedded inside the Ag_2Hg_3 (γ_1) and at grain boundaries in the matrix. The Cu_6Sn_5 (η') precipitates are 20 - 300 nm in diameter and 60 - 800 nm long, and are non-uniformly distributed.
- (iv). The alloy particles have a dendritic microstructure and contain a Ag_3Sn (γ) plus Ag_4Sn (β) matrix, and Cu_3Sn (ϵ) precipitates. The particle matrix has

a mosaic structure similar to the particles in Velvalloy. However, the grains are very small compared to those of Velvalloy particles.

- (v). Cu_3Sn (ϵ) is present in the alloy particles in two different morphologies: (1) fine precipitates, ~ 50 nm in diameter with an orientation relationship with the matrix, and (2) discrete grains, ~ 100 nm in diameter and ~ 500 nm long.
- (vi). Two morphologies are observed for Cu_6Sn_5 (η'): (1) large grains (~ 1 - 2 μm), mostly irregularly shaped, are formed in the periphery of unreacted particles, and (2) smaller rod-shaped grains are embedded in the Ag_2Hg_3 (γ_1) and along the grain boundaries.
- (vii). The large Cu_6Sn_5 (η') grains include small grains of Ag_3Sn (γ) and/or Ag_2Hg_3 (γ_1). There was no indication of transformation of Cu_3Sn (ϵ) to Cu_6Sn_5 (η'). The Cu_6Sn_5 (η') grains adjacent to unreacted particles show superlattice reflections, but the few Cu_6Sn_5 (η') grains distant from the particles do not show superlattice reflections.
- (viii). As in the case of Velvalloy, binary Ag-Hg (β_1) is occasionally found in the matrix. The ternary Ag-Hg-Sn (β_1) forms through solid state-diffusion of mercury into the alloy particles, not through precipitation from the liquid.
- (ix). Ag_2Hg_3 (γ_1)/ Ag_2Hg_3 (γ_1) grain boundaries are not smooth, suggesting the presence of another phase.
- (x). The electron transparent areas of Tytin remain unchanged after 10 months of storage at room temperature. However, oxide layer formation does

occur during the storage. Unreacted particle areas show SnO_2 formation on the surface.

APPENDIX
ANALYTICAL MICROSCOPY

A.1 Analytical Electron Microscopy (AEM)

AEM is a powerful tool in materials science, and a solid foundation for the design of new commercial electron microscopes. Multiple microanalysis techniques such as microdiffraction, electron energy loss spectroscopy (EELS), and x-ray energy dispersive spectroscopy (XEDS) can be combined in a single instrument. Dedicated scanning transmission electron microscopes (STEM) are considered by some as an ideal AEM. The addition of analytical techniques to conventional TEMs have led to high resolution microstructural analysis (< 10 nm) with quantitative chemical analysis. Each of the two instruments, dedicated STEM and TEM/STEM, have advantages, depending on the purpose. A brief general introduction to the microanalytical techniques used in this research is presented here.

A.2 STEM

The STEM is an amalgamation of two major electron beam characterization techniques: scanning and transmission electron microscopy. Fundamentally and functionally, TEM and STEM are essential components of AEM. In contrast to a stationary large diameter electron probe ($\sim 1\mu\text{m}$), the electron beam is focussed to a small probe (~ 5 nm) while operating in the STEM mode.¹ This probe is raster scanned across the sample. Fig. A.1 shows the difference between image formation in TEM and STEM. In TEM, a coherent and approximately parallel beam illuminates the sample and a magnified image is formed in the objective lens image plane. This stationary image is magnified and projected onto a fluorescent screen. In STEM, a convergent incoherent

electron beam scans the sample with a rastering motion. With a thin sample, transmitted electrons can be obtained, and the objective lens recombines the transmitted electrons from all scanned points to a fixed region in the back focal plane. Intermediate and projector lenses are used to transfer the image to an electron detector in place of the fluorescent screen. The signal is then used to modulate the brightness of a CRT display on a point-by-point basis. The STEM image on the CRT is equivalent to the bright field TEM image if the directly transmitted beam is collected. Since the incident beam is not parallel, the STEM image is time dependent.

Diffracted electrons are also focussed in the back focal plane of the objective lens. A dark field image (as in conventional TEM) can be obtained by detecting the off-axis diffracted electrons. Analogous to SEM, secondary and backscattered electrons can be collected from thin or thick samples in STEM mode to obtain the corresponding images.

A.3 X-ray Microanalysis

When a high energy electron beam strikes an electron transparent sample, besides SEM and TEM images, additional signals useful for microanalytical analysis are also produced. Some of the possible signals which are primarily used for analysis in TEM are shown in Fig. A.2. When a fine focussed electron probe is positioned at a single point of interest on the sample, localized information can be obtained from the available signals. Usually, an x-ray energy dispersive spectrometer (XEDS) is used for AEM. X-ray microanalysis permits identification of the elemental constituents of a sample with resolution limits of 0.5- 0.1 wt%. Using thin samples (~ 10 nm) and a small spot size

(~ 1-2 nm) using a field emission gun (FEG), minimum elemental detectability <0.1 wt% is possible.² The spatial resolution is determined by the size of the x-ray activation volume, on the order of 10 nm.

A.3.1 X-ray Lines

The interaction of the electron beam with the sample produces two types of x-rays. Bremsstrahlung or continuum x-rays are generated as the electrons are decelerated through interactions with the nuclear cores of the atoms in the sample. These x-rays are the noise component of the total x-ray signal, and constitute a background intensity across the full energy range of the spectrum. The continuum x-rays have an intensity that varies as $(E_0 - E)/E$, where E_0 is the electron beam energy and E is the x-ray energy.

The second type of x-rays are produced by direct interaction of high energy electrons with the sample. When the electron beam removes an inner core electron, an electron from a higher energy level falls to the inner shell vacant state (Fig. A.3(a)). Transition of an electron from higher energy to lower energy is accompanied by a release of energy in the form of a photon. The released energy is a function of the difference between the two energy levels. Since the energy differences between two energy shells are well defined and specific to each element, the energy of the x-ray photon is characteristic of the emitting atom.³

Because most elements have multiple energy shells, more than one x-ray energy may be produced. Each emitted x-ray energy is named after the shell of initial vacancy such

as K, L, M, etc. The shell of the electron filling the vacancy is represented by a Greek subscript letter such as K_{α} , K_{β} . Nomenclature of a few of these x-ray lines is shown in Fig. A.3(b).⁴ With increasing atomic number, the nomenclature gets more complex due to the multiplicity of shells and subshells.

The spectrometer (XEDS) counts and sorts the characteristic x-rays on the basis of energy. The spectrum is plotted with the number of x-rays as the ordinate and the energy as the abscissa. Peaks in the spectrum correspond to specific electron transitions in specific elements. The energy of the peak identifies the element. The number of counts in the peak corresponds to number of x-rays detected and is related to the concentration of the element.

A.3.2 X-ray Energy Dispersive Spectroscopy (XEDS)

The XEDS detector is a reverse-biased p-i-n diode. Usually, lithium-drifted silicon is used to convert the x-ray energy into charge. X-rays entering the detector create electron-hole pairs in the semiconductor. The reverse biased p-i-n diode collects the electrons and holes and converts this to a voltage pulse with a height proportional to the charge. The number of electron-hole pairs generated is directly proportional to the energy of the x-ray. The magnitude of the voltage pulse is used to determine the incident x-ray energy.

Quantitative x-ray analysis of a bulk material requires correction for the differences in the electron scattering efficiency related to atomic number (Z), self-absorption of x-rays (A) within the sample, and fluorescence (F) of x-rays. Fig. A.4

schematically shows the activation volume for these interactions. In SEM, even with small probes, the x-rays are generated from a region $\sim 1\text{-}2\text{ }\mu\text{m}$ in diameter due to electron scattering. In contrast, TEM samples are very thin, and the activation volume is small, as shown in Fig. A.4. X-ray microanalysis of thin foils has the distinct advantage of better spatial resolution over analysis performed on bulk materials in an SEM because the analyzed volume is substantially reduced. Simple and straightforward compositional calculations can be performed because ZAF corrections may be omitted.⁵ It is possible to estimate the stoichiometric composition using the peak heights. However, a computer is usually used to calculate the composition taking x-ray production cross-sections into account.

A.3.3 The Cliff-Lorimer Ratio Technique

It is assumed that an electron transparent sample is thin enough to ignore any absorption A and fluorescence F corrections. Quantitative microanalysis can be easily performed using the equation

$$\frac{C_A}{C_B} = k_{AB} \frac{I_A}{I_B} \quad (1)$$

where C_A and C_B are the wt% of elements A and B, and I_A and I_B are the characteristic x-ray intensities above background in the analyzed volume. k_{AB} is an appropriate proportionality factor.⁴ The values of k_{AB} were first measured by Cliff and Lorimer (1975), hence k_{AB} is also known as the Cliff-Lorimer factor. This factor is independent of specimen composition and thickness, but varies with the energy of the incident electrons.

Quantitative analysis of binary systems can be obtained by measuring only I_A and I_B , because $C_A + C_B = 100\%$ of the sample. Equation (1) can be generalized to ternary and higher order systems as follows

$$\begin{aligned}\frac{C_C}{C_A} &= k_{CA} \frac{I_C}{I_A} \\ \frac{C_C}{C_B} &= k_{CB} \frac{I_C}{I_B}\end{aligned}\tag{2}$$

and

$$\begin{aligned}C_A + C_B + C_C &= 100\% \\ k_{CA} &= \frac{k_{CB}}{k_{AB}}\end{aligned}\tag{3}$$

A.4 Micro-microdiffraction ($\mu\mu$ D)

Microdiffraction can be broadly defined as the acquisition of electron diffraction information from a region $<0.5 \mu\text{m}$ in diameter. This is the spatial limit of conventional selected area diffraction (SAD) patterns in the TEM. The conventional SAD patterns use an aperture in the image plane of the objective lens to create a virtual aperture in the specimen plane. Under these conditions, the spatial resolution is limited by both spherical aberration and the ability to focus both the aperture and the image in the same plane. The error in area selection,⁶ A , is given by

$$A = C_s (2\theta)^3 + D (2\theta)\tag{4}$$

where

C_s = spherical aberration coefficient

D = minimum focus step, i.e. error in focus

θ = Bragg angle

An area selection of $\sim 0.5 \mu\text{m}$ is a theoretical lower limit for most commercial TEMs. Experimentally, the analysis area is limited because electron microscope apertures $< 5\text{-}10 \mu\text{m}$ in diameter contaminate very quickly. The actual area of selection depends on the demagnification of the aperture image between the image and sample planes. An aperture which selects an area $< 500 \text{ nm}$ in diameter is not of any use, because the error in area selection is about the same order as its radius (equation (4)). The microscope must be carefully and accurately adjusted for small selected areas. Usually, diffraction patterns are obtained from $10\text{-}100 \mu\text{m}$ areas, which are large compared to many of the small features of interest in the microstructure, such as precipitates.

Various microdiffraction techniques have been invented since the early development of TEM. Convergent beam diffraction (CBD), invented by Kossel and Möllenstedt in 1939, is the most commonly used technique for microdiffraction. This technique is easy to use in any TEM equipped with a STEM unit. The technique requires a strong upper objective lens or the addition of a mini-lens to a conventional TEM. The second condenser lens (C_2) is turned off or is only very weakly excited. A strong upper objective lens (working as a third condenser) produces a convergent probe of electrons ($\sim 10\text{-}100 \text{ nm}$ in diameter) on the surface of the sample. This generates a stationary diffraction pattern in the back focal plane of the objective lens. In contrast to CTEM, the

diffraction maxima are discs, not spots. Usually, the scanning probe is stopped on the area of interest. This technique has a spatial resolution equal to the volume sampled by the probe. Ideally, the probe size is the spatial resolution limit, but in practice spreading of the beam determines the resolution.

The effect of varying the beam convergence angle 2α on the CBDP is shown in Fig. A.5. When discrete maxima are formed, the pattern is known as a Kossel-Möllenstedt (K-M) pattern. When all maxima overlap, Kossel patterns are formed. The size of the diffraction discs depends on the convergence angle (2α). For K-M patterns, the diffraction discs should not overlap. Hence a suitable C_2 aperture is selected such that $2\alpha < 2\theta$ where θ is the Bragg angle for the particular specimen being analyzed. CBDP can be obtained in both TEM and STEM modes. When CBDP are generated in TEM mode, the illuminated area is small and reduced diffraction contrast is obtained due to the smaller probe size. The image intensity is very low which makes it difficult to correctly focus the probe on the sample.

When CBDP is used in the simplest form, i.e., measurement of inter-spot spacing and angles to give two dimensional crystal structure information, it is termed 'microdiffraction.' This is achieved by using a very small convergence angle (a very small C_2 aperture) and high angular resolution. In this case, the diffraction discs do not provide any internal diffraction contrast information.

JEOL, the manufacturer of the TEMs used in this work, uses the term micro-microdiffraction ($\mu\mu D$) when a fully focussed probe is used to generate a microdiffraction

pattern. In our work, the intermediate and projector lenses were used to fully focus the diffraction patterns.

A.5 Operational Details for Microanalysis in the JEOL 200CX

In the scanning mode (SM) of the JEOL 200 CX equipped with an EM-ASID3D unit, the objective lens is highly excited. The lens work as a three lens independent system (Fig. A.6). The electron beam is deflected by the scanning coils. The prefield or upper objective lens converges the beam and focuses it on the thin sample. A focused STEM image of the desired field of view is obtained on the CRT as described in the JEOL manual.⁷ The probe diameter is inversely proportional to the beam divergence as shown in Fig. A.7. The beam divergence is selected by the condenser knob (C_2). The following procedure is used to obtain a micro-area diffraction pattern.

1. $\mu\mu$ DIFF switch is depressed, PL switch at manual, and the image is focused with focus knobs (objective lens). Usually, a high magnification image (50,000x or greater) is obtained.
 2. Spot mode is selected to stop the scanning and the beam is positioned on the region of interest.
 3. Smallest condenser aperture (20 μm) is inserted into the beam path.
 4. Fluorescent screen is closed. A CBED pattern should be visible on the TEM screen, because the TEM is operated in the diffraction mode during STEM.
 5. Film Advance button is depressed and the diffraction pattern is recorded on film (usually 20-30 s).
-

6. While recording the diffraction pattern, the x-ray spectrum is also collected from the same area. Usually, a larger C_2 aperture (100 μm) is used to obtain a higher x-ray count rate.
 7. Screen is closed and an STEM image is obtained by switching to area mode.
- Steps 2 to 6 are repeated for analyzing other areas of the sample.

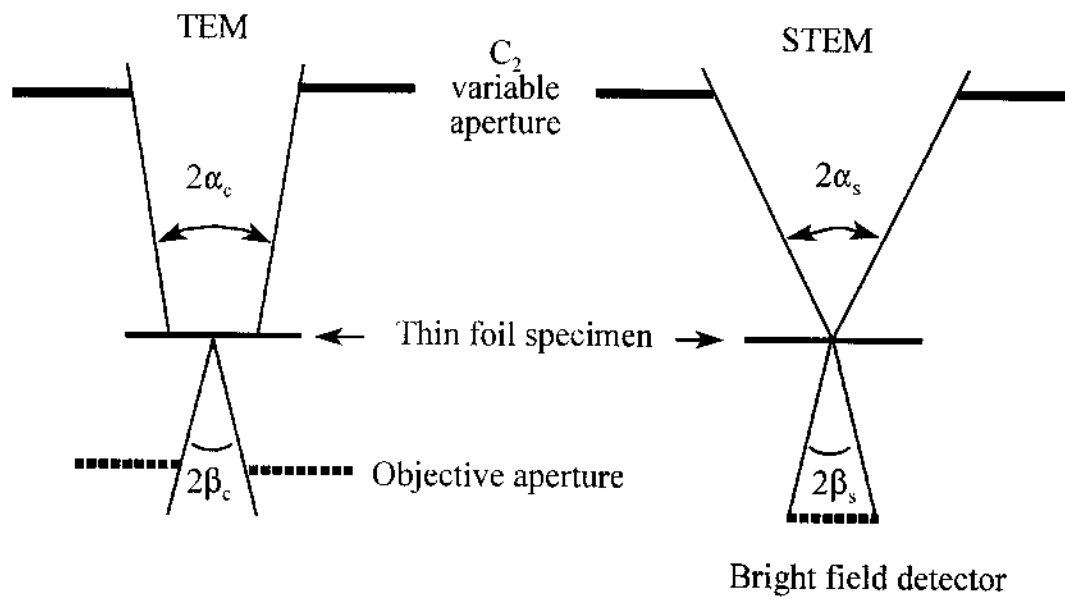


Figure A.1. Diagrams showing the relevant cone angles in TEM and STEM modes that must be adjusted for reciprocal imaging conditions.²

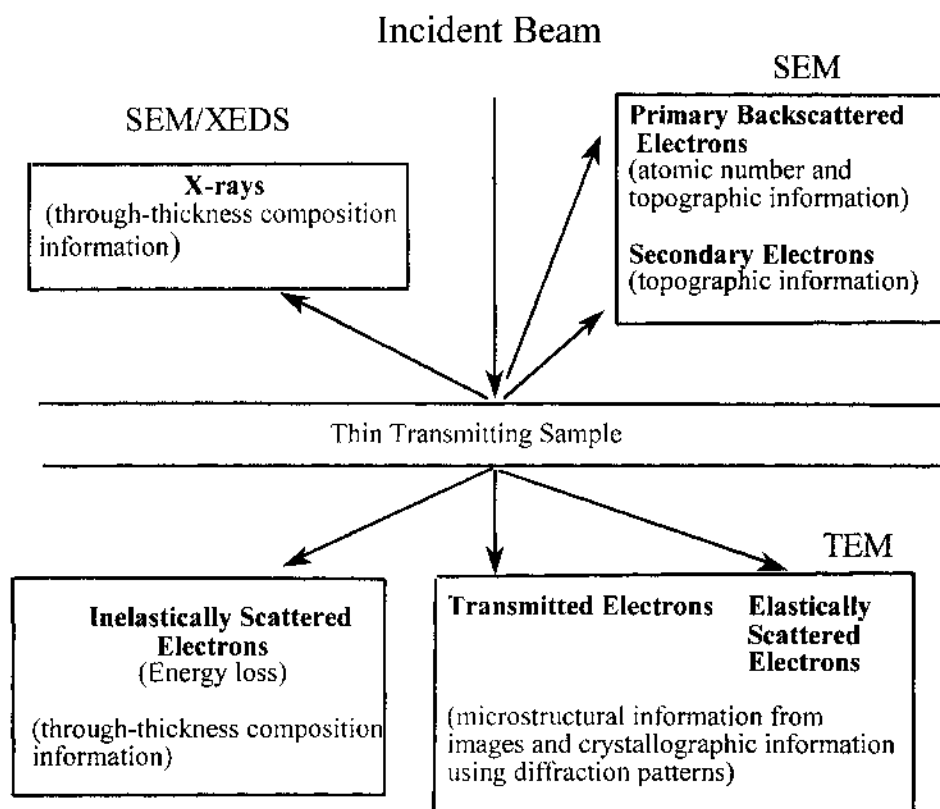


Figure A.2. Signals produced from the interaction of a high energy electron beam with a crystalline sample.⁵

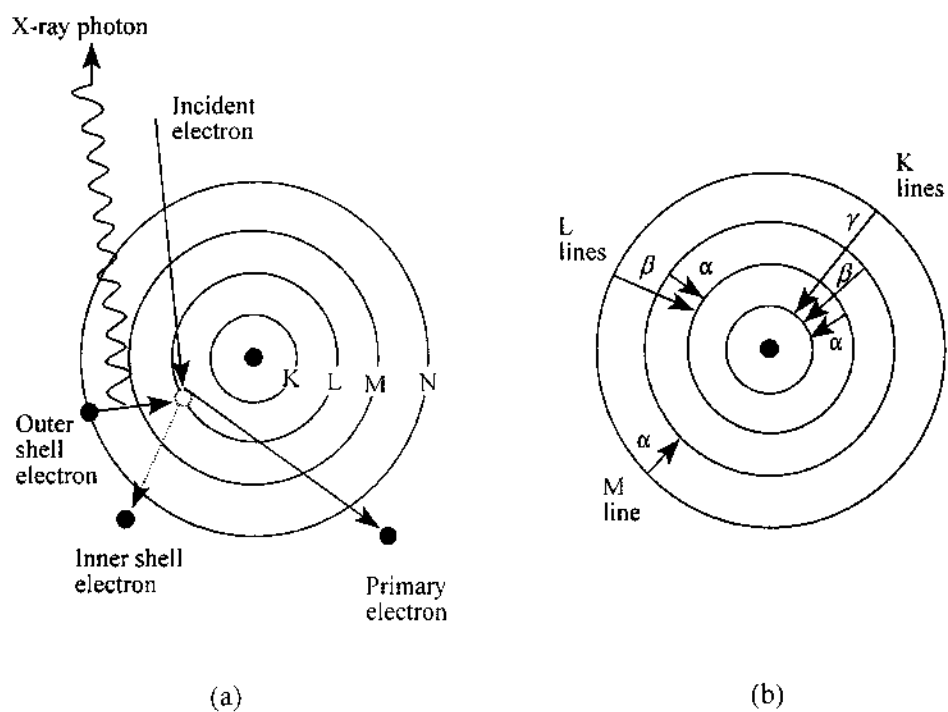


Figure A.3. (a) Characteristic x-ray generation (b) nomenclature of x-ray lines.

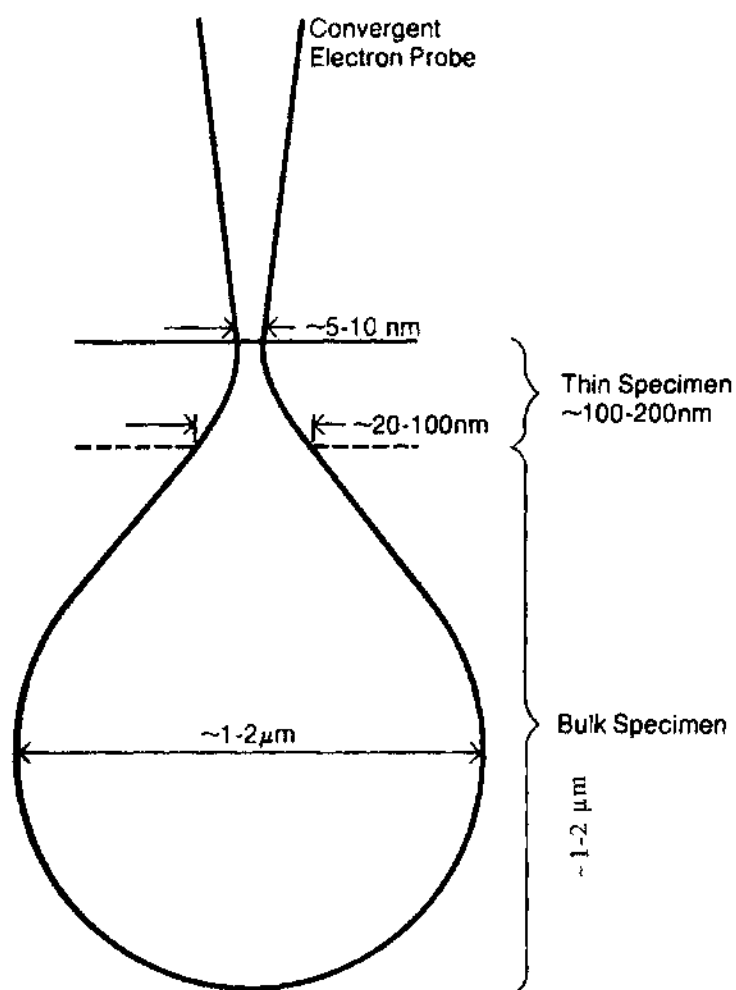


Figure A.4. The electron beam/sample interaction volume showing the approximate spatial resolution of x-ray analysis in thin and bulk samples.⁵

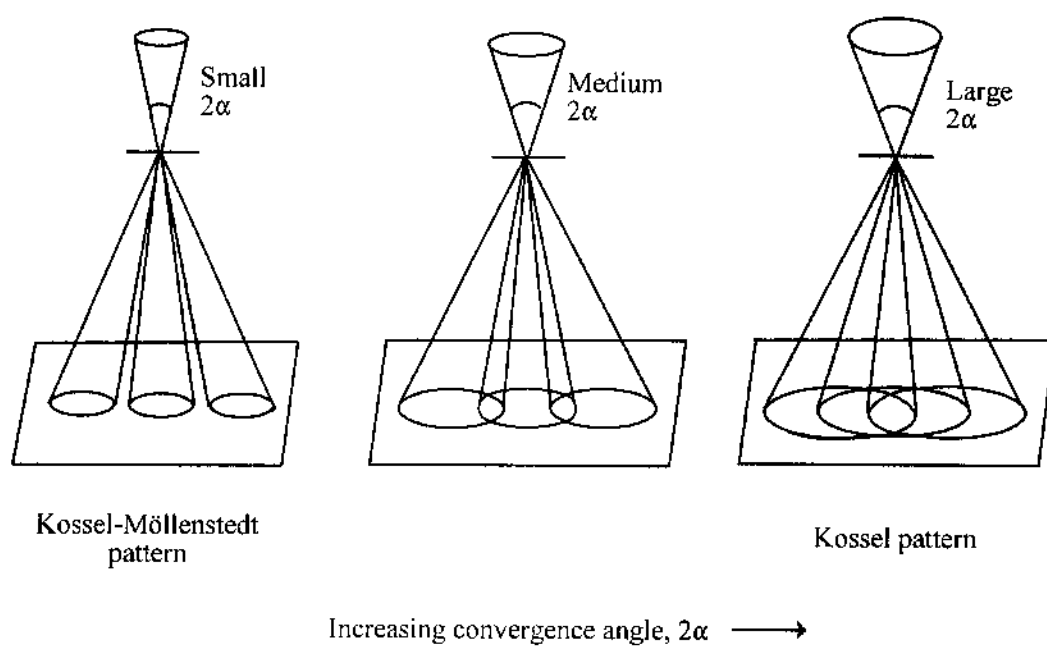


Figure A.5. The effect of varying the beam convergence angle 2α on the type of CDBP.

Increasing beam convergence is schematically shown from left to right.²

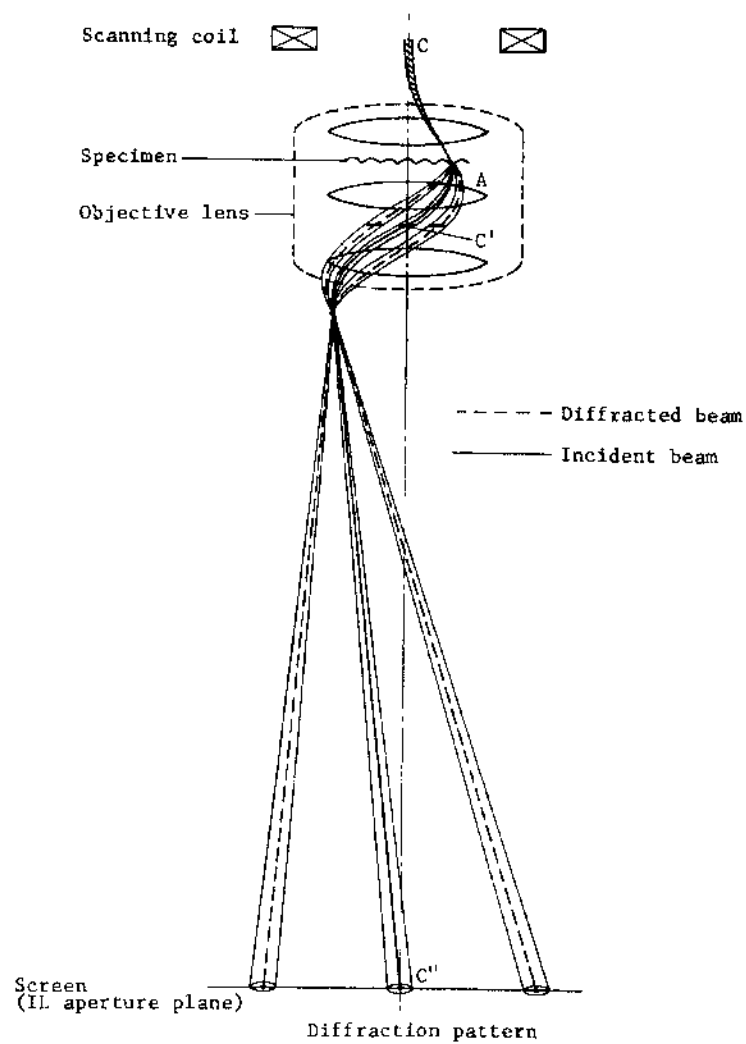


Figure A.6. Ray diagram of micro-area electron diffraction.⁷

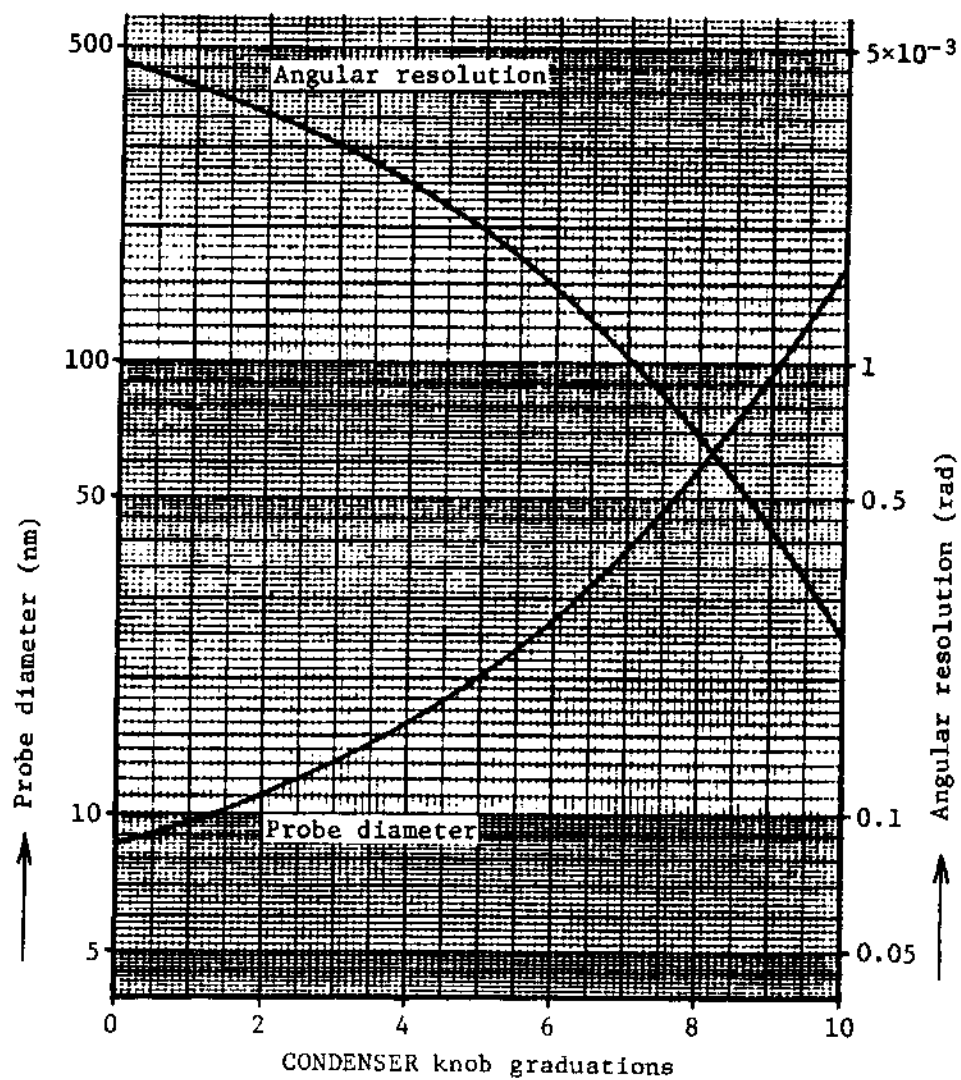


Figure A.7. Probe diameter and angular resolution.⁷

APPENDIX REFERENCES

1. D.C. Joy, A.D. Romig, Jr., and J.I. Goldstein, *Principles of Analytical Electron Microscopy*, (Plenum Press, 233 Spring Street, NY 10013, 1986).
2. D.B. Williams and C.B. Carter, *Transmission Electron Microscopy IV*, (Plenum Press, 233 Spring Street, NY 10013, 1996).
3. M.H. Loretto, *Electron Beam Analysis of Materials*, (Chapman and Hall Ltd., 733 Third Avenue, New York, NY 10017, 1984).
4. L.C. Feldman and J.W. Mayer, *Fundamentals of Surface and Thin Film Analysis*, (P.T.R. Prentice Hall, Englewood Cliffs, NJ 07632, 1986).
5. D.B. Williams, *Practical Analytical Electron Microscopy in Materials Science*, (Philips Electronic Instruments Inc., 85 McKee Drive, Mahwah, NJ 07430, 1987).
6. J.W. Edington, *Practical Electron Microscopy in Materials Science*, (Van Nostrand Reinhold Co., 450 West 33rd street, NY 10001, 1976).
7. Instruction Manual for EM-ASID3D Ultrahigh Resolution Scanning System, JEOL Ltd., Tokyo, Japan.

BIBLIOGRAPHY

Addendum to American National Standards Institute/American Dental Association Specification No. 1 for Alloy Dental Amalgam, JADA **95**, 614 (1977).

Allied High Tech Products, Inc., 2376 East Pacifica Place, Rancho Dominguez, CA 90220.

ASM Handbook, edited by Hugh Baker, Vol. 3 (ASM International, Materials Park, Ohio 44073, 1992).

A. Gangulee, G.C. Das, and M.B. Bever, Metallurgical Transactions **4**, 2063 (1973).

C.L. Reynolds, Jr. and F. E. Wawner, Jr., Biomat., Med. Dev., Art. Org. **2**, 67 (1974).

C.L. Reynolds, Jr., F.E. Wawner, and H.G.F. Wilsdorf, Scrip. Metall. **8**, 657 (1974).

C.L. Reynolds, Jr., F.E. Wawner, and H.G.F. Wilsdorf, J. Appl. Phys. **5**, 171 (1975).

C. W. Fairhurst, Ph.D. Dissertation, Northwestern University, Evanston IL (1966).

C.W. Fairhurst and G. Ryge, in *Advances in X-ray Analysis*, Plenum Press Vol. 5, 64 (1961).

D. B. Mahler and J. D. Adey, J. Dent. Res. **63**, 921 (1984).

D. B. Mahler, J.D. Adey and J.V. Eysden, J. Dent. Res. **54**, 218 (1975).

D.B. Mahler and J.D. Adey, J. Dent. Res. **70**, 1384 (1991).

D.B. Williams, *Practical Analytical Electron Microscopy in Materials Science*, (Philips Electronic Instruments Inc., 85 McKee Drive, Mahwah, NJ 07430, 1987).

D.B. Williams and C.B. Carter, *Transmission Electron Microscopy IV*, (Plenum Press, 233 Spring Street, NY 10013, 1996).

D.C. Joy, A.D. Romig, Jr., and J.I. Goldstein, *Principles of Analytical Electron Microscopy*, (Plenum Press, 233 Spring Street, NY 10013, 1986).

E.H. Greener, J.K. Yang, A.A. Grant, and M. Meshii, Aust. Dent. J. Oct., 363 (1968).

F. Aldinger and W. Kraft, *Z. Metallkde.* **68**, 523 (1977).

G. Petzow and G. Effenberg, *Ternary Alloys-A Comprehensive Compendium of Evaluated Constitutional Data on Phase Diagrams*, (VCH Verlagsgesellschaft, Weinheim, Germany), pp. 38-40, 256-261, (1988).

H. Yang, Ph.D. Dissertation, University of North Texas, Denton, TX (1993).

Instruction Manual for EM-ASID3D Ultrahigh Resolution Scanning System, JEOL Ltd., Tokyo, Japan.

International Center for Diffraction Data (12 Campus Blvd., Newtown Square, PA 19073), Powder Diffraction File PDF#11-67, 4-0800, 27-618, 29-1151, 1-1240, 2-0713.

J. F. DeFreitas, *Australian Dent. J.* **24**, 17 (1979).

J. H. Watkins, H. Nakajima, K. Hanaoka, L. Zhao, T. Iwamoto, and T. Okabe, *Dent. Mater.* **11**, 24 (1995).

J. P. Benedict, R. M. Anderson, and S. J. Klepeis, *Mater. Res. Soc. Proc.* **254**, 121 (1991).

J. R. Abbott, D. R. Miller, and D. J. Netherway, *J. Biomed. Mat. Res.* **20**, 1391 (1986).

J. W. Edington, *Practical Electron Microscopy in Materials Science* (Van Nostrand Reinhold Co., 450 West 33rd Street, New York 10001), Appendix 4, pp. 303-312 (1976).

K. Asgar, in *IADR Prog. and Abst.* 53, No. 23 (1974).

Kerr Manufacturing Co., Romulus, MI 48174.

L.B. Jonson, Jr., *J. Biomed. Mater. Res.* **1**, 415 (1967).

L.B. Jonson, Jr., *J. Biomed. Mater. Res.* **1**, 285 (1967).

L.B. Johnson and G.C. Paffenbarger, *J. Dent. Res.* **59**, 1412 (1980).

L.C. Feldman and J.W. Mayer, *Fundamentals of Surface and Thin Film Analysis*, (P.T.R. Prentice Hall, Englewood Cliffs, NJ 07632, 1986).

M. Gayler, *J. Inst. Metals* **60**, 376 (1937).

- M. Hansen and K. Anderko, *Constitution of Binary Alloys*, (McGraw-Hill, New York 1958).
- M.H. Loretto, *Electron Beam Analysis of Materials*, (Chapman and Hall Ltd., 733 Third Avenue, New York, NY 10017, 1984).
- N.K. Sarkar, J. Mater. Res: Mater. in Medicine **5**, 171 (1994).
- Noran Instruments, 2551 W. Beltline Highway, Middleton, WI. 53562-2679.
- P. Andersen and S.J. Jensen, Scand J. Dent. Res. **79**, 466 (1971).
- P. G. Boswell, Scripta Metallurgica **13**, 383 (1979).
- P.G. Boswell, J. Mater. Sci. **15**, 1311 (1980).
- P.G. Shewmon, *Transformation in Metals* (McGraw Hill, Inc. New York), 156 (1969).
- Quick Bonding Nail Glue, Sally Hansen Div., Del Laboratories, Inc. Farmingdale, NY 11735.
- R.D. Field, A.R. Cox, and H.L. Fraser, in *Rapid Solidification Technology Source Book* (American Society for Metals, Metals Park, Ohio 44073), 420 (1983).
- R. Mitchell, T. Okabe, and C.W. Fairhurst, J. Dent. Res (Special. Issue. B) **56**, 146 (1977).
- R. Mitchell, T. Okabe, and C.W. Fairhurst, J. Dent. Res. (Special. Issue. A) **57**, 125 (1978).
- R.J. Mitchell, T. Okabe, and M.B. Butts, J. Dent. Res. **60**, 480 (1981).
- R.J. Mitchell and T. Okabe, Critical Rev. in Oral Biology and Medicine **7**, 12 (1996).
- R.M. Waterstrat and T Okabe, *Intermetallic Compounds* (John Wiley & Sons Ltd.), Vol. 2, pp. 575-580 (1994).
- R.M. Waterstrat, J. O. M **42**, 8 (1990).
- R. W. Bryant, Aust. Dent. J. **29**, 163 (1984).
- R.W. Phillips, *Skinner's Science of Dental Materials*, Eighth Edition (Saunders Co., West Washington Square, PA 19105), pp. 302-310 (1982).
-

- S. S. White Dental Products International, Holmdel, NJ 07733.
- S. J. Klepeis, R. M. Anderson, and J. P. Benedict, Mater. Res. Soc. Proc. **115**, 179 (1988).
- S. J. Jensen and P. Anderson, Scan. J. Dent. Res. **80**, 158 (1972).
- S. J. Jensen, K. B. Olsen, and L. Utoft, Scand. J. Dent. Res. **81**, 572 (1979).
- S.J. Jensen, Scand. J. Dent Res. **93**, 84 (1984).
- S.J. Jensen, Scand. J. Dent. Res. **85**, 297 (1977).
- South Bay Technology, Inc., 1120 Via Callejon, San Clemente, California 92672.
- T. Hanawa, H. Takahasi, M. Ota, R. F. Pinizzotto, J. L. Ferracane, and T. Okabe, J. Dent. Res. **66**, 1470 (1987).
- T.K. Hooghan, R.F. Pinizzotto, J.H. Watkins, and T. Okabe, J. Mater. Res. **11**, 2474 (1996).
- T. Okabe, Manuscript prepared for the proceedings of the Satellite Symposium, "*Setting Mechanism of Dental Materials*", in Glasgow, Scotland, U.K.; co-sponsored by GC Corporation, The Dental Materials Group, IADR and The Academy of Dental Materials (1992).
- T. Okabe, A.L. Hines, R.F. Hochman, and L.O. Sims, Biomed. Mater. Res. **9**, 389 (1975).
- T. Okabe, F. Ling, and R.F. Hochman, J. Dent. Res. **54**, L162 (1975).
- T. Okabe, in *Encyclopedia of Materials Science and Engineering*, edited by R.W. Cahn (Pergamon Press, Oxford), Suppl. Vol. 2, 866 (1990).
- T. Okabe and R.J. Mitchell, Critical Rev. in Oral Biology and Medicine **7**, 23 (1996).
- T. Okabe, R. J. Mitchell, M.B Butts, and C.W. Fairhurst, J. Dent. Res. **57**, 975 (1978).
- T. Okabe, R.J. Mitchell, M.B. Butts, S.S. Galloway, and W.S. Twiggs, J. Biomedical Mat. Res. **19**, 727 (1985).
- T. Okabe, R.J. Mitchell, M.B. Butts, and C.W. Fairhurst, in *Metallurgie Dentaire* (PYC editions), 395 (1981).
-

T. Okabe, R. Mitchell, M. B. Butts, J. R. Bosley, and C. W. Fairhurst, *J. Dent. Res.* **56**, 1037 (1977).

T. Okabe, R. F. Hochman, and L. O. Sims, *J. Biomed. Mater. Res.* **9**, 221 (1975).

T. Okabe, R. J. Mitchell, M. B. Butts, and C. W. Fairhurst, *Microstructural Science* **7**, 165 (1979).

Y.C. Durandet, R.J. Finch and D.R. Miller, *Materials Forum* **17**, 51 (1993).
